

Hazy blue worlds: A holistic aerosol model for Uranus and Neptune, including Dark Spots

P.G.J. Irwin¹, N.A. Teanby², L.N. Fletcher³, D. Toledo⁴, G.S. Orton⁵, M.H. Wong⁶, M.T. Roman³, S. Pérez-Hoyos⁷, A. James¹, J. Dobinson¹

¹Department of Physics, University of Oxford, Parks Rd, Oxford, OX1 3PU, UK

²School of Earth Sciences, University of Bristol, Wills Memorial Building, Queens Road, Bristol, BS8 1RJ, UK

³School of Physics & Astronomy, University of Leicester, University Road, Leicester, LE1 7RH, UK

⁴Instituto Nacional de Técnica Aeroespacial (INTA), 28850, Torrejón de Ardoz (Madrid), Spain.

⁵Jet Propulsion Laboratory, California Institute of Technology, 4800 Oak Grove Drive, Pasadena,

CA 91109, USA

⁶Center for Integrative Planetary Science, University of California, Berkeley, CA 94720, USA

⁷University of the Basque Country UPV/EHU, 48013 Bilbao, Spain

Key Points:

- Ice Giant reflectivity spectra from 0.3 to 2.5 μm well approximated by a single aerosol model comprised of three to four distinct layers.
- Static stability region at 1–2 bar, caused by methane condensation, seems to lead to build-up of haze and seeds CH_4 snow at its base.
- Darkening of deepest $\text{H}_2\text{S}/\text{haze}$ layer, based at $p > 5\text{--}7$ bar, found to account well for spectral properties of dark spots.

Corresponding author: Patrick Irwin, patrick.irwin@physics.ox.ac.uk

This article has been accepted for publication and undergone full peer review but has not been through the copyediting, typesetting, pagination and proofreading process, which may lead to differences between this version and the Version of Record. Please cite this article as doi: [10.1029/2022JE007189](https://doi.org/10.1029/2022JE007189).

This article is protected by copyright. All rights reserved.

21 Abstract

22 We present a reanalysis (using the Minnaert limb-darkening approximation) of visible/near-
 23 infrared ($0.3 - 2.5 \mu\text{m}$) observations of Uranus and Neptune made by several instruments.
 24 We find a common model of the vertical aerosol distribution that is consistent with the
 25 observed reflectivity spectra of **both** planets, consisting of: 1) a deep aerosol layer with
 26 a base pressure $>5-7$ bar, assumed to be composed of a mixture of H_2S ice and photo-
 27 chemical haze; 2) a layer of photochemical haze/ice, coincident with a layer of high static
 28 stability at the methane condensation level at 1–2 bar; and 3) an extended layer of photo-
 29 chemical haze, likely mostly of the same composition as the 1–2-bar layer, extending
 30 from this level up through to the stratosphere, where the photochemical haze particles
 31 are thought to be produced. For Neptune, we find that we also need to add a thin layer
 32 of micron-sized methane ice particles at ~ 0.2 bar to explain the enhanced reflection at
 33 longer methane-absorbing wavelengths. We suggest that methane condensing onto the
 34 haze particles at the base of the 1–2-bar aerosol layer forms ice/haze particles that grow
 35 very quickly to large size and immediately ‘snow out’ (as predicted by Carlson et al., 1988),
 36 re-evaporating at deeper levels to release their core haze particles to act as condensa-
 37 tion nuclei for H_2S ice formation. In addition, we find that the spectral characteristics
 38 of ‘dark spots’, such as the Voyager-2/ISS Great Dark Spot and the HST/WFC3 NDS-
 39 2018, are well modelled by a darkening or possibly clearing of the deep aerosol layer only.

40 Plain Language Summary

41 Previous studies of the reflectance spectra of Uranus and Neptune have concentrated
 42 on individual, narrow wavelength regions and the conclusions have been difficult to com-
 43 pare with each other. Here, we analyse a combined set of observations from three dif-
 44 ferent instruments covering the wavelength range $0.3 - 2.5 \mu\text{m}$ to arrive at a **single** aerosol
 45 model that matches the observations at all wavelengths simultaneously for **both** plan-
 46 etes. We conclude that photochemical haze produced in the upper atmospheres of both
 47 planets is steadily mixed down to lower layers, where it forms part of a vertically-thin
 48 layer in a statically stable region above the methane condensation level at 1–2 bar. We
 49 suggest that methane condenses so rapidly upon these haze particles that it efficiently
 50 ‘snows’ out at the base of this layer, falling to lower, warmer levels, where the methane
 51 evaporates, releasing the core haze particles to ‘seed’ H_2S condensation. For Neptune
 52 we need to add an additional layer of moderately large methane ice particles at ~ 0.2 bar.
 53 Intriguingly, we find that a darkening (or perhaps clearing) of the lowest $\text{H}_2\text{S}/\text{haze}$ layer
 54 matches very well the observed properties of the dark spots seen occasionally in Nep-
 55 tune’s atmosphere and very occasionally in Uranus’s atmosphere.

56 1 Introduction

57 The visible and near-infrared spectra of the Solar System’s ‘Ice Giants’, Uranus and
 58 Neptune, have fascinated planetary astronomers for many years. The atmospheres of the
 59 Ice Giants are observed to have similar atmospheres with similar tropospheric temper-
 60 ature profiles and He/H_2 ratios, determined from Voyager-2 observations and post anal-
 61 yses (Lindal et al., 1987; Lindal, 1992; Sromovsky et al., 2011), and similar, high mole
 62 fractions of methane of $\sim 4\%$ (Karkoschka & Tomasko, 2009, 2011; Sromovsky et al., 2014,
 63 2019; Irwin, Toledo, Braude, et al., 2019). Both planets appear blue or bluish-green to
 64 the naked eye, in contrast to the more yellowish appearance of Jupiter and Saturn. We
 65 now know this blueness comes from a combination of this higher abundance of gaseous
 66 methane, which has strong absorption bands in the infrared and red portion of the vis-
 67 ible spectrum, and enhanced Rayleigh-scattering from atmospheres that have low abun-
 68 dances of aerosols. In addition to CH_4 , Irwin et al. (2018) detected the presence of gaseous
 69 H_2S in Uranus’s atmosphere, which is also probably present in Neptune’s atmosphere
 70 (Irwin, Toledo, Garland, et al., 2019). Hence, it would seem that H_2S and NH_3 react to-

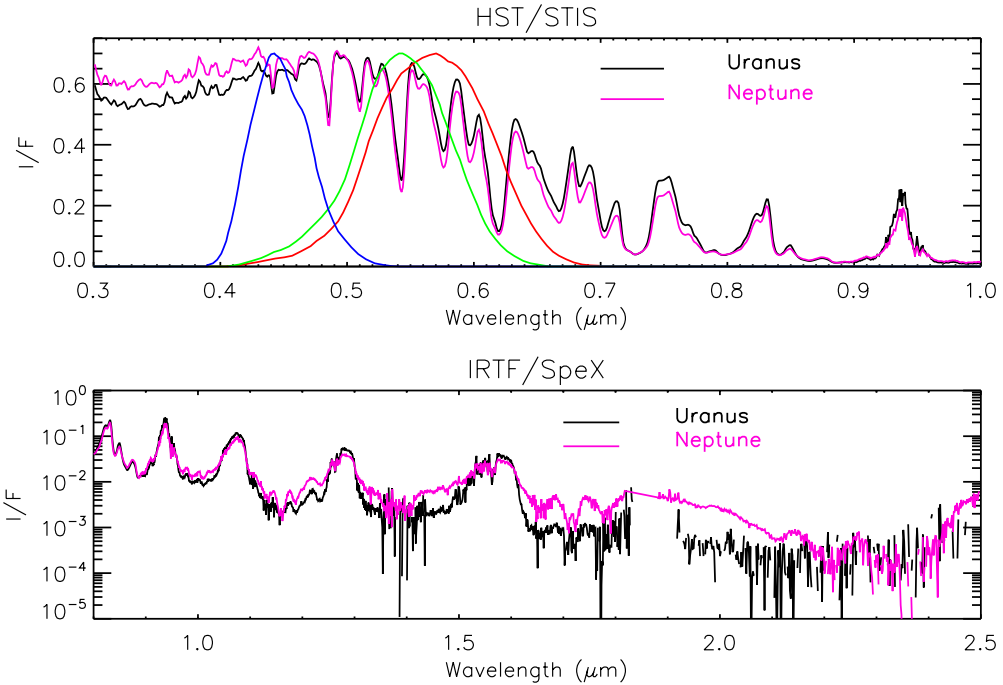


Figure 1. Composite HST/STIS and IRTF/SpeX central-meridian-averaged I/F spectra of Uranus and Neptune compared with each other over the HST/STIS ($0.3\text{--}1.0\ \mu\text{m}$) and IRTF/SpeX ($0.8\text{--}2.5\ \mu\text{m}$) spectral ranges. Note that the HST/STIS data have been smoothed to the IRTF/SpeX resolution of $0.002\ \mu\text{m}$. Also overplotted, for reference, in the top panel are the red, green, blue sensitivities of the human eye (Stockman & Sharpe, 2000; Stockman, 2019).

gether to form a deep cloud of $\text{NH}_4\text{SH(s)}$ (at pressures of ~ 40 bar), which leaves H_2S alone to condense at a lower pressure, but greater than ~ 3 bar (Irwin et al., 2018; Irwin, Toledo, Braude, et al., 2019). Given the known temperature profile and methane abundance, methane should condense at ~ 1.5 bar in both planets, and hence it might be expected that a thick cloud of methane should similarly shroud both worlds. However, this does not seem to be the case, although upper tropospheric (200-600 mb) bright clouds are commonly seen in Neptune's atmosphere, and occasionally in Uranus's atmosphere. In addition, several dark spots have been seen in Neptune's atmosphere, most famously the Great Dark Spot observed by Voyager-2 in 1989 (Smith et al., 1989), but also in more recent Hubble Space Telescope observations (Hammel et al., 1995; Sromovsky et al., 2011; Wong et al., 2018; Hsu et al., 2019). These spots are of unknown origin, but seem only to be visible at wavelengths < 700 nm. One dark spot has been reported in Uranus's atmosphere (Hammel et al., 2009), which was less dark, but appears to have been observable to wavelengths as long as $1.5\ \mu\text{m}$.

At first glance, the visible/near-infrared spectra of these planets are very similar, as can be seen in Fig. 1. However, it appears that at the peaks, Neptune is generally slightly less bright, while at longer methane-absorbing wavelengths, and in the UV, Neptune is more reflective. To simulate these spectra, a number of models of the vertical distribution of clouds and hazes have been proposed for Uranus (e.g., Karkoschka & Tomasko, 2009; Tice et al., 2013; Irwin et al., 2015, 2018; Roman et al., 2018; Sromovsky et al., 2019) and for Neptune (e.g., Karkoschka & Tomasko, 2011; Irwin et al., 2011a; Luszcz-Cook et al., 2016; Irwin, Toledo, Garland, et al., 2019; Irwin, Toledo, Braude, et al., 2019). All these models mostly have a thick aerosol layer at 2–4 bars (assumed to be photochem-

ical haze and perhaps mixed with H₂S ice) and some sort of overlying haze. This aerosol layer has been modelled as a uniformly mixed (with height) haze (e.g., Tice et al., 2013; Irwin et al., 2015), or as a discrete detached haze (e.g., Irwin, Toledo, Braude, et al., 2019), or has been modelled *ab initio* from microphysical models (e.g., Toledo et al., 2019, 2020). The reason that all these constituents are thought to be photochemically-produced hazes, rather than clouds, is that away from the discrete, bright upper tropospheric methane ice clouds, they are optically thin, appear to be spatially homogeneous and also need at some wavelengths to have single-scattering albedos considerably less than unity (e.g., Irwin et al., 2011a, 2015) in order to be consistent with the observed limb-darkening/limb-brightening. The particles in the upper-tropospheric/lower-stratospheric haze, in particular, are seen to be rather dark in the 1–2 μm region (e.g., Irwin et al., 2011a), and the particles in the ‘main’ 2–4-bar layer also seem to have significant absorption features. By contrast, freshly condensed methane (and presumably also H₂S ice) is expected to be nearly conservatively scattering.

Historically, cloud/haze retrieval studies have taken a set of observed spectra, covering a particular range of wavelengths, and found a cloud/haze model consistent with these observations using simple cloud/haze parameterisations and *ad hoc* adjustments of single-scattering albedo and scattering phase function asymmetry. Different studies have used different wavelength ranges and different *ad hoc* cloud/haze models, which has made it difficult to interpret these studies simultaneously to gain a deeper, simpler representation of the aerosol structures of these worlds. What makes such a holistic approach even more difficult is that we have no ‘ground truth’ information on what the ice giant aerosols are made of and what their spectral properties are. Hence, the problem is extremely degenerate and multiple solutions exist. Recently, attempts have been made to fit a wide range of wavelengths simultaneously using moderately self-consistent models. Irwin et al. (2015) modelled IRTF/SpeX observations (0.8–1.8 μm) of Uranus, recorded near the disc centre, using a simple two-component model comprising a vertically thin aerosol layer based at ~ 2 bar, with variable opacity, base pressure and fractional scale height, combined with an extended haze of variable opacity, but fixed base pressure of 1.0 bar and fixed fractional scale height of 1.0 (i.e., uniformly mixed). This cloud/haze scheme was linked with a self-consistent cloud-scattering model that fitted for the imaginary refractive index spectra of the two constituents, reconstructing the real part using a Kramers-Kronig analysis and then calculated the extinction cross-sections, single-scattering albedos and phase functions using Mie theory. It was found that the particles in the ‘main’ ~ 2 -bar aerosol layer must be significantly more absorbing at wavelengths longer than 1 μm . Another study to find a model able to account for the observed reflectivity spectrum over a wide wavelength range is that of Sromovsky et al. (2019), who reanalysed HST/STIS observations (0.3–1.0 μm) of Uranus (Karkoschka & Tomasko, 2009). Like Irwin et al. (2015), Sromovsky et al. (2019) favoured a simple two-component cloud/haze structure to the more complex five-layer structure used in their previous analysis (Sromovsky et al., 2014), and like Irwin et al. (2015) were able to make their cloud/haze model consistent out to 1.6 μm with IRTF/SpeX and Keck/NIRC2 observations by increasing the particles’ imaginary refractive index at longer wavelengths. This increase of inferred n_{imag} with wavelength has also been reported by de Kleer et al. (2015). Sromovsky et al. (2019) noted that a plausible condensable species in the 1–3 bar region is H₂S, but since the spectral characteristics of this condensate are not currently known, the determined wavelength dependence of n_{imag} could not be used to constrain its identity. Finally, Sromovsky et al. (2019) reported the possible detection of a second, deeper aerosol layer near ~ 10 bar, which they tentatively suggested to be composed of NH₄SH.

While attempts have been made to model Uranus spectra over a wider wavelength range, the same cannot be said for Neptune. Neptune is a significantly smaller target than Uranus and hence more difficult to spatially resolve, especially at longer wavelengths. It is also significantly more cloudy (i.e., upper tropospheric methane ice clouds are widespread, for example Irwin et al., 2016), which at lower spatial resolution makes it difficult to dis-

148 entangle sunlight reflected from the background aerosol structure from that reflected from
 149 the discrete bright clouds. However, given these observational difficulties it is surpris-
 150 ing that to our knowledge no attempt has previously been made to fit the spectra of both
 151 these planets with a single model, even though the observable atmospheres of these plan-
 152 etes have similar tropospheric temperature and composition and have similar observable
 153 spectra, although we do note that the Uranus and Neptune models of Karkoschka and
 154 Tomasko (2009) and Karkoschka and Tomasko (2011) are very similar. In this paper we
 155 present a holistic aerosol model of both Uranus and Neptune and also propose a simple
 156 way of explaining the phenomenon of ‘dark spots’, which are occasionally seen in these
 157 atmospheres, but whose nature has until now been a mystery.

158 2 Observations

159 The observations analysed in this study come from a variety of sources. The imag-
 160 ing observations from HST/WFC3 and Voyager-2/ISS (for Neptune) are described later,
 161 but here we give an overview of the spectral observations considered.

162 2.1 Uranus spectral observations

163 We analysed HST/STIS observations of Uranus from 2002 (Karkoschka & Tomasko,
 164 2009), 2012 (Sromovsky et al., 2014) and 2015 (Sromovsky et al., 2019). Since our pri-
 165 mary intention in this paper was not to revisit the question of latitudinal variability of
 166 methane abundance or polar brightening, we concentrated on the 2002 data (Karkoschka
 167 & Tomasko, 2009), when the disc of Uranus appeared particularly featureless, allowing
 168 us to combine the data from all latitudes together. This observation was made on Au-
 169 gust 19th 2002, between 01:43 and 10:57 UT. HST/STIS is actually a long slit spectrom-
 170 eter, but the slit was aligned parallel to the central meridian and then stepped from the
 171 central meridian to the edge of the planet to form a ‘cube’ of half the planet, where at
 172 each location on the disc a complete spectrum covering 300.4 – 1020.0 nm was recorded
 173 at a resolution of 1 nm, sampled every 0.4 nm.

174 We also analysed an observation of Uranus made using IRTF/SpeX, another long-
 175 slit spectrometer. In this case, the slit was aligned on the disc centre and the fluxes in-
 176 tegrated along the central meridian. This standard reference spectrum is available on
 177 the IRTF Spectral Library website (http://irtfweb.ifa.hawaii.edu/~spex/IRTF_Spectral_Library), reported by Rayner et al. (2009), and was made in SXD mode (0.8 – 2.5 μm)
 178 on May 18th 2000. These data have a spectral resolution of 0.002 μm .

180 Finally, we analysed observations of Uranus made with Gemini/NIFS in H-band
 181 (i.e., 1.47 – 1.8 μm) in 2009 and 2010 (Irwin et al., 2011b; Irwin, Teanby, et al., 2012).
 182 Gemini/NIFS is an integral field-unit (IFU) spectrometer that simultaneously records
 183 spatial and spectral information, and where each pixel or ‘spaxel’ is composed of a com-
 184 plete spectrum covering the targeted spectral range with a spectral resolving power of
 185 $R \sim 5200$. The actual cube used for our retrieval study was recorded on 2nd Septem-
 186 ber 2009, which had good spatial resolution and was reasonably clear of discrete features.

187 To enable easy intercomparison and simulation speed the HST/STIS and Gemini/NIFS
 188 data were smoothed to the spectral resolution of IRTF/SpeX of 0.002 μm (i.e., 2 nm),
 189 and sampled with a step of 0.001 μm .

190 During the time period spanned by these observations, Uranus moved through its
 191 orbit about the Sun and Table 1 lists the date, sub-Earth latitude (planetocentric) ϕ_E ,
 192 and also the apparent target-centered longitude of the Sun L_s (which gives a convenient
 193 measure of season, with 0° being northern spring equinox, 90° being northern summer
 194 solstice, etc.) of the observations. In addition, we list the disc-integrated photometric
 195 magnitudes of Uranus as observed and reported by Lockwood (2019) in the y (551 nm)

Table 1. Summary of Spectral Observations of Uranus and Neptune

Uranus observations								
Date	Instrument	Wavelength range	L_s	Sub-earth latitude ϕ_E	b-mag 471 nm	y-mag 511 nm	b-y	
May 18th 2000	IRTF/SpeX	0.8 – 2.5 μm	330.4°	–27.6°	5.769	5.560	0.209	
August 19th 2002	HST/STIS	300 – 1020 nm	339.3°	–21.4°	5.779	5.577	0.202	
September 2nd 2009	Gemini/NIFS	1.47 – 1.8 μm	6.8°	+7.9°	5.785	5.592	0.193	
Neptune observations								
Date	Instrument	Wavelength range	L_s	Sub-earth latitude ϕ_E	b-mag 471 nm	y-mag 511 nm	b-y	
June 30th 2000	IRTF/SpeX	0.8 – 2.5 μm	259.5°	–28.7°	7.830	7.704	0.126	
August 3rd 2003	HST/STIS	300 – 1020 nm	266.2°	–29.1°	7.809	7.689	0.120	
September 7th 2009	Gemini/NIFS	1.47 – 1.8 μm	279.5°	–28.8°	7.819	7.694	0.125	

and b (472 nm) filters of the Strömgren photometric system, which gives a measure of the overall disc brightness and blueness. It can be seen that the IRTF/SpeX and HST/STIS observations were both made with $L_s \sim 335^\circ$ and $\phi_E \sim -25^\circ$. However, the Gemini/NIFS observation comes from just after the northern spring equinox in 2007 with $\phi_E = 7.9^\circ$. Hence, while the IRTF/SpeX and HST/STIS observations will be slightly more weighted to conditions in the southern hemisphere, the Gemini/NIFS observations will be more weighted to equatorial regions and in a slightly later season. However, neither set of observations will sample well the hazes in the polar regions. From 2000 to 2009 the disc-averaged magnitude of Uranus decreased by ~ 0.03 and became slightly more blue as the southern polar ‘hood’ or ‘cap’ (e.g., Sromovsky & Fry, 2008) became less visible. However, these changes are relatively small, enabling us to assume that all three sets of observations were observing approximately the same disc of Uranus. However, care should be taken when comparing this work with Voyager-2 studies of Uranus’s aerosol structure, since Uranus was then near southern summer solstice and had a well developed ‘hood’ and markedly higher albedo and thus brightness (Lockwood, 2019).

2.2 Neptune spectral observations

We analysed HST/STIS observations of Neptune (Karkoschka & Tomasko, 2011) made on August 3rd 2003, between 4:38 and 14:15 UT. As for the Uranus HST/STIS data these form a ‘cube’ of half of Neptune’s disc, covering 300.4 – 1020.0 nm.

We also analysed a reference observation of Neptune made using IRTF/SpeX and integrated along the central meridian, available on the IRTF Spectral Library (Rayner et al., 2009). The SXD component of this reference spectrum analysed here (0.8 – 2.5 μm), was observed on June 30th 2000.

Finally, we analysed observations of Neptune made with Gemini/NIFS in 2009 (H-band) and 2011 (I, J, and H-band, i.e., 0.94 – 1.16 μm , 1.14 – 1.36 μm , and 1.47 – 1.8 μm , respectively) (Irwin et al., 2011a, 2016). The actual cube used for our retrieval study was recorded in the H-band on 7th September 2009 and was chosen for its good spatial resolution and reasonably limited distribution of discrete cloud features.

During the time period spanned by these observations, Neptune also moved through its orbit about the Sun and Table 1 again lists the date, sub-Earth latitude ϕ_E , apparent target-centered longitude of the Sun L_s , and the disc-integrated photometric magnitudes (Lockwood, 2019) of the observations. Neptune’s southern summer solstice occurred in 2005, but Neptune’s slower orbit about the Sun means that L_s and ϕ_E differed little during the total elapsed period, and can be assumed to be $\sim 270^\circ$ and $\sim -29^\circ$,

respectively. However, it can be seen that all three data sets will be weighted towards conditions in the southern hemisphere, with the south polar region clearly visible. From 2000 to 2009 the disc-averaged magnitudes and colour of Neptune were found not to vary significantly (Lockwood, 2019), again enabling us to assume that all three sets of observations were observing approximately the same disc of Neptune. However, care should again be taken when comparing this work with Voyager-2 studies of Neptune's aerosol structure, and indeed the Voyager-2/ISS observations described later in this paper, since Neptune was then still approaching southern summer solstice and was noticeably darker (Lockwood, 2019).

Once again, to enable easy intercomparison the HST/STIS and Gemini/NIFS data were smoothed to IRTF/SpeX spectral resolution.

3 Analysis

3.1 Atmospheric and Radiative Transfer Modelling

We modelled these observations using the radiative transfer and retrieval tool, NEMESIS (Irwin et al., 2008; Irwin, Teanby, de Kok, et al., 2022a, 2022b). To account for multiple scattering, NEMESIS employs a plane-parallel matrix operator model (Plass et al., 1973), where integration over zenith angle is performed with a Gauss-Lobatto quadrature scheme, while the azimuth integration is done with Fourier decomposition. We have found that five zenith angles are usually sufficient to model the giant planet I/F spectra and the number of azimuth Fourier components is set from the viewing and solar zenith angles as $N_F = \lfloor \Theta/3 \rfloor$, where $\Theta = \max[\theta, \theta_0]$ and where θ is the observation zenith angle (in degrees) and θ_0 is the solar zenith angle (in degrees). This scaling of N_F with Θ is necessary to reconstruct reliably the scattering functions at higher zenith angles, but comes at a considerable computational cost. Calculations at intermediate zenith angles are interpolated between the matrix operator calculations at the nearest tabulated viewing and solar zenith angles. The five-angle zenith angle quadrature scheme used here is listed in Table 1 of Irwin et al. (2021).

NEMESIS was run in correlated- k mode, with the methane k -tables generated from a number of different sources as described in Section 3.3. For H_2 - H_2 and H_2 -He collision-induced absorption we used the coefficients of Borysow et al. (1989); Borysow and Frommhold (1989); Borysow et al. (2000), assuming a thermally-equilibrated ortho:para hydrogen ratio for both Uranus and Neptune. Rayleigh scattering was included as described in Irwin, Toledo, Braude, et al. (2019), and the effects of polarization and Raman scattering were included as described in Section 3.3. We used the solar spectrum of Chance and Kurucz (2010), extrapolated to longer/shorter wavelengths with the solar spectrum of Kurucz (1993). This combined solar spectrum was smoothed with a triangular line shape of FWHM = 0.002 μm for consistency with the Uranus and Neptune resampled spectra.

3.2 Atmospheric Models

The reference temperature and mole fraction profile for Uranus is the same as that used by Irwin et al. (2018) and is based on the 'F1' temperature profile determined from Voyager 2 and HST/STIS observations (Sromovsky et al., 2011), with $\text{He:H}_2=0.131$ and including 0.04% mole fraction of neon. We adopted a simple 'step' model for the methane profile with variable deep mole fraction (*a priori* 4%), variable relative humidity above the condensation level and a limiting stratospheric mole fraction of 1×10^{-4} (Encrenaz et al., 1998; Orton et al., 2014). For the atmospheric static stability study discussed later, we also added saturation-limited profiles of H_2S and NH_3 . When dealing with condensing gases such as CH_4 , once the profile for that gas was determined, the abundance of H_2 and He was scaled at each level, keeping $\text{He:H}_2=0.131$, to ensure that the mole fractions added up to 1.0

The reference temperature and mole fraction profile for Neptune is the same as that used by Irwin, Toledo, Braude, et al. (2019) and Irwin et al. (2021) and is based on the ‘N’ profile determined by Voyager-2 radio-occultation measurements (Lindal, 1992), with $\text{He:H}_2 = 0.177$ (15:85) and including 0.3% mole fraction of N_2 . We again adopted a simple ‘step’ methane model with a variable deep mole fraction, variable relative humidity above the condensation level and limiting the stratospheric mole fraction to 1.5×10^{-3} (Lellouch et al., 2010). Again, the abundances of H_2 and He were adjusted at each level to ensure the mole fractions added up to 1.0, keeping $\text{He:H}_2 = 0.177$.

3.3 Spectral Modelling

The HST/STIS and IRTF/SpeX observations of both Uranus and Neptune were first combined to give composite central-meridian-averaged spectra of both planets, which are shown in Fig. 1. To create these combined spectra, we took the HST/STIS observations of Uranus and Neptune from 2002 and 2003, respectively, averaged them along the central meridian (masking discrete cloud features in the Neptune STIS data) and then scaled the IRTF/SpeX Uranus and Neptune spectra to match at overlapping wavelengths from 0.85 to 1.0 μm . This scaling was necessary as the IRTF/SpeX data are in units of line-integrated total flux and needed to be converted to I/F. Given uncertainty in the slit size and position it was not possible to do this *ab initio* with sufficient accuracy and hence re-scaling was necessary to ensure consistency with HST/STIS data. The Gemini/NIFS data, although not used in this initial analysis, were also averaged along the central meridian and their reflectivities adjusted to match the scaled IRTF/SpeX spectrum at overlapping wavelengths for later use.

Until now, our radiative transfer model NEMESIS has not incorporated Raman scattering, but since the HST/STIS observations extend to 0.3 μm , where Sromovsky (2005a) shows that Raman scattering is significant, it was necessary here to incorporate this effect. To do this, we followed the approach of Sromovsky (2005a) and considered only the $S(0)$, $S(1)$ and combined ‘Q’ transitions, using the cross-section absorption coefficients of Ford and Browne (1973). Radiation scattered from short to longer wavelengths was introduced at the longer wavelengths as an additional pseudo-thermal-emission term, using the assumption of Sromovsky (2005a) that this Raman re-emitted radiation is effectively isotropic, with wavenumber shifts of 354.69 cm^{-1} , 587.07 cm^{-1} and 4160.00 cm^{-1} , respectively for the $S(0)$, $S(1)$ and combined ‘Q’ transitions. In addition to including Raman scattering, we also further revised NEMESIS to incorporate a correction for polarisation effects as described by Sromovsky (2005b).

Using our upgraded NEMESIS model we show in Fig. 2 synthetic spectra calculated from our assumed Uranus and Neptune atmospheres for aerosol-free conditions, including Rayleigh scattering, Raman scattering, $\text{H}_2\text{-H}_2$ and $\text{H}_2\text{-He}$ collision-induced absorption (CIA), and absorption by gaseous methane. As can be seen, the measured reflectivity (I/F) of both Uranus and Neptune decreases rapidly with wavelength and is well matched overall by a $1/\lambda^4$ curve, suggesting that any aerosols which are present are small and of low integrated opacity. In Fig. 2 we compare calculations made using three different available sources of methane absorption data. The band data of Karkoschka and Tomasko (2010), converted to k-tables by Irwin et al. (2011a), covers the entire wavelength range and reproduces most of the observed features well. However, at longer wavelengths we can also use k-tables generated from HITRAN2016 methane line data (Gordon et al., 2017), and a more recent compilation of methane line data from the TheoRETS project (Rey et al., 2018). The HITRAN2016 data can be seen to be in good agreement with the band/k-data at wavelengths longer than 1.0 μm , while the TheoRETS data extends reasonably well to even shorter wavelengths of 0.75 μm . However, neither set extends to visible wavelengths and since our aim in this study is to find a holistic aerosol model of Uranus and Neptune that matches all wavelengths covered by HST/STIS, IRTF/SpeX and Gemini/NIFS simultaneously we used the band/k-data of Karkoschka and Tomasko

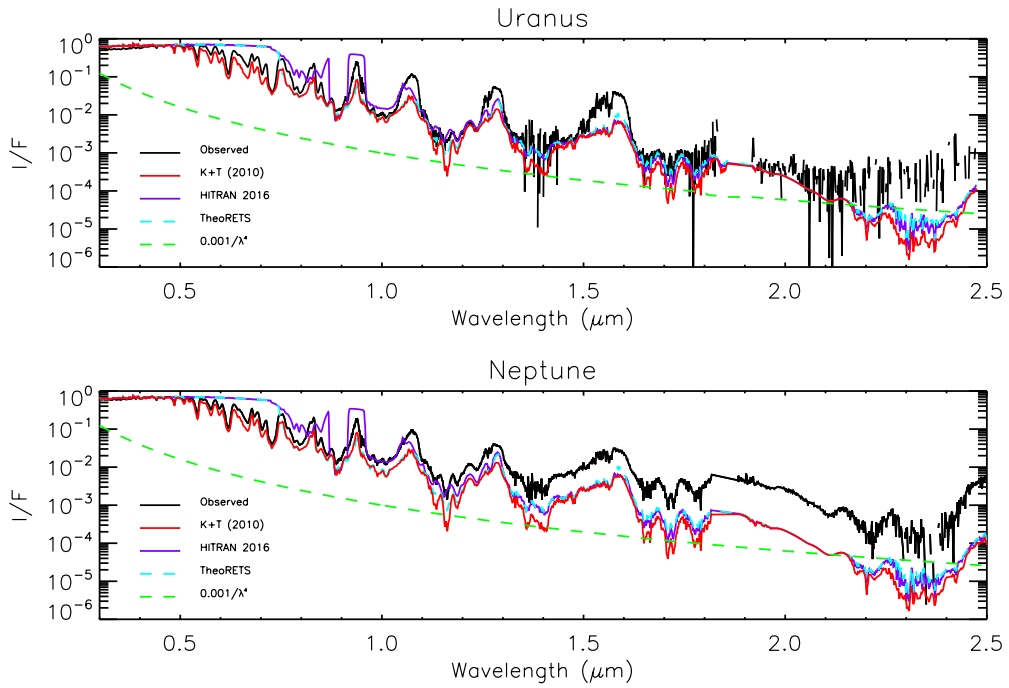


Figure 2. Combined HST/STIS and IRTF/SpeX central-meridian-averaged I/F spectra of Uranus and Neptune compared with calculations from an aerosol-free atmosphere including only Rayleigh/Raman scattering and gaseous absorption from methane and hydrogen-helium collision-induced absorption. The observations are plotted in black, while calculations using different sources of methane absorption from band data (Karkoschka & Tomasko, 2010) and line datasets HITRAN2016 (Gordon et al., 2017) and TheoRETS (Rey et al., 2018) are over-plotted in red, purple and cyan, respectively. Also plotted in green in both panels are simple $1/\lambda^4$ curves, showing the general trend of the combined spectra. N.B., the HITRAN2016 and TheoRETS do not cover the entire range and so at shorter wavelengths the calculations revert to Rayleigh/Raman scattering only.

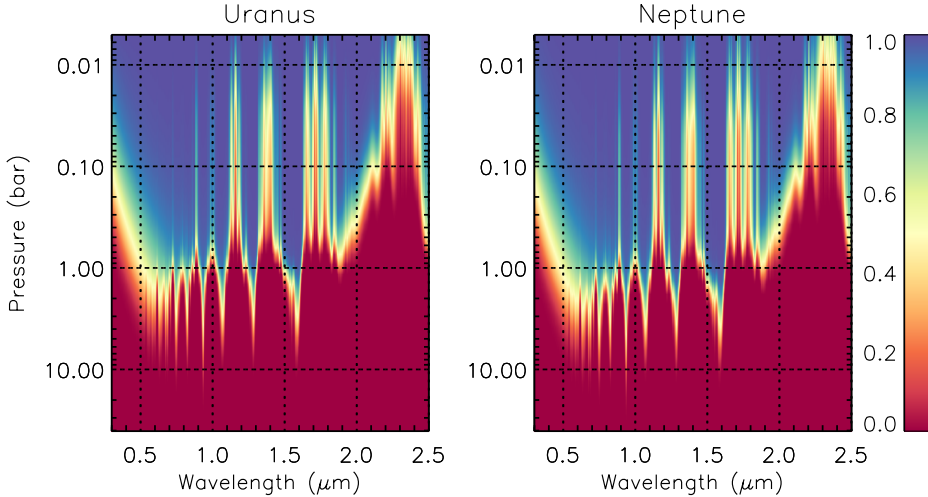


Figure 3. Two-way transmission from space, for a vertical path, to different levels in our standard Uranus and Neptune atmospheres for aerosol-free conditions. These calculations include Rayleigh scattering, Raman scattering and absorption from gaseous methane and hydrogen-helium collision-induced absorption.

(2010)/Irwin et al. (2011a) in this study. It is also apparent from Figs. 1–2 that Neptune is more reflective than Uranus at methane-absorbing wavelengths longer than $\sim 1 \mu\text{m}$, indicating that Neptune has a higher opacity of upper-atmosphere aerosols, which must be of a size greater than $\sim 1 \mu\text{m}$ in order to be visible at these longer wavelengths. Furthermore, it would appear that any aerosols in Uranus’s upper atmosphere must be of very low opacity, since a pure Rayleigh/Raman scattering calculation already matches the observed reflectivity at methane-absorbing wavelengths reasonably well.

In order to analyse the observations, we needed to determine the depths to which sunlight can penetrate at different wavelengths. In Fig. 3 we show contour plots of the two-way transmission from space, for a vertical path, to different levels in the atmospheres of Uranus and Neptune for aerosol-free conditions, including Rayleigh scattering, Raman scattering, methane absorption and hydrogen-helium collision-induced absorption. Here it can be seen that the penetration depth is very similar for Uranus and Neptune, but that a radiative transfer model wishing to simulate the observations needs potentially to cover a very wide range of pressure levels. Hence, the pressure range for both Uranus and Neptune models was set to cover $40 - 0.001$ bar and the atmosphere split into 39 layers (equally spaced in log pressure) for our radiative transfer calculations.

To best analyse the combined HST/STIS, IRTF/SpeX and Gemini/NIFS observations, and place strong constraint on the vertical structure and spectral dependence of particle scattering properties, we needed to develop an efficient way of modelling the observed centre-to-limb variations of the HST/STIS and Gemini/NIFS data and combine these with the wider wavelength-range central-meridian-averaged IRTF/SpeX observations, which provide important constraints on particle size and better probe lower pressure levels at the longer wavelengths. To do this we employed the Minnaert limb-darkening approximation (Minnaert, 1941), where for an observation at a particular wavelength, the reflectivity R is approximated as:

$$R = R_0 \mu_0^k \mu^{k-1}. \quad (1)$$

Here, μ and μ_0 are the cosines of the viewing and solar zenith angles, respectively, R_0 is the fitted nadir reflectance, and k is the fitted limb-darkening parameter. Irwin et al. (2021) applied this model to VLT/MUSE observations of Neptune made in 2018 and found it to give a very good approximation to the observations and was also well reproduced by the NEMESIS radiative transfer model. Hence, in this study we used the Minnaert approximation to simplify our calculation of the disc-averaged limb-darkening and central-meridian averaged spectra following the scheme:

- As previously described, the HST/STIS and Gemini/NIFS observations were first averaged to the IRTF/SpeX resolution of $0.002 \mu\text{m}$ and sampled on a regular grid of spacing $0.001 \mu\text{m}$. The masked HST/STIS data were then averaged along the central meridian and used to scale the IRTF/SpeX observations to make the combined HST/IRTF processed observations self-consistent. The Gemini/NIFS data were also averaged along the central meridian (masking out discrete cloud features) and themselves scaled to be consistent with the combined HST/STIS and IRTF/SpeX observations.
- The averaged HST/STIS and Gemini/NIFS ‘cubes’ were then masked to exclude discrete cloud features and the remaining observations at all latitudes Minnaert-analysed to derive spectra of the disc-averaged $R_0(\lambda)$ and $k(\lambda)$. This was simplified in this case since Uranus and Neptune are so distant that the solar zenith angle and viewing zenith angle can be approximated to be the same (i.e., $\mu = \mu_0$) and hence $R = R_0 \mu^{2k-1}$.
- The fitted Minnaert parameters $R_0(\lambda)$ and $k(\lambda)$ were used to generate reconstructed spectra for HST/STIS and Gemini/NIFS at two zenith angles (0° , 61.45°), corresponding to two of the five zenith angles of the Gauss-Lobatto multiple-scattering radiative transfer model used in NEMESIS. The higher angle is large enough to ensure we fully capture the observed limb-darkening/limb-brightening, and is coincident with one of the Gauss-Lobatto quadrature angles, thus obviating the need for any interpolation (Irwin et al., 2021). However, it is not so large that the computational cost becomes excessive.

The two resulting reconstructed HST/STIS spectra, two reconstructed Gemini/NIFS spectra and the measured IRTF/SpeX central-meridian line-averaged spectrum were then used as a set of ‘measured’ observations to NEMESIS. By fitting an aerosol model to the HST/STIS and Gemini/NIFS processed spectra at 0° and 61.45° zenith angles, and extracting our best fits to the Minnaert parameters $R_0(\lambda)$ and $k(\lambda)$, we could then simply reproduce the observations at any other angle from Eq. 1, assuming that the Minnaert approximation holds at all the other zenith angles of our zenith-angle quadrature scheme, which Irwin et al. (2021) found to be a good approximation for their analysis of VLT/MUSE Neptune observations. However, we still needed an efficient way of simulating the central-meridian-averaged IRTF/SpeX spectra. We could have computed spectra at multiple locations along the central meridian and averaged these, but this would have been slow, especially near the disc edges. Instead, for each iteration we calculated spectra at two zenith angles (0° and 42.47°), extracted Minnaert parameters R_0 and k at each wavelength (using $k = (1 + \log(R_\mu/R_0)/\log(\mu))/2$, where R_0 is the nadir-calculated radiance and R_μ is the radiance calculated at $\mu = \cos(42.47^\circ)$) and used these to compute the central-meridian line-average as follows. The reason we chose the middle zenith angle of our quadrature scheme (42.47°) here, instead of the second largest (61.45°) as we did for the HST/STIS observations, is that calculations at lower zenith angles require fewer Fourier azimuth components and are more rapid; since we only needed to approximate the line-average in this case, rather than limb-darkening, the lower angle was found to be sufficiently accurate.

In Appendix B we show that the mean radiance integrated along the central meridian of a planet whose limb-darkening is well represented by the Minnaert approximation

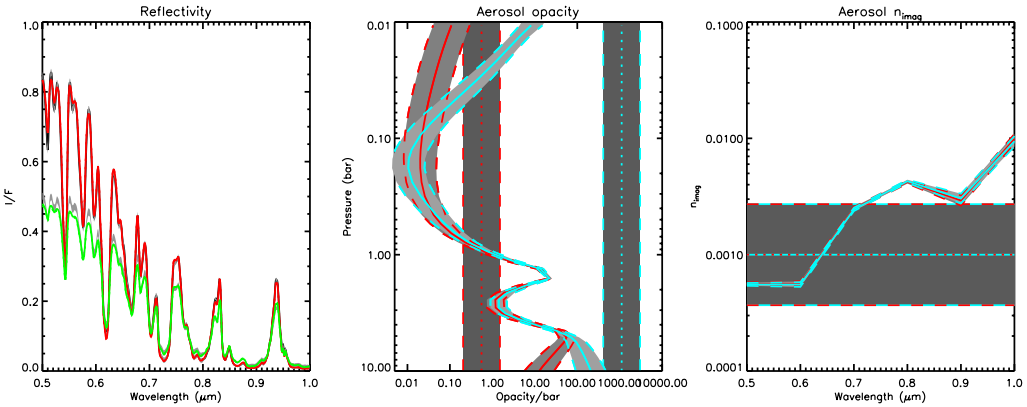


Figure 4. Example ‘bracketed’ retrieval fit to reconstructed HST/STIS spectra of Uranus from 0.5–1.0 μm at 0° and 61.45° , using two continuous *a priori* distributions of aerosols of radius 0.1 μm and variable n_{imag} spectra. The left-hand panel compares the modelled spectra (red for 0° and green for 61.45°) to the observations (grey) (N.B. The modelled fits for the two *a priori* cases are indistinguishable at this scale). The middle panel shows the retrieved aerosol profiles (in terms of opacity/bar at the reference wavelength of 0.8 μm) for the two widely separated *a priori* profiles, indicating two aerosol layers at depth. Here, the solid lines (red or cyan) show the retrieved profiles, while the dotted lines show the *a priori* profiles; the *a priori* and retrieved errors are indicated by the shaded regions and dashed lines. It can be seen that the retrievals tend back to *a priori* above and below the region of maximum sensitivity between 1 and ~ 5 bar, and thus that although we can detect a second aerosol layer at $p > \sim 4$ bar, we cannot detect whether it has a base in the 5–10-bar range. The right-hand panel shows the two fitted n_{imag} spectra, with the dotted line indicating the *a priori* value for both cases.

can be written (assuming $\mu = \mu_0$) as:

$$\overline{R}_{\text{line}} = R_0 \int_0^{\pi/2} (\cos \theta)^{2k} d\theta. \quad (2)$$

Hence, if we have an estimate of the Minnaert limb-darkening coefficient, k , and nadir radiance, R_0 , we can easily compute the corresponding central meridian line-averaged radiance. This function cannot be integrated analytically and so we pre-computed a table of $\overline{R}_{\text{line}}/R_0$ versus k and then interpolated this to the value of k derived at each wavelength. Hence, using calculations at just two angles to determine k we were able to accurately simulate the central-meridian line-averaged IRTF/SpeX observations using Eq. 2. For the HST/STIS and Gemini/NIFS data, we further verified that the central-meridian-line-average calculated from Eq. 2 using the disc-averaged Minnaert parameters was consistent with the measured IRTF/SpeX observations. For the Neptune Gemini/NIFS observations, this test necessitated some iteration on the degree to which discrete clouds were masked in order to generate the best overall set of self-consistent Minnaert coefficients. All five spectra could then be fitted simultaneously, or individual spectra fitted separately as necessary.

Our starting assumption in this analysis is that the cloud/haze structures of Uranus and Neptune are substantially the same, but that Neptune has thicker upper-tropospheric/lower-stratospheric haze. Hence, to begin with we analysed the simpler case of the Uranus observations and extended to Neptune observations later.

425 3.4 Analysis of HST/STIS Uranus observations

426 We first analysed the HST/STIS reconstructed observations of Uranus at zenith
 427 angles of 0° and 61.45° from $0.5\text{--}1.0\ \mu\text{m}$. We conducted a first-pass retrieval using a con-
 428 tinuous distribution of haze particles, in order to let the data (rather than *a priori* as-
 429 sumptions) determine the location of aerosol layers. In this first pass, the particle sizes
 430 were assumed to follow a Gamma distribution with mean radius $0.1\ \mu\text{m}$ and variance
 431 $\sigma = 0.3$. We also fitted for the imaginary refractive index spectrum (*a priori* value set
 432 to 0.001) of these particles at six wavelengths from 0.5 to $1.0\ \mu\text{m}$, step $0.1\ \mu\text{m}$, and then
 433 reconstructed the real refractive index spectrum using the Kramers-Kronig relation, as-
 434 suming the real refractive index at $0.8\ \mu\text{m}$ was fixed to a value of 1.4. The resulting com-
 435 plex refractive index spectrum was then used to calculate, using Mie theory, the extinc-
 436 tion cross-section, single-scattering albedo, and phase function spectra. However, since
 437 we expect the particles (ice and haze) to be non-spherical, the phase function spectra
 438 were approximated with combined Henyey-Greenstein phase function parameters to av-
 439 erage over features peculiar to spherical particles such as the ‘rainbow’ and ‘glory’. For
 440 the methane profile we assumed a ‘step’ function with retrievable deep abundance up
 441 to the condensation level, but with the relative humidity above the condensation level
 442 fixed to 100% and the stratospheric abundance limited to not exceed 1×10^{-4} . The re-
 443 trieval was attempted with two widely spaced *a priori* aerosol abundance profiles (as-
 444 sumed to have constant opacity/bar at all pressure levels) to achieve a ‘bracketed’ re-
 445 trieval, where the retrieved profiles will overlap where they are well constrained by the
 446 measurements and tend back to their respective *a priori* values at pressures where there
 447 is little sensitivity. Fig. 4 shows the fits to the reconstructed spectra together with the
 448 fitted aerosol abundance profiles. As can be seen, the fit struggles slightly at short wave-
 449 lengths, but otherwise we find that the HST/STIS observations are well fitted by an aerosol
 450 structure with a thin, well defined peak at ~ 1.5 bar and a second layer at pressures greater
 451 than ~ 4 bar. Although we can clearly detect the top of this deeper layer, we cannot con-
 452 strain its base pressure as the bracketed retrievals tend back to their respective *a pri-*
 453 *ori* values at pressures exceeding approximately 5–7 bar; this makes sense given that the
 454 two-way transmission to space for a vertical path rapidly falls to zero in this pressure
 455 region, even for an aerosol-free atmosphere (Fig. 3). This indication of a double-peaked
 456 cloud/haze structure was also noted by Sromovsky et al. (2019), as described earlier.

457 3.5 Analysis of combined HST/STIS and IRTF/SpeX Uranus observa- 458 tions - snippet analysis

459 Having noted that there may be two aerosol layers at depth in Uranus’s atmosphere,
 460 we attempted to fit the combined HST/STIS and IRTF/SpeX data with three aerosol
 461 layers: one based at $p > 5\text{--}7$ bar; one based at 1–2 bar; and an additional extended haze
 462 in the upper troposphere/lower stratosphere. We allowed the mean particle sizes of these
 463 constituents to vary and also fitted for the imaginary refractive index spectra of each par-
 464 ticle type. We found this to be a massively degenerate problem, with multiple combi-
 465 nations of parameters able to match the observations equally well. To attempt to pre-
 466 vent the solutions becoming stuck in local minima, we performed multiple retrievals with
 467 randomly varied *a priori* values of the pressure levels of these aerosol components and
 468 also their imaginary and real refractive indices, but were still unable to find a reliable
 469 model that was clearly better than any of the others. An additional problem is that since
 470 the HST/STIS data sets do not include estimated errors, we needed a way to set appro-
 471 priate error estimates on these data that were compatible with the published errors on
 472 the IRTF/SpeX observations and so provided appropriate weight between the two data
 473 sets. Most of all, though, we needed a way to decouple the vertical structure of the best-
 474 fitting aerosol profile from the wavelength-dependent scattering and absorption proper-
 475 ties of the particles necessary to model the spectra over a wide wavelength range.

Accepted Article

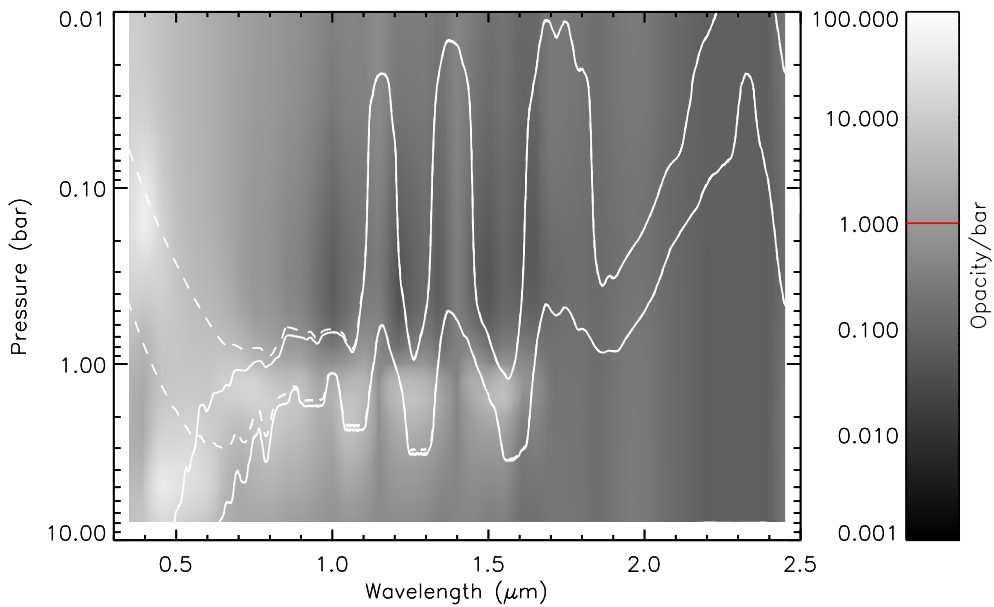


Figure 5. Contour plot of vertical aerosol structure (opacity/bar) inferred from ‘snippet’ Uranus retrievals, where for each wavelength the aerosol structure is retrieved from the wavelengths in a bin of width $0.1 \mu\text{m}$ centred on that wavelength. The contour levels are indicated in the bar on the right. From 0.3 to $0.8 \mu\text{m}$ the aerosol structure is inferred from the HST/STIS nadir spectrum, while from 0.85 to $2.5 \mu\text{m}$ the IRTF/SpeX line-averaged spectrum is used. Overplotted are white lines showing the two-way nadir transmission to space of 0.2 and 0.8 for an aerosol-free atmosphere, either excluding (solid lines) or including (dashed lines) Rayleigh-Raman scattering. The retrieved aerosol opacity/bar shown is that derived with the full Rayleigh-Raman scattering taken into account. The red line in the opacity/bar key is the assumed *a priori* value.

The method we settled on to do this was to split the HST/STIS and IRTF/SpeX spectra into a series of narrow wavelength-range ‘snippets’, each covering a wavelength bin of width $0.1 \mu\text{m}$ (narrow, but in most cases covering a reasonably large range of methane absorption strengths) and stepped by $0.05 \mu\text{m}$ to achieve Nyquist sampling. Then for each spectral snippet, we adopted a continuous distribution of aerosols with $r_{mean} = 0.1 \mu\text{m}$ and $\sigma = 0.05$, assumed that $n_{real} = 1.4$, and fitted for the imaginary refractive index, which we assumed to be constant across the moderately narrow wavelength bins chosen. For the snippet covering $0.8 - 0.9 \mu\text{m}$, which includes CIA bands of $\text{H}_2 - \text{H}_2$ and $\text{H}_2 - \text{He}$, we also fitted for the deep CH_4 abundance, which we then kept fixed for all other snippets. Hence, this snippet had to be fitted first.

For the HST/STIS ‘snippets’ we only fitted to the nadir spectrum to keep the retrievals fast, while for the IRTF/SpeX ‘snippets’ we fitted to the central-meridian line average as described earlier, modelling spectra at two zenith angles (0° and 42.47°) and combining using Eq. 2. At this point we considered what errors would be appropriate to assume for the data. Looking at the quality of the fits, we found we were able to fit the HST/STIS reflectivity spectra to a precision of $\chi^2/n \sim 1$ if we assumed the errors to be equivalent to $1/50$ of the peak reflectivity in each bin. This estimated error covers unknown systematic uncertainties from sources such as the Lucy-Richardson spatial deconvolution applied to the HST/STIS data, the inhomogeneous aerosol structure, and the methane absorption k-table parameters. While the HST/STIS data do not include error estimates, the IRTF/SpeX data do contain these, and so we added the systematic $R/50$ errors in quadrature with the measured/scaled errors. Our approach meant that: 1) we achieved a good balance between the STIS and SpeX data; 2) we did not overfit the peak radiance wavelengths; and 3) in regions of low reflectance for the SpeX data we did not attempt to fit noise.

The fitted aerosol profiles for each snippet were then combined together and plotted as a contour function of aerosol opacity/bar against the mean bin wavelength as shown in Fig. 5. Also plotted on Fig. 5 are the depths for two-way nadir transmission of 0.2 and 0.8, respectively, for an aerosol-free atmosphere and including or excluding Rayleigh and Raman scattering to give an idea of how deeply we can see at different wavelengths. We can draw a number of conclusions from Fig. 5. First of all these ‘snippet’ retrievals favour a vertically confined aerosol layer at $\sim 1.5 - 2.5$ bar for all wavelengths that penetrate deeply, except $0.4 - 0.6 \mu\text{m}$, where a much deeper aerosol layer at $p > \sim 5$ bar is indicated. The apparent base of this deeper layer is, as in the low *a priori* example shown in Fig. 4, caused by the retrieved profile tending back to *a priori* at depth. The highest opacity/bar values of these constituents are generally found between two-way transmission levels of 0.2 and 0.8, where the retrieval has most sensitivity. It is likely that the deeper $p > 5 - 7$ bar aerosol layer is present at all wavelengths, but cannot be detected at longer wavelengths due to lower reflectivity, increased gas absorption, and increased opacity of the overlying 1.5–2.5-bar aerosol layer. It should also be noted that the aerosol layer at ~ 2 bar has a much lower integrated opacity than the deeper layer, since although both have similar peak opacity/bar values, the 2-bar layer spans a smaller range of pressure. The narrow wavelength range of detectability makes it difficult to say much about the particle size of aerosols in the deepest layer. However, for the 1.5–2.5 bar layer the opacity drops slowly with wavelength, suggesting particle sizes of the order of $1 \mu\text{m}$. Finally, it can be seen that at short wavelengths (i.e., $0.3 - 1.0 \mu\text{m}$) there is general indication of an extended upper tropospheric/lower stratospheric haze, where the opacity/bar increases with altitude at pressures less than ~ 1 bar, but where the opacity drops with increasing wavelength. The retrieved wavelength dependence of this constituent of $\sim 1/\lambda^4$ suggests a very small particle size, while the increasing opacity/bar with altitude is consistent with microphysical modelling of haze production in Ice Giant atmospheres of Toledo et al. (2019, 2020), who predict a haze distribution with a fractional scale height of 2–4.

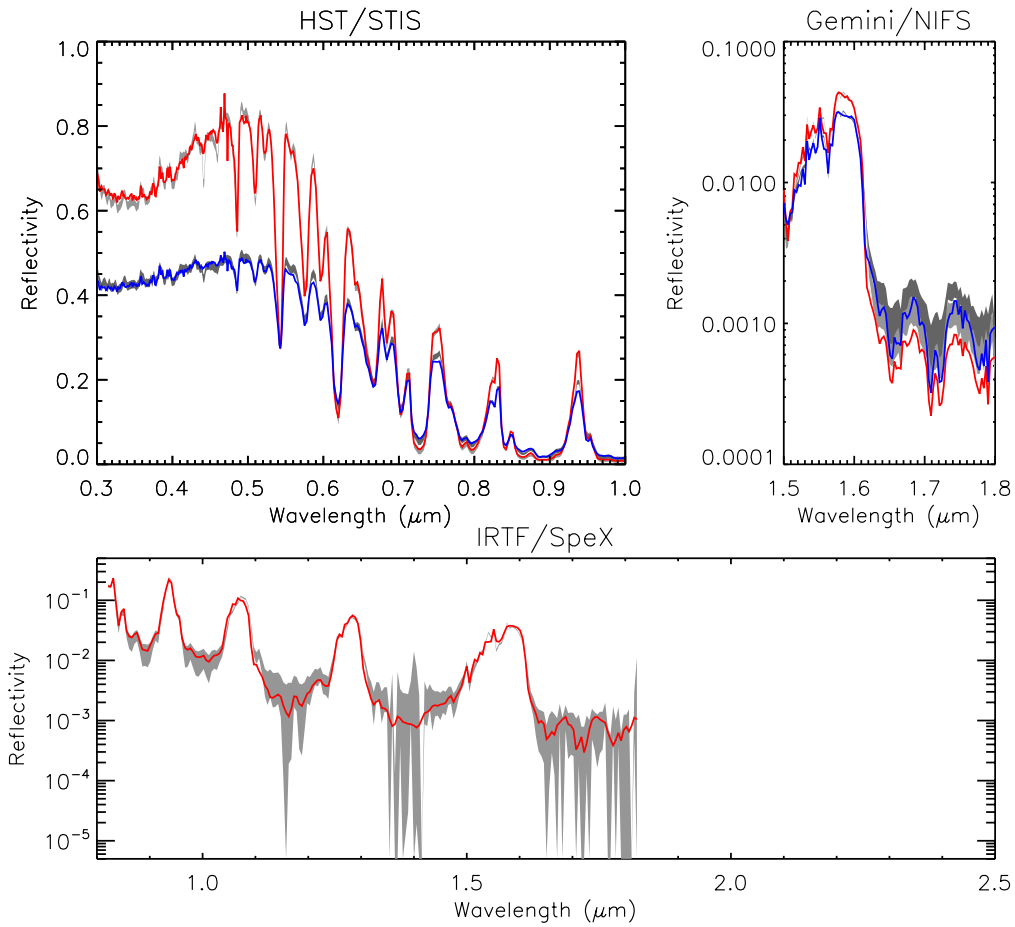


Figure 6. Example of one of the best fitted spectra for Uranus, with $\chi^2/n = 3.76$ for our assumed errors. Here, the measured spectra and assumed error range are shown in grey and the fits at 0° and 61.45° are shown in red and blue, respectively, for the HST/STIS and Gemini/NIFS observations. For the IRTF/SpeX observation, the simulated central-meridian line average is shown in red. It can be seen that we achieve a very good fit to the data for all three data sets.

529 **3.6 Simultaneous retrieval of combined HST/STIS, IRTF/SpeX, and**
 530 **Gemini/NIFS Uranus observations**

531 Having established the general vertical aerosol structure of Uranus from the first-
 532 pass retrieval, and the wavelength-dependent absorption from the snippet analysis, we
 533 moved to a parameterized model for the final retrieval. The parameterized model for Uranus
 534 included three aerosol layers: 1) a deep cloud/haze layer, ‘Aerosol-1’ fixed with a base
 535 at 10 bar (i.e., well below where we are sensitive to), with variable fractional scale height;
 536 2) a vertically-thin cloud/haze at 1–2 bar, ‘Aerosol-2’, modelled as a Gaussian distribu-
 537 tion with fixed width of ~ 0.1 scale heights; and 3) an extended tropospheric/stratospheric
 538 haze, ‘Aerosol-3’, based at 1–2 bar with a fixed fractional scale height of 2.0. Since the
 539 Aerosol-1 layer is effectively infinitely deep compared with our sensitivity functions, in
 540 this study we only quote its integrated opacity from space down to the level at which
 541 this sensitivity diminishes, which can be seen from Fig. 4 to be ~ 5 bar. Also, since the
 542 deep Aerosol-1 layer is only of importance at short wavelengths we **assumed** it to be
 543 composed predominantly of very small particles and assumed a Gamma distribution of
 544 sizes with $r_{mean} = 0.05 \mu\text{m}$ and variance, $\sigma = 0.05$. We assumed the same particle
 545 size distribution for the tropospheric/stratospheric haze particles (Aerosol-3) since the
 546 opacity of this component needs to fall as $1/\lambda^4$. For the intermediate cloud/haze layer
 547 at 1–2 bar (Aerosol-2) we tried a number of mean particle sizes of size $\sim 1 \mu\text{m}$, with vari-
 548 ance $\sigma = 0.3$. Given the degenerate nature of this problem, we first fitted to the HST/STIS
 549 data alone in the wavelength range $0.8\text{--}0.9 \mu\text{m}$ to constrain the deep methane abundance
 550 and pressure of the 1–2 bar Aerosol-2 component, which we then used as the *a priori* in
 551 subsequent all-wavelength retrievals. To do this, we generated a set of 30 retrievals with
 552 randomly chosen values of the Aerosol-1 fractional scale heights (in range 0.05–0.15), ran-
 553 domly chosen Aerosol-2 mean particle radii (in range 0.1–4.0 μm) and then fitted for the
 554 opacities of all three constituents, their mean imaginary refractive indices (assumed con-
 555 stant in $0.8\text{--}0.9 \mu\text{m}$ range), together with the deep methane abundance, setting the rel-
 556 ative humidity above the condensation level to 100% and limiting the stratospheric mole
 557 fraction to not exceed 10^{-4} . The real refractive index of all components was assumed
 558 to be 1.4 (other values for the real refractive index were tried, but were not found to more
 559 or less appropriate). Then, for the best-fitting aerosol/methane solutions to the $0.8\text{--}0.9$
 560 μm region (achieving $\chi^2/n < 1$), we fitted the entire combined STIS/SpeX/NIFS dataset
 561 using these retrievals as the *a priori*, keeping the mean Aerosol-2 particle size fixed, but
 562 fitting again for all other properties and also for the imaginary refractive index spectra
 563 from $0.2\text{--}1.9 \mu\text{m}$, with step $0.1 \mu\text{m}$ and assuming $n_{real} = 1.4$ at $0.8 \mu\text{m}$. We again re-
 564 constructed n_{real} at other wavelengths using the Kramers-Kronig relation and then gen-
 565 erated cross-section spectra, single-scattering albedo spectra and phase function spec-
 566 tra from Mie theory, approximating the phase functions with double Henyey-Greenstein
 567 functions.

568 For the HST/STIS spectra at zenith angles of 0° and 61.45° we modelled 500 points
 569 from $0.2\text{--}1.0 \mu\text{m}$, with 300 points from 0.2 to $0.5 \mu\text{m}$, spaced every $0.001 \mu\text{m}$ to fully cap-
 570 ture the Raman-scattering component, and the remaining 200 points equally spaced from
 571 0.5 to $1.0 \mu\text{m}$. Although the HST/STIS data do not extend below $0.3 \mu\text{m}$, we still needed
 572 to model the spectra from $0.2 \mu\text{m}$ upwards in order to compute the effect of sunlight be-
 573 ing scattered to the longer wavelengths observed by STIS. We generated synthetic ‘mea-
 574 sured’ radiances at $\lambda < 0.3 \mu\text{m}$ having the same reflectivity as observed at $0.3 \mu\text{m}$, but
 575 with very large errors in order that NEMESIS did not try to fit to them, but did include
 576 their Raman-scattering effect on the measured wavelengths. For wavelengths longer than
 577 $0.3 \mu\text{m}$, we set the reflectivity errors to be equivalent to 1/50 of the reflectivity of the
 578 nearest peak, but in addition prevented the reflectivity error from exceeding a value of
 579 0.01 in order to force the model to fit the data well near $\sim 0.5 \mu\text{m}$, where the observed
 580 reflectances peak. We also halved the errors in the $0.8\text{--}0.9 \mu\text{m}$ range to ensure good fit
 581 at the wavelengths best able to differentiate between methane abundance and 1–2-bar
 582 aerosol layer (Aerosol-2) pressure.

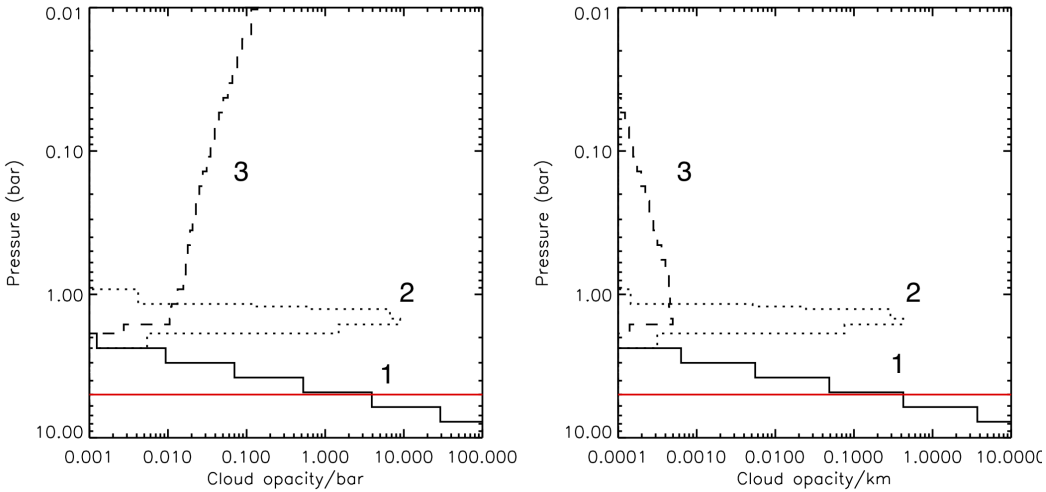


Figure 7. Fitted vertical aerosol structure for Uranus’s atmosphere from our example best-fit retrieval, presented in terms of opacity/bar (left) and opacity/km (right) at $0.8 \mu\text{m}$. The deep aerosol layer (Aerosol-1) is shown as a solid line, the middle aerosol layer (Aerosol-2) as a dotted line, and the extended tropospheric/stratospheric haze (Aerosol-3) as a dashed line. The red line marks the 5-bar level, which is roughly the level where our sensitivity runs out.

For the Gemini/NIFS data, we selected 100 wavelengths equally spaced between 1.5 and $1.8 \mu\text{m}$, again at 0° and 61.45° zenith angles. The errors were set to $1/100$ of the maximum reflectivity of the $1.55 \mu\text{m}$ peak to give these data slightly more weight in the final fit than the IRTF/SpeX data since they contain clearer limb-darkening information.

Finally, for the IRTF/SpeX data we selected 200 wavelengths, equally spaced between 0.8 and $1.9 \mu\text{m}$ (longer wavelengths were discounted as they can be seen in Fig. 1 to have low SNR), and set the errors to be $1/50$ of the nearest peak reflectance, added in quadrature with the published errors.

Figure 6 shows one of our best fits to the combined data set where we can see that we match the observed reflectivity spectra very well. The vertical cloud/haze structure retrieved in this case is shown in Fig. 7, both in terms of opacity/bar and opacity/km at $0.8 \mu\text{m}$ (see Appendix C for an explanation of the different opacity units), which is comprised of a deep aerosol layer (Aerosol-1) based at 10 bar with fractional scale height 0.11 and integrated opacity to 5 bar (at $0.8 \mu\text{m}$) 0.81, a middle vertically-thin aerosol layer (Aerosol-2) at 1.48 bar and opacity 3.1, composed of particles of mean radius $0.6 \mu\text{m}$, and an extended haze (Aerosol-3), based at 1.6 bar with fixed fractional scale height 2.0 and retrieved opacity 0.03. The retrieved methane mole fraction is 3.0% and the relative humidity above the condensation level was fixed to 100%. It should be stressed here that there is no single solution that clearly fits better than all others. As we have performed multiple slightly perturbed retrievals there is a general class of solutions that fit best, of which this is one representative example. The complete set of retrieved parameters is shown in Fig. 8 and the range of solutions and errors are listed in Table 2.

The estimated n_{imag} spectra for the three constituents are shown in Fig. 9. Here, we have taken the fitted n_{imag} spectra for the best-fitting cases and combined them together to give an idea of the range of acceptable solutions, together with two estimates of the optimal solution and the fitted spectra from our example best-fitting case, which

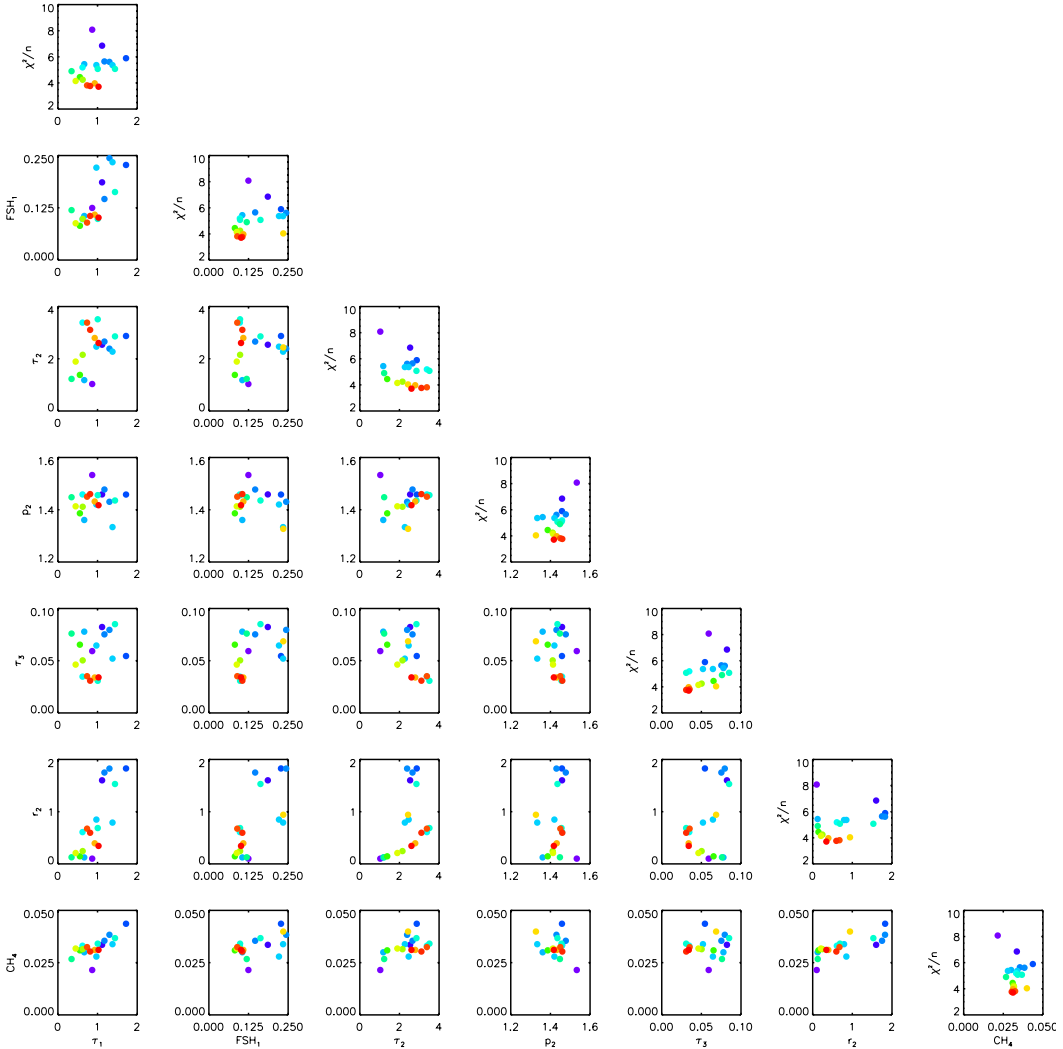


Figure 8. ‘Corner’ plot of 30 retrievals of the combined HST/STIS, IRTF/SpeX and Gemini/NIFS Uranus dataset with $\chi^2/n < 10$. Note that for the opacity of the Aerosol-1 layer, τ_1 , the opacity plotted is that integrated from space down to the 5-bar pressure level. The data points are colour-coded by the χ^2/n of the fit, with red fitting best and purple worst. Along the leading diagonal, instead of plotting the marginalised errors as would be usual for such plots, we plot χ^2/n as a function of fitted parameter, again colour-coded with red points having the lowest χ^2/n and purple points the highest. Although some parameters are better constrained than others, it can be seen that there is little cross-correlation between any of the fitted parameters.

Table 2. Fitted model parameters to combined HST/STIS, IRTF/SpeX and Gemini/NIFS data. Note that the fractional scale height of the Gaussian-shaped Aerosol-2 layer (and Aerosol-4 layer for Neptune) was fixed at 0.1 and the fractional scale height of the Aerosol-3 layer was fixed at 2.0. Note also that the quoted opacities for the Aerosol-1 layer, τ_1 are integrated from space down to a pressure level of 5 bar.

Parameter	Uranus	Neptune
Opacity τ_1 (at 0.8 μm)	0.8 – 1.1	0.5 – 0.8
Frac. Sc. Ht. fsh_1	0.08 – 0.12	0.14 – 0.18
Radius r_1	0.05 μm (fixed)	0.05 μm (fixed)
Pressure p_2	1.4 – 1.5 bar	2.0 – 2.1 bar
Opacity τ_2 (at 0.8 μm)	2.0 – 3.5	1 – 2
Radius r_2	0.3 – 0.8 μm	0.3 – 0.8 μm
Pressure p_3	1.6 bar (fixed)	1.6 bar (fixed)
Opacity τ_3 (at 0.8 μm)	0.03 ± 0.01	0.04 ± 0.01
Radius r_3	0.05 μm (fixed)	0.05 μm (fixed)
Pressure p_4	n/a	0.2 bar (fixed)
Opacity τ_4 (at 0.8 μm)	n/a	0.030 ± 0.005
Radius r_4	n/a	$2.5 \pm 0.5 \mu\text{m}$
Deep CH ₄ mole fraction	$3 \pm 1 \%$	$7 \pm 1 \%$
Tropopause CH ₄ RH	100% (fixed)	$35 \pm 5 \%$

are listed in Table 3. As can be seen there are certain features common to all the best-fitting retrieved imaginary refractive index spectra, namely:

1. The lowest aerosol layer (Aerosol-1) has very low n_{imag} at 0.4–0.5 μm , which increases either side, but never gets very big. This means this layer is bright and highly scattering at 0.5 μm , but less so either side. Since we chose this layer to be composed of very small particles its contribution diminishes rapidly at longer wavelengths.
2. The 1–2-bar aerosol layer (Aerosol-2) has lowest n_{imag} from 0.4–0.6 μm , which then increases sharply on either side. This increase is necessary to give sufficient ultraviolet (UV) absorption and also to reproduce the observed limb-darkening/limb-brightening seen at longer wavelengths. The retrieved mean radius of the particles in this layer of $\sim 1 \mu\text{m}$, makes them moderately forward-scattering at 0.5 μm , lowering their back-scatter and thus contribution to the reflected spectra, and increasing their ‘transparency’ to allow light to be reflected from the deeper $p > 5\text{--}7$ bar Aerosol-1 layer.
3. The tropospheric/stratospheric haze (Aerosol-3) n_{imag} spectrum is moderately similar to that of the Aerosol-2 layer, but is less well constrained.

It should be noted that the fitted n_{imag} spectra can alias all sorts of other deficiencies in the forward model, such as inaccuracies in the methane absorption data, assumed/estimated particle size, or vertical cloud/haze parameterisation, and so not all features in these spectra may necessarily reflect what we would measure were we able to make *in situ* observations of the particle scattering properties. However, the similarity between the retrieved Aerosol-2 and Aerosol-3 spectra and the generally higher values of n_{imag} leads us to posit that the middle Aerosol-2 layer is not a pure condensed cloud, but instead is a region of photochemically-produced haze transported from the upper atmosphere and perhaps mixed with some methane ice. This is a point we shall return to later. For the lower Aerosol-1 layer, this has a lower n_{imag} and we posit that this is actually the H₂S condensation layer (rather than an NH₄SH layer, suggested by Sromovsky et al. (2019)), condensing onto dark haze particles and thus not conservatively scattering. We did attempt to model

Table 3. Estimated n_{imag} spectra for Uranus aerosols. Here, for each aerosol type, ‘Mean 1’ is the weighted average for all best-fitting retrieved spectra, while ‘Mean 2’ are the averages of the contour maps shown in Fig. 9. ‘Sample’ is the retrieved spectra from the representative best-fitting sample case shown for each planet.

$\lambda(\mu\text{m})$	Aerosol-1 Mean 1	($> 5\text{-}7$ bar) Mean 2	Sample	Aerosol-2 Mean 1	(1–2 bar) Mean 2	Sample	Aerosol-3 Mean 1	(extended) Mean 2	Sample
0.3	1.95×10^{-3}	5.62×10^{-4}	3.88×10^{-4}	1.10×10^{-2}	9.90×10^{-3}	8.59×10^{-3}	3.07×10^{-3}	2.98×10^{-3}	3.31×10^{-3}
0.4	6.73×10^{-5}	6.17×10^{-5}	2.19×10^{-5}	1.61×10^{-3}	1.64×10^{-3}	1.44×10^{-3}	1.50×10^{-3}	1.48×10^{-3}	1.51×10^{-3}
0.5	1.10×10^{-6}	1.66×10^{-5}	1.00×10^{-6}	1.35×10^{-3}	1.03×10^{-3}	1.07×10^{-3}	1.91×10^{-4}	1.90×10^{-4}	2.54×10^{-4}
0.6	2.96×10^{-4}	2.36×10^{-4}	2.30×10^{-4}	9.65×10^{-4}	1.10×10^{-4}	1.86×10^{-5}	1.70×10^{-4}	9.34×10^{-5}	2.99×10^{-4}
0.7	1.39×10^{-3}	7.88×10^{-4}	9.66×10^{-4}	1.37×10^{-3}	3.78×10^{-4}	8.37×10^{-4}	1.38×10^{-3}	2.59×10^{-4}	4.79×10^{-4}
0.8	2.12×10^{-4}	1.99×10^{-4}	6.88×10^{-5}	4.89×10^{-3}	1.69×10^{-3}	5.03×10^{-3}	7.74×10^{-3}	8.92×10^{-4}	7.96×10^{-4}
0.9	7.21×10^{-4}	2.51×10^{-4}	3.04×10^{-4}	4.24×10^{-3}	8.63×10^{-4}	3.84×10^{-3}	7.87×10^{-3}	3.21×10^{-3}	2.60×10^{-3}
1.0	2.46×10^{-3}	1.52×10^{-3}	6.26×10^{-4}	1.13×10^{-2}	7.70×10^{-3}	1.29×10^{-2}	1.52×10^{-3}	1.60×10^{-3}	1.14×10^{-3}
1.1	5.18×10^{-2}	1.16×10^{-2}	5.08×10^{-3}	6.91×10^{-3}	2.29×10^{-3}	3.92×10^{-4}	8.38×10^{-2}	1.97×10^{-3}	6.73×10^{-2}
1.2	3.23×10^{-3}	9.75×10^{-3}	2.37×10^{-3}	5.25×10^{-2}	3.55×10^{-3}	9.09×10^{-3}	7.20×10^{-2}	1.79×10^{-3}	1.20×10^{-1}
1.3	7.82×10^{-3}	5.05×10^{-3}	3.72×10^{-3}	1.72×10^{-2}	4.62×10^{-3}	1.12×10^{-2}	1.16×10^{-2}	2.37×10^{-3}	7.53×10^{-2}
1.4	4.46×10^{-3}	3.78×10^{-3}	1.18×10^{-3}	5.20×10^{-1}	3.46×10^{-1}	2.52×10^{-1}	2.16×10^{-1}	9.62×10^{-3}	2.46×10^{-1}
1.5	3.20×10^{-4}	3.52×10^{-4}	1.45×10^{-4}	1.06×10^{-1}	9.83×10^{-2}	6.72×10^{-2}	2.19×10^{-2}	6.77×10^{-3}	2.31×10^{-2}
1.6	4.19×10^{-4}	4.89×10^{-4}	2.01×10^{-4}	6.21×10^{-2}	5.65×10^{-2}	5.87×10^{-2}	3.53×10^{-2}	3.34×10^{-2}	3.62×10^{-2}
1.7	2.64×10^{-3}	2.49×10^{-3}	1.49×10^{-3}	1.23×10^{-1}	7.95×10^{-2}	4.01×10^{-2}	1.19×10^{-3}	2.28×10^{-3}	1.85×10^{-3}
1.8	6.98×10^{-4}	1.70×10^{-3}	6.35×10^{-4}	2.75×10^{-3}	4.89×10^{-3}	3.07×10^{-3}	7.35×10^{-4}	8.57×10^{-4}	9.75×10^{-4}
1.9	1.02×10^{-3}	1.00×10^{-3}	5.47×10^{-4}	1.47×10^{-3}	1.12×10^{-3}	1.67×10^{-3}	8.44×10^{-4}	9.53×10^{-4}	9.42×10^{-4}

Table 4. Estimated n_{imag} spectra for Neptune aerosols. Again, for each aerosol type, ‘Mean 1’ is the weighted average for all best-fitting retrieved spectra, while ‘Mean 2’ are the averages of the contour maps shown in Fig. 9. ‘Sample’ is the retrieved spectra from the representative best-fitting sample case shown for each planet.

$\lambda(\mu\text{m})$	Aerosol-1 Mean 1	($> 5\text{-}7$ bar) Mean 2	Sample	Aerosol-2 Mean 1	(1–2 bar) Mean 2	Sample	Aerosol-3 Mean 1	(extended) Mean 2	Sample
0.3	2.89×10^{-4}	1.87×10^{-4}	1.52×10^{-4}	3.13×10^{-3}	3.46×10^{-3}	3.40×10^{-3}	6.39×10^{-3}	4.78×10^{-3}	4.46×10^{-3}
0.4	1.00×10^{-5}	1.57×10^{-5}	5.27×10^{-6}	1.13×10^{-3}	1.26×10^{-3}	1.27×10^{-3}	1.01×10^{-2}	8.23×10^{-3}	7.62×10^{-3}
0.5	1.19×10^{-5}	6.76×10^{-6}	2.16×10^{-6}	1.61×10^{-3}	1.49×10^{-3}	1.79×10^{-3}	5.47×10^{-3}	4.66×10^{-3}	3.14×10^{-3}
0.6	4.54×10^{-4}	1.91×10^{-4}	2.02×10^{-4}	1.76×10^{-4}	1.71×10^{-4}	9.71×10^{-5}	3.56×10^{-3}	2.19×10^{-3}	1.31×10^{-3}
0.7	1.13×10^{-3}	9.28×10^{-4}	1.14×10^{-3}	2.22×10^{-3}	3.03×10^{-4}	2.24×10^{-4}	1.71×10^{-2}	1.46×10^{-2}	1.77×10^{-2}
0.8	1.13×10^{-3}	1.51×10^{-3}	1.79×10^{-3}	1.48×10^{-3}	2.83×10^{-4}	2.19×10^{-4}	3.61×10^{-2}	3.53×10^{-2}	3.48×10^{-2}
0.9	4.00×10^{-4}	3.62×10^{-4}	3.83×10^{-4}	3.52×10^{-4}	2.97×10^{-4}	3.09×10^{-4}	4.13×10^{-2}	3.21×10^{-2}	4.06×10^{-2}
1.0	1.64×10^{-3}	1.46×10^{-3}	1.75×10^{-3}	6.36×10^{-3}	2.16×10^{-3}	6.65×10^{-3}	4.66×10^{-3}	4.80×10^{-3}	2.39×10^{-3}
1.1	2.28×10^{-3}	2.43×10^{-3}	2.43×10^{-3}	8.36×10^{-3}	7.09×10^{-3}	1.07×10^{-2}	5.29×10^{-3}	1.62×10^{-3}	1.82×10^{-3}
1.2	3.35×10^{-3}	2.57×10^{-3}	3.11×10^{-3}	3.73×10^{-2}	1.97×10^{-2}	2.68×10^{-2}	4.05×10^{-2}	1.44×10^{-3}	1.75×10^{-3}
1.3	1.45×10^{-2}	4.40×10^{-3}	5.66×10^{-3}	3.28×10^{-2}	2.21×10^{-2}	3.55×10^{-2}	2.49×10^{-2}	2.34×10^{-3}	2.50×10^{-3}
1.4	6.87×10^{-3}	2.69×10^{-3}	3.71×10^{-3}	5.31×10^{-1}	6.08×10^{-2}	3.50×10^{-1}	3.73×10^{-1}	2.45×10^{-2}	1.26×10^{-2}
1.5	6.23×10^{-4}	4.53×10^{-4}	4.43×10^{-4}	5.33×10^{-2}	1.03×10^{-2}	3.79×10^{-2}	3.10×10^{-1}	3.16×10^{-1}	2.77×10^{-1}
1.6	4.76×10^{-4}	3.41×10^{-4}	3.41×10^{-4}	3.85×10^{-2}	3.66×10^{-2}	4.54×10^{-2}	3.46×10^{-1}	4.04×10^{-1}	3.26×10^{-1}
1.7	1.46×10^{-2}	1.34×10^{-3}	1.09×10^{-3}	9.55×10^{-2}	9.45×10^{-3}	5.42×10^{-2}	2.89×10^{-1}	9.08×10^{-2}	3.57×10^{-1}
1.8	2.53×10^{-3}	1.05×10^{-3}	9.41×10^{-4}	2.69×10^{-3}	2.10×10^{-3}	2.70×10^{-3}	2.27×10^{-1}	6.91×10^{-3}	3.76×10^{-2}
1.9	3.84×10^{-3}	9.95×10^{-4}	1.08×10^{-3}	1.61×10^{-3}	1.13×10^{-3}	1.32×10^{-3}	2.88×10^{-1}	2.07×10^{-3}	6.00×10^{-2}
2.0	1.28×10^{-3}	9.79×10^{-4}	1.19×10^{-3}	1.16×10^{-3}	1.01×10^{-3}	9.86×10^{-4}	8.22×10^{-1}	1.57×10^{-3}	9.92×10^{-1}
2.1	1.08×10^{-3}	9.89×10^{-4}	1.06×10^{-3}	1.07×10^{-3}	1.00×10^{-3}	8.06×10^{-4}	1.59×10^{-2}	1.69×10^{-3}	1.38×10^{-2}
2.2	1.12×10^{-3}	9.82×10^{-4}	9.00×10^{-4}	1.03×10^{-3}	1.00×10^{-3}	8.60×10^{-4}	2.68×10^{-3}	1.18×10^{-3}	2.59×10^{-3}
2.3	9.54×10^{-4}	9.76×10^{-4}	1.03×10^{-3}	9.92×10^{-4}	1.00×10^{-3}	7.84×10^{-4}	1.42×10^{-3}	1.02×10^{-3}	1.41×10^{-3}
2.4	9.04×10^{-4}	1.02×10^{-3}	1.04×10^{-3}	1.01×10^{-3}	1.00×10^{-3}	7.71×10^{-4}	1.10×10^{-3}	1.00×10^{-3}	1.12×10^{-3}

these data with a conservatively-scattering cloud/haze, but found that there was a detectable contribution from this component at longer visible wavelengths, which from the ‘snippet’ analysis we think is unlikely. Instead, this Aerosol-1 layer is only visible from 0.4 to 0.7 μm due to: a) this layer being most reflective at these wavelengths; b) at longer (and shorter) wavelengths it is obscured by the thicker, and increasingly less scattering overlying 1–2-bar Aerosol-2 layer; and c) we have assumed a small particle size to make sure the extinction cross-section falls as $1/\lambda^4$. Of course it is entirely possible that the particles in the Aerosol-1 layer are actually larger than the value of 0.05 μm we have assumed here, in which case the retrieval model would likely have estimated larger n_{imag} at longer wavelengths in order to reduce the reflectivity to a sufficiently small values. Typical sizes of droplets in clouds on Earth are many orders of magnitude larger than value of 0.05 μm assumed here, although such clouds are formed of different condensate at very different pressures and temperatures so may not be representative. However, it is worth emphasising that the actual mean radius of the Aerosol-1 particles is very uncertain and is not unambiguously constrained by these data.

One final point to make here is that the computed opacity/km of the Aerosol-2 layer at 0.8 μm is rather low, peaking at about 1.0–10 km^{-1} . This underlines our suggestion that, assuming these are layers are homogeneous, they are extended photochemically-produced haze layers, rather than opaque cloud decks, since we would be able to see many hundreds of metres in all directions were we to be present in these layers.

3.7 Analysis of IRTF/SpeX Neptune H+K band observations

Having found a good fit to our Uranus observations, we then turned our attention to the Neptune observations. Before analysing the combined HST/STIS, IRTF/SpeX and Gemini/NIFS data sets we first of all sought to understand the gross differences between the Uranus and Neptune IRTF/SpeX observations, in particular the high reflectivities seen at methane absorption wavelengths longer than 1 μm for Neptune, but not seen for Uranus.

The 1.65–2.4 μm region is particularly good for determining upper atmospheric aerosol density since the strong methane absorption band at 1.7 μm lies next to strong H₂-H₂/H₂-He collision-induced absorption bands centred at 2.1 μm . The weighting functions of the methane-absorbing and hydrogen/helium-CIA-absorbing regions cover a similar range of pressure levels in the upper troposphere (0.6–0.1 bar) and thus this spectral region can be used to resolve the degeneracy between aerosol opacity and upper tropospheric methane abundance and retrieve reliable estimates of both (Roman et al., 2018).

Fig. 10 shows a ‘bracketed’ retrieval to the IRTF/SpeX spectrum in the wavelength range 1.65–2.4 μm , assuming two widely-separated continuous distributions of small aerosols of mean radius 0.1 μm , variance $\sigma = 0.3$, and fixed $n_{\text{imag}} = 0.1$. As can be seen, a sharply peaked aerosol profile is favoured, peaking at ~ 0.2 bar, with the local methane relative humidity retrieved to be $\sim 32\%$. At first glance this fitted aerosol structure seems contrary the results of microphysical modelling (Toledo et al., 2019, 2020) where, since photochemically-produced haze particles are produced in the stratosphere and then progressively mixed to deeper and deeper pressures, we expect a distribution with decreasing opacity/bar with increasing pressure. To understand what was going on here, we needed to examine the reflectivities over a wider wavelength range, which, as we did for Uranus, we achieved with a Neptune ‘snippet’ analysis, which we outline in the next section.

3.8 Analysis of combined HST/STIS and IRTF/SpeX Neptune observations - snippet analysis

As for our Uranus analysis, we split the HST/STIS and IRTF/SpeX observations into small, manageable ‘snippets’ of wavelength width 0.1 μm , spaced every 0.05 μm and

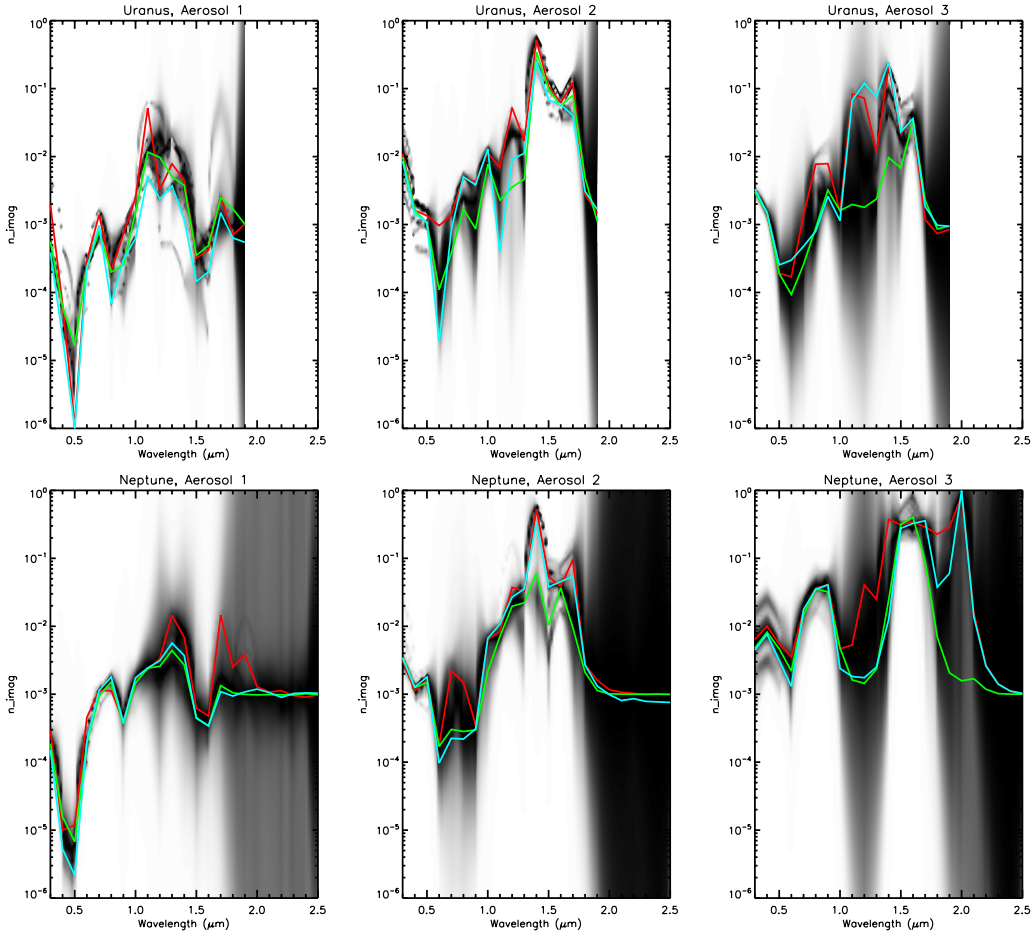


Figure 9. Fitted n_{imag} spectra for Uranus (top row) and Neptune (bottom row) for the lower cloud/haze at 10 bar (Aerosol-1), the middle cloud/haze at 1–2 bar (Aerosol-2) and the vertically-extended upper tropospheric/lower stratospheric haze (Aerosol-3). The filled contour plots show the linear addition of the best-fitting imaginary index distributions. Over-plotted on these distributions are the extracted mean n_{imag} spectra, where red are the weighted averages of all best-fitting retrieved spectra, green are the contour-map-weighted averages, and cyan are the retrieved spectra from the representative retrieval case shown for each planet. These spectra are listed in Tables 3 and Tables 4. N.B., the *a priori* value of n_{imag} was set to 0.001 and this is the value the retrievals tend back to when the data are no longer constraining. The IRTF/SpeX data for Uranus were truncated at 1.9 μm as it can be seen from Fig. 1 that the observations are too noisy to use at longer wavelengths.

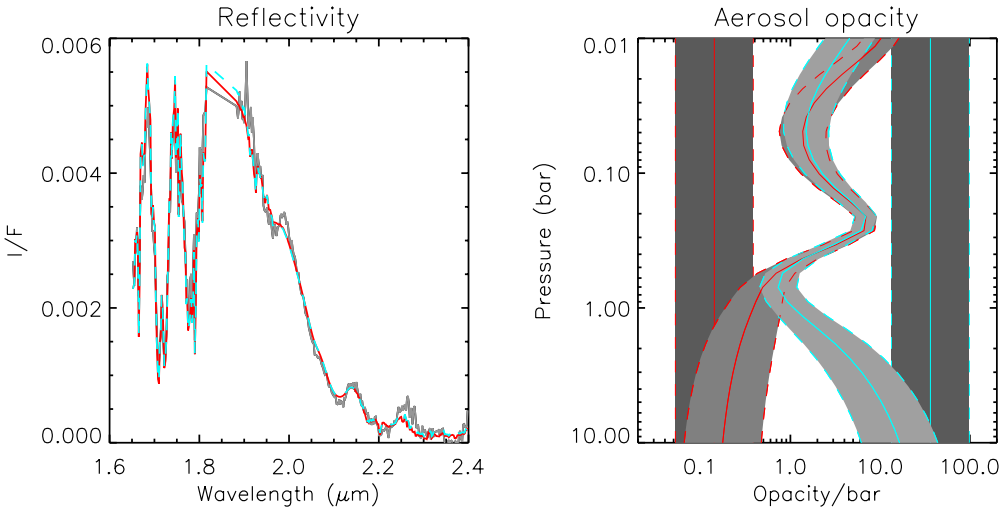


Figure 10. Example ‘bracketed’ fits to the longwave part of the IRTF/SpeX spectrum of Neptune using two different continuous *a priori* distributions of aerosol particles of radius $0.1 \mu\text{m}$ and fixed $n_{\text{imag}} = 0.1$. The left panel compares the modelled spectra (red and cyan-dashed for two different priors) to that observed (grey), while the right panel shows the retrieved aerosol profiles for the two different *a priori*, indicated in red and cyan respectively, showing that the spectrum is best fit in both cases with a layer that has peak opacity just below the tropopause near 0.2 bar. Note that in the right-hand panel the *a priori* and retrieved error ranges are shaded in grey and edged by dashed coloured lines.

retrieved the vertical aerosol profile for a Gamma distribution of particles with mean radius $0.1 \mu\text{m}$ and variance $\sigma = 0.05$, varying also the imaginary refractive index n_{imag} and keeping $n_{\text{real}} = 1.4$. The resulting retrieved aerosol vertical/wavelength structure is shown in Fig. 11. As can be seen, the aerosol structure shares many similarities with the equivalent Uranus results (Fig. 5), with a deep Aerosol-1 layer seen at $p > \sim 4$ bar and a middle Aerosol-2 layer at ~ 2 bar (slightly deeper than for Uranus). At short wavelengths it can also be seen that the opacity/bar increases with height in the upper troposphere/lower stratosphere, and decays rapidly with wavelength, consistent with our expectations with small, photochemically-produced haze particles. However, for Neptune there is clearly also a component of vertically confined particles centred at ~ 0.2 bar, which must have a larger mean size in order that their opacity does not drop noticeably with wavelength. We believe here that we are detecting in the IRTF/SpeX data the signature of an additional component of larger-sized particles at ~ 0.2 bar, which we surmise to be condensed methane ice. Such upper tropospheric methane condensation clouds are often seen in Neptune observations, especially in the regions at $20\text{--}40^\circ\text{N}$ and $20\text{--}40^\circ\text{S}$ and are seen to be highly temporally and spatially variable. We have tried to mask out such regions in the HST/STIS and Gemini/NIFS data. However, since we do not have an image of Neptune observed simultaneously with the IRTF/SpeX central-meridian line average, we do not know how significant this component of upper tropospheric methane clouds is in the recorded IRTF/SpeX spectrum. Hence, we need to be careful when interpreting the IRTF/SpeX Neptune data, especially when used in combination with the other data sets. However, the good correspondence between the scaled IRTF/SpeX and Gemini/NIFS data sets, achieved, as described earlier, by optimising the cut-off level for bright clouds in the Gemini/NIFS data, reassures us that these data are reasonably self-consistent.

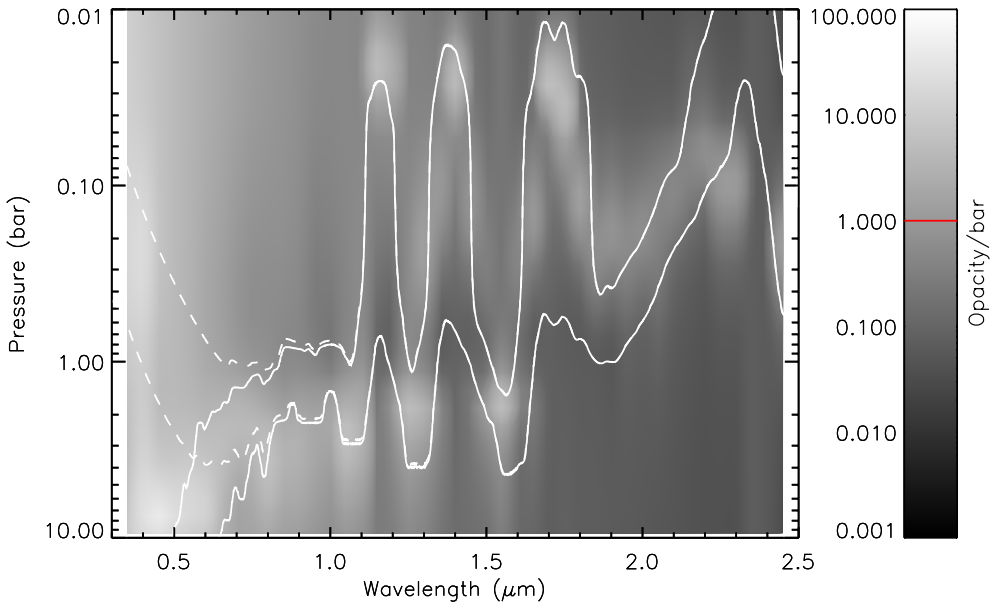


Figure 11. As Fig. 5, but for Neptune, showing a contour plot of vertical aerosol structure (opacity/bar) inferred from our ‘snippet’ Neptune retrievals, where for each wavelength the aerosol structure is retrieved from the wavelengths in a bin of width $0.1\text{ }\mu\text{m}$ centred on that wavelength. The red line in the opacity/bar key is again the assumed *a priori* value.

3.9 Simultaneous retrieval of combined HST/STIS, IRTF/SpeX, and Gemini/NIFS Neptune observations

Having found from the ‘snippet’ analysis that our expected aerosol solution for Neptune was very similar to that for Uranus, we attempted to fit the combined STIS/SpeX/NIFS Neptune data set in the same way, except that we also added a thin layer of methane ice centred at 0.2 bar and with variable mean radius and fixed variance $\sigma = 0.3$ (N.B. although we have modelled this layer as being homogeneous, it is also possible that this component is composed of sub-pixel-scale clouds). We first fitted the $0.8\text{--}0.9\text{ }\mu\text{m}$ region separately with a range of randomly varied *a priori* Aerosol-1 fractional scale heights and Aerosol-2 base pressures and radii and used those achieving $\chi^2/n < 1$ as the *a priori* for the full retrievals, fixing the Aerosol-2 radii. Figure 12 shows one of our best fits to the combined Neptune data set, where we can see that we again match the observed reflectivities and limb-darkening very well. The vertical aerosol structure retrieved for this case is shown in Fig. 13, which is comprised of a deep Aerosol-1 layer at fixed base pressure 10 bar with fractional scale height 0.18 and integrated opacity to 5 bar (at $0.8\text{ }\mu\text{m}$) 0.81 (coincidentally the same value as for our sampled Uranus retrieval shown earlier), a compact Aerosol-2 layer at 2.08 bar and opacity 1.8 composed of particles of mean radius $0.68\text{ }\mu\text{m}$, an extended haze (Aerosol-3), based at 1.6 bar with fixed fractional scale height 2.0 and opacity 0.05, and a detached methane ice aerosol layer near the tropopause (0.2 bar), of opacity 0.03 comprised of particles of mean radius $2.8\text{ }\mu\text{m}$. The methane deep mole fraction is 7.7% and relative humidity at the tropopause is 34% in this case. It should be stressed here that once again there is no single solution that fits better than all others; as we have performed multiple slightly perturbed retrievals there is a general class of solutions that fit best, of which this is one representative example. The complete

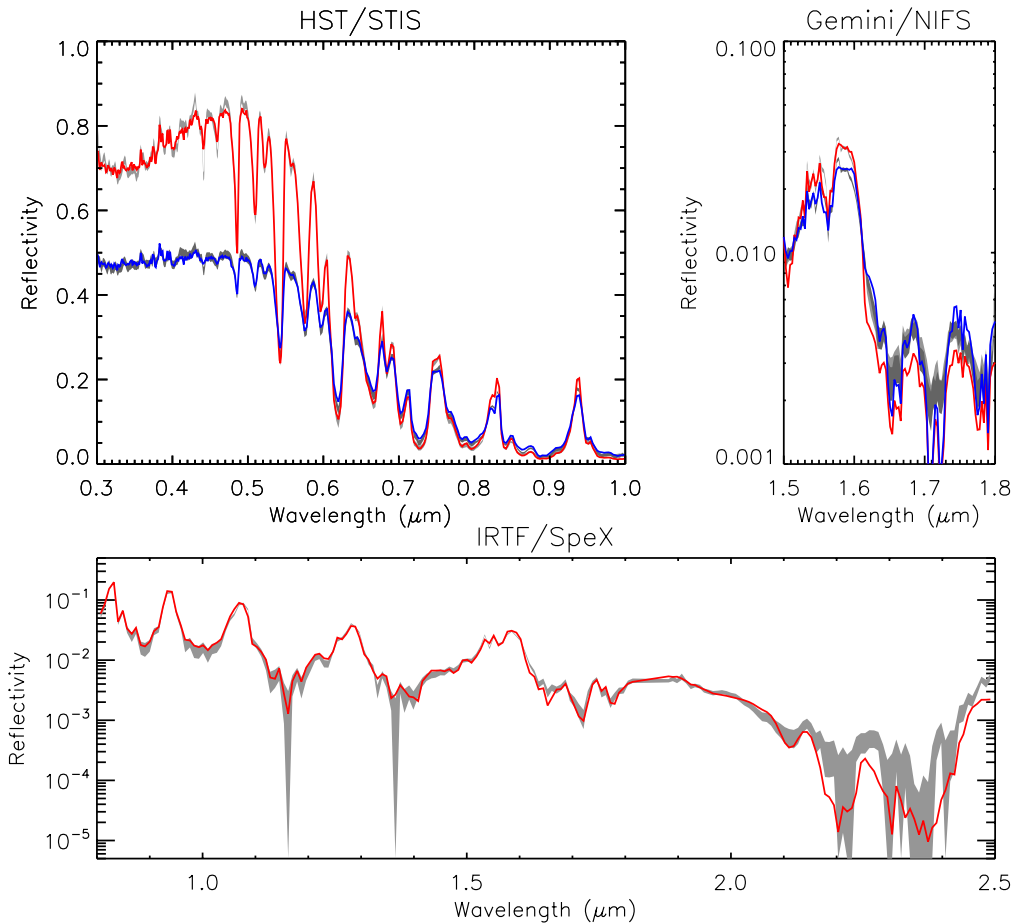


Figure 12. Example of one of the best fitted spectra for Neptune, with $\chi^2/n = 2.79$ for our assumed errors. Here, the measured spectra and assumed error range are shown in grey and the fits at 0° and 61.45° are shown in red and blue, respectively, for both the HST/STIS and Gemini/NIFS observations. For the IRTF/SpeX observation, the simulated central-meridian line average is shown in red. It can be seen that we achieve a very good fit to the data for all three data sets.

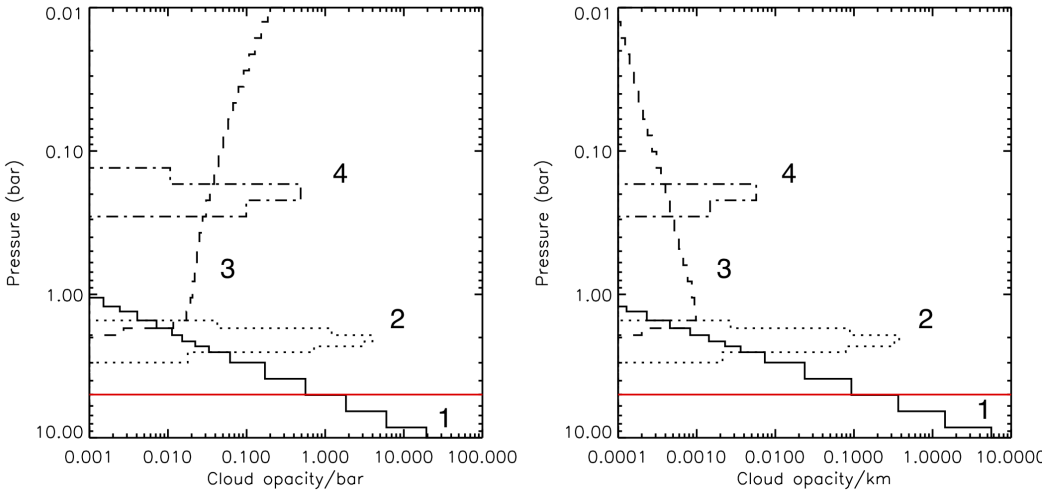


Figure 13. Fitted vertical aerosol structure for Neptune’s atmosphere from our example best-fit retrieval, presented in terms of opacity/bar (left) and opacity/km (right) at $0.8 \mu\text{m}$. The deep Aerosol-1 layer is shown as a solid line, the middle Aerosol-2 layer as a dotted line, the tropospheric/stratospheric extended haze (Aerosol-3) as a dashed line, and the detached methane ice haze near the tropopause as the dashed-dotted line. The red line marks the 5-bar level, which is roughly the level where our sensitivity runs out.

set of retrieved parameters is shown in Fig. 14 and the range and errors on our best fit solutions are listed in Table 2. It is worth noting, however, that the retrieved imaginary refractive index spectra of the main aerosol components, shown in Fig. 9, and listed in Table 4 are similar to those retrieved for Uranus, suggesting a similar composition. It is also worth noting that the opacity of the middle Aerosol-2 layer at ~ 2 bar is approximately half that determined for Uranus’s atmosphere, while the opacity of the deeper Aerosol-1 layer is also greatly reduced. The lower Aerosol-2 opacity means that the Aerosol-1 layer has a greater contribution to the modelled spectra and so we have greater constraint on the Aerosol-1 imaginary refractive index spectrum as can be seen. For the methane ice layer at 0.2 bar, this is retrieved to be composed of moderately large particles ($r = 2\text{--}3 \mu\text{m}$), which means they are most reflective at the longer wavelengths where the increased scattering at methane-absorbing wavelengths is seen. It also means that they are effectively conservatively forward-scattering at visible wavelengths, and thus they have very little effect here (as can be seen later in Fig. 18). Finally, since we discriminated against cloudy regions when we compiled our mean data sets, the opacity we retrieve for the Aerosol-4 layer will of course be significantly less than a true disc-average that includes such clouds.

One curious feature of these retrievals is the significantly larger deep methane abundance we retrieve for Neptune of $7\pm1\%$, versus $3\pm1\%$ for Uranus. An analysis of recent Neptune/MUSE observations (Irwin et al., 2021) found values varying from $5\pm1\%$ at the equator to $3\pm1\%$ at the south pole, which compared reasonably well with previous analyses of these HST/STIS observations and others (e.g., Karkoschka & Tomasko, 2009, 2011; Sromovsky et al., 2011, 2014) who found values of $\sim 4\%$ at equatorial latitudes and $\sim 2\%$ at polar latitudes for both planets. In this study, we have analysed disc-averaged spectra so we might have expected to retrieve a methane abundance of $\sim 3\text{--}4\%$ for both Uranus and Neptune, and given that we would see more of the polar regions in the Neptune disc-averages than in the Uranus observations we might expect to retrieve lower methane abundances for Neptune than we do for Uranus. In practice the deter-

mination of ‘deep’ methane abundance (i.e., immediately below the methane condensation level) is almost inextricably tied up with the assumed cloud/haze parameterisation scheme, and also the assumed vertical distribution of methane. Our simple haze model, which is designed to match the observations at **all** wavelengths simultaneously, leads to fits that do not match the 800–860 nm range as well as other models that are able concentrate on this region alone (e.g., Irwin et al., 2021) and achieve closer fits, lower methane abundances, and slightly different aerosol profiles. Also, in this work we have assumed the same simple ‘step’ model for the methane profile (constant mole fraction up to some fraction of the saturated vapour pressure curve set by the relative humidity) as Irwin et al. (2021), while other authors used a ‘descended’ methane profile (e.g., Sromovsky et al., 2019). Finally, although there is little cross-correlation seen in our ‘corner-plots’ (Figs. 8,14) it is possible that the methane abundance is correlated with some of the cloud parameters, perhaps Aerosol-1, and hence for Neptune the methane abundance is being slightly overestimated and the Aerosol-1 parameters under- or over-estimated. Hence, in practice the methane retrieval problem is extremely degenerate and while here we find a difference in the retrieved deep methane abundances for Uranus and Neptune, there is not sufficient evidence to claim that this is a robust result. Perhaps with a revised haze parameterisation scheme, or different Aerosol-1 particle assumptions, we may determine values that are closer to each other. We hope to return to this question in future work.

3.10 HST/WFC3 observations of dark spots in the atmospheres of Uranus and Neptune and their spectral characteristics.

The analysis of available reflectance spectra of Uranus and Neptune reveals very similar aerosol structures for both planets, with a deep Aerosol-1 layer based at $p > 5$ –7 bar detectable at visible wavelengths, a middle Aerosol-2 layer at 1–2 bar seen at other wavelengths, a vertically extended stratospheric haze (Aerosol-3), detectable mostly at visible wavelengths, and finally, for Neptune, the presence of condensation layer of moderately large methane ice particles near the tropopause. Such a model can then be used simulate the general appearance at all wavelengths of either planet with good accuracy. However, there is one aspect in which Uranus and Neptune seem to differ substantially and that is the presence of ‘dark spots’

The first dark spots observed in an Ice Giant atmosphere were the Great Dark Spot (GDS) and Dark Spot 2 (DS2), seen by Voyager 2 in Neptune’s atmosphere in 1989 (Smith et al., 1989; Sromovsky et al., 1993). The GDS was most visible at a wavelength of 0.48 μm , but was undetectable longward of 0.7 μm . Since the Voyager flyby several new dark spots have been seen in Neptune’s atmosphere from Hubble Space Telescope observations in 1994, 1996, 2015 and 2018 (Hammel et al., 1995; Sromovsky et al., 2001; Wong et al., 2018; Hsu et al., 2019). These have all had similar spectral characteristics to those noted for the GDS, namely that they are visible near 0.5 μm , but not visible longward of 0.7 μm . For Uranus, there has to date only been one dark spot detected, which was observed in 2006 (Hammel et al., 2009). Unlike the Neptune dark spots the Uranus dark spot seems to have been detectable to longer wavelengths.

The dark spots seem to be some sort of vortex structure and the colouration must be due to either a darkening of the aerosol particles, or a change in opacity of the aerosol layer, or perhaps a combination of both effects. Putting aside the Uranus dark spot observation for one moment, the darkening effect needs to be confined to a rather small and particular range of wavelengths. It could very well be caused by a spectrally-limited darkening of the aerosol particles, but we would then need to have quite a particular perturbation of the cloud/haze scattering properties and simultaneously confine that change somehow to be within a vortex. On the other hand, if dark spots are caused by cloud/haze opacity changes, we need to explain how its signature is so spectrally confined. We believe that the retrievals described in previous sections provide the answer. The deep Aerosol-1 layer based at $p > 5$ –7 bar is only visible at wavelengths less than $\sim 0.7 \mu\text{m}$ and if that

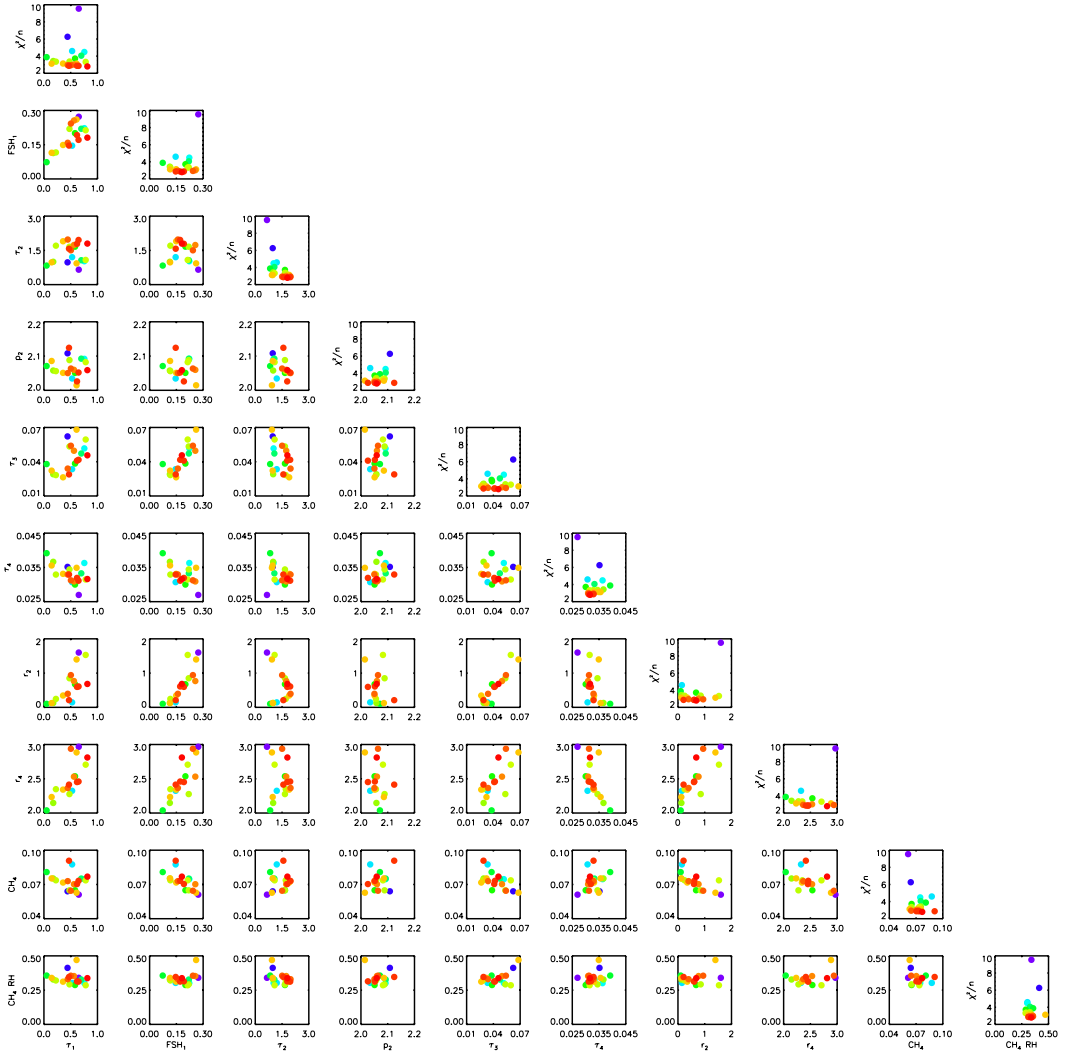


Figure 14. ‘Corner’ plot of 30 retrievals of the combined HST/STIS, IRTF/SpeX and Gemini/NIFS Neptune dataset with $\chi^2/n < 10$. The data points are colour-coded by the χ^2/n of the fit. Along the leading diagonal, instead of plotting the marginalised errors as would be usual for such plots, we plot χ^2/n as a function of fitted parameter. Although some parameters are better constrained than others, it can be seen that there is little cross-correlation between any of the fitted parameters.

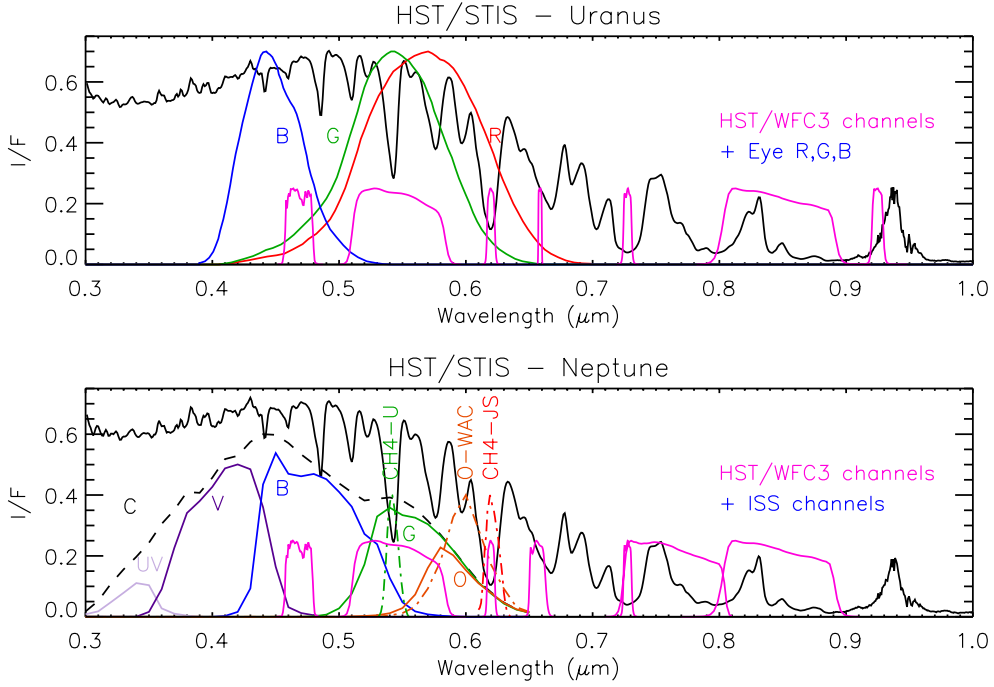


Figure 15. HST/STIS central-meridian-averaged I/F spectra of Uranus (top panel) and Neptune (bottom panel). Overplotted in the top panel for Uranus are the red, green, blue sensitivities of the human eye (Stockman & Sharpe, 2000; Stockman, 2019), together with the HST/WFC3 filters: F467M, F547M, FQ619N, F658N, FQ727N, F845M, and FQ924N (Dressel, 2021). Overplotted in the bottom panel for Neptune are the HST/WFC3 filters: F467M, F547M, FQ619N, F657N, FQ727N, F763N and F845M, together with the ‘clear’, ‘UV’, ‘violet’, ‘blue’, ‘green’ and ‘orange’ Voyager-2/ISS NAC sensitivities (Smith et al., 1977), and the ‘CH4-U’ (i.e., 547 nm), ‘CH4-JS’ (i.e., 619 nm) and ‘orange’ Voyager-2/ISS WAC sensitivities (dashed lines).

were to have lower opacity, or reduced reflectivity, then we might expect to see a dark spot at just those wavelengths.

To see if this phenomenon was apparent in our modelled Uranus observations we generated synthetic images of Uranus from our best-fitting cloud/haze model in the seven wavelength channels observed by HST/WFC3 with the OPAL program in 2014 (Simon et al., 2015). The location of the filters used (F467M, F547M, FQ619N, F658N, FQ727N, F845M, and FQ924N) are compared with the central-meridian line-averaged HST/STIS Uranus spectrum in Fig. 15 and in Fig. 16 we compare the observations with synthetic images. The middle and bottom rows of Fig. 16 show synthetic images at each filter wavelength, which were constructed using the following procedure:

1. In our baseline simulations we used our optimal fit to the reconstructed spectra at 0° and 61.45° to extract Minnaert parameters $I_0(\lambda)$ and $k(\lambda)$ and, using $I = I_0 \mu_0^k \mu^{k-1}$, constructed synthetic disc images of Uranus at each modelled HST/STIS wavelength, $I_{\text{reference}}(\lambda)$ for the HST/WFC3 observation zenith angles μ and μ_0 .
2. Then, from our fitted cloud/haze model, we calculated modelled spectra (at 0° and 61.45°) with either: A) the opacity of the Aerosol-1 layer based at $p > 5$ – 7 bar set to zero; or B) the imaginary refractive indices of the particles in this layer set to 0.001 at all wavelengths (which darkens the particles at short wavelengths).

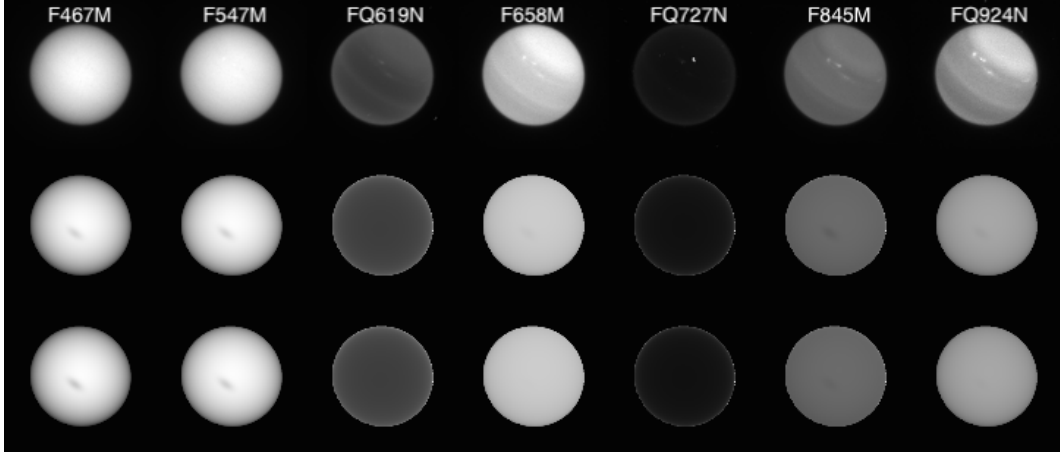


Figure 16. Observed and reconstructed HST/WFC3 images of Uranus. Top row shows HST/WFC3 observations made in 2014 during the OPAL program, centred at the wavelengths: 467, 547, 619, 658, 727, 845, and 924 nm. Middle row shows images reconstructed from our fits to the HST/STIS data, which also includes a hole in the deep Aerosol-1 layer ($p > 5 - 7$ bar) near the disc centre. Bottom row shows images reconstructed from our fits to the HST/STIS data, where the deep Aerosol-1 layer is darkened near the disc centre by setting $n_{imag} = 0.001$ at all wavelengths. It can be seen that for the darkening case the modelled dark spot is visible at 467 and 547 nm, but not at longer wavelengths, whereas for the clearing simulation the modelled spot is visible at 467 and 547 nm, but also faintly at 658, 845 and 924 nm. In addition, the modelled spot is darker at 467 nm when the Aerosol-1 layer is darkened rather than removed.

We then extracted modified $R_0(\lambda)$ and $k(\lambda)$ Minnaert parameters for both cases, which we used to generate two additional sets of synthetic Uranus images, $I_{modified}(\lambda)$.

- 834
- 835
- 836
- 837
- 838
- 839
- 840
- 841
- 842
- 843
- 844
3. We then constructed a weighting factor, f_w , to simulate a cloud/haze darkening/clearing near the disc centre, with latitude $\Phi_0 = 20^\circ\text{N}$ and central meridian longitude $\Lambda_0 = 0^\circ$, setting $f_w = \exp(((\Phi - \Phi_0)/\Delta\Phi)^2 + ((\Lambda - \Lambda_0)/\Delta\Lambda)^2)$, where Φ is the latitude on the disc, Λ is the longitude relative to the central meridian, and where $\Delta\Phi = 5^\circ$ and $\Delta\Lambda = 10^\circ$.
4. We then made weighted averages of our two sets of images at each HST/STIS wavelength: $I_{mean}(\lambda) = (1 - f_w)I_{reference}(\lambda) + f_wI_{modified}(\lambda)$.
5. Finally, the combined images were convolved with the HST/WFC3 filter functions to create the synthetic images.

845
846 From Fig. 16 it can be seen that aside from the latitudinal cloud/haze and methane
847 abundance variations visible in the observed images (which we did not attempt to sim-
848 ulate here) we capture reasonably well the observed limb-darkening/limb-brightening at
849 all wavelengths. Although the HST/WFC3 OPAL 2014 observations did not contain any
850 dark spots, if there were a hole in the deep Aerosol-1 layer in Uranus's atmosphere, or
851 a darkening, it can be seen in the middle and bottom rows of Fig. 16 that it would pro-
852 duce a dark spot at *precisely* the same wavelengths as seen by HST/WFC3, i.e., at 467
853 and 547 nm. However, while for the Aerosol-1-darkening case the spot is invisible at longer
854 wavelengths, for the clearing case it is still just visible at 658, 845 and 924 nm. In ad-
855 dition, the darkening simulation results in a spot that is darker at 467 nm than in the
856 clearing simulation, which is again more consistent with the observations.

857 Turning to Neptune, we generated synthetic images from our best-fitting model in
the seven wavelength channels observed by HST/WFC3 with the OPAL program in 2018

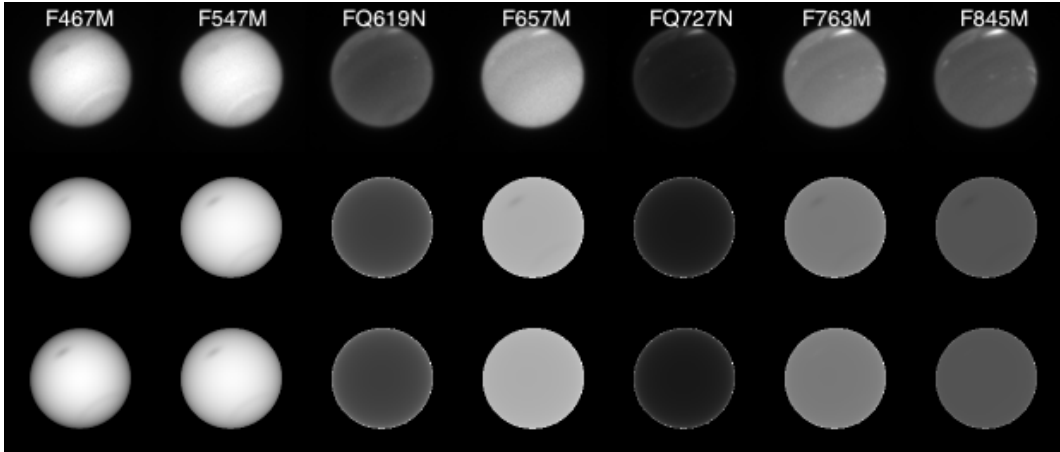


Figure 17. Observed and reconstructed HST/WFC3 images of Neptune. Top row shows HST/WFC3 observations made in 2018 during the OPAL program, centred at the wavelengths: 467, 547, 619, 657, 727, 763, and 845 nm. Middle row shows images reconstructed from our fits to the HST/STIS data, which also includes a hole in the deep Aerosol-1 layer ($p > 5 - 7$ bar) near the central meridian at 15°N, and a clearing at 60°S. Bottom row shows images reconstructed from our fits to the HST/STIS data, where the Aerosol-1 layer is darkened near the central meridian at 15°N and at all longitudes at 60°S by setting $n_{imag} = 0.001$ at all wavelengths. As for the Uranus case shown in Fig. 16, we can see that a dark spot is visible at 467 and 547 nm and that again, while for the Aerosol-1-darkening case the spot is invisible at longer wavelengths, for the clearing case it is still just visible at 657, 763 and 845 nm. Also, as for Uranus, the darkening simulation results in a spot that is darker at 467 nm than in the clearing simulation, which is more consistent with observations.

(Simon et al., 2019), which reported the detection of a new dark spot, NDS-2018. The channel filter functions used (F467M, F547M, FQ619N, F657M, FQ727N, F763M and F845M) are shown in Fig. 15 and the observed images can be seen in the top row of Fig. 17. In the middle and bottom rows, we present our simulations with a dark spot centred at $\Phi_0 = 15^\circ\text{N}$, $\Lambda_0 = 0^\circ$, and also with a clearing/darkening at latitude $\Phi_0 = 60^\circ\text{S}$. Here, we can again see that we predict the appearance of the clearing of the deep Aerosol-1 layer to be most clearly detectable at the two shortest wavelengths, very similar to the observed spot. However, for the clearing simulation, the modelled spot is still just visible at 657, 763 and 845 nm, which is contrary to the observations and also contrary to the darkening simulation, where the modelled spot is completely invisible at the longer wavelengths. In addition, the spot modelled with the darkening hypothesis is darker at 467 nm than the clearing case, which is again more consistent with the observed properties.

Considering Uranus and Neptune together it can be seen that although a clearing of the Aerosol-1 layer based at $p > 5-7$ bar produces *almost* the right response, it does not predict the spot to be darker at 467 nm than 547 nm, and the simulated spot can still just be seen at longer continuum wavelengths, contrary to the observations. In contrast, our simulated images where we darken the Aerosol-1 layer produces a feature that much more closely resembles the real NDS-2018 on Neptune. We find that removing the Aerosol-1 layer does not darken the spot sufficiently at short wavelengths since there is still significant Rayleigh scattering from the air itself at these depths. However, by darkening this aerosol layer, the contrast of the dark spot at short wavelengths is greatly increased. Add to that the disappearance of the feature at longer wavelengths by dark-

ening the Aerosol-1 particles, rather than removing them altogether, and on balance we conclude that darkening the particles provides a better match to the observations. Further evidence in support of this hypothesis comes from an analysis of earlier HST/WFC3 Neptune images (Karkoschka, 2011), where the author suggested that the dark belt at 30–60°S was best explained by a darkening of the haze at pressures > 3 bar. Karkoschka (2011) went on to speculate that since dark spots have very similar spectral characteristics to the 30–60°S belt, they might be explained by vertical motions bringing dark material from depth up to altitudes where it can be observed. Finally, we also see that our predicted Neptune dark spot is slightly darker than the equivalent spot modelled for Uranus, which can be explained by the fact that the opacity of the overlying ~2-bar Aerosol-2 layer on Neptune is lower than it is on Uranus. The higher opacity of the UV-absorbing Aerosol-2 layer on Uranus also explains why the UV reflectivity of Uranus is lower than Neptune.

Since the scattering cross-section of the approximately micron-sized Aerosol-2 particles is found to have a roughly white visible reflectivity spectrum, the higher opacity of the Aerosol-2 layer on Uranus also mostly explains why Uranus appears to have a paler blue colour to the human eye (to some more greenish) than Neptune, which we show in Fig. 18. In this figure we show the simulated colours of the background, masked regions of Uranus and Neptune reconstructed from the Minnaert limb-darkening approximations to the HST/STIS observations using Eq. 1. Here, as a representative case we assumed the solar and emission zenith angles varied across the disc of both Uranus and Neptune as observed for the Uranus 2014 HST/WFC3 observations shown in Fig. 16. In these simulations the modelled radiance spectra across the planet were convolved with the CIE-standard (Commission Internationale de l’Éclairage) red, green, and blue human cone spectral sensitivities of Stockman and Sharpe (2000); Stockman (2019) and are, as near as we can determine the ‘natural’ colours that the background atmospheres of these planets would have if we were to observe them from space. As can be seen Uranus appears paler and less blue than Neptune, although the colour differences are actually rather subtle. In Fig. 18 we can see that if we modelled the planets’ appearances for aerosol-free conditions and with no methane absorption then both planets would appear pearly-white since even though Rayleigh-scattering is more effective at blue wavelengths, we eventually reach depths at even red wavelengths where Rayleigh scattering becomes effective. It is only when we add absorption by the red-absorbing methane that the characteristic blue colour of these planets develop. Then as we add the scattering effects of Aerosol-1, Aerosol-3 and Aerosol-4 components the modelled appearances become paler, but it is not until we add in scattering from Aerosol-2 that the main colour difference manifests itself. Why the Aerosol-2 layer on Uranus is thicker than that of Neptune is not clear. Potentially, we suggest that perhaps the more dynamically overturning atmosphere of Neptune is more efficient at clearing this haze layer through methane condensation at its base, as discussed later. Also, we note that during the Voyager-2 encounters with these planets, Uranus was close to southern summer solstice when the south polar region was covered in a ‘hood’ of haze, which we presume to be Aerosol-2. Hence, the planet would likely have looked even paler than we have simulated here from HST/STIS observations in 2002 and 2003.

In summary we find that the aerosol structure that we have retrieved from the combined HST/STIS, IRTF/SpeX and Gemini/NIFS data for Uranus and Neptune are also consistent with HST/WFC3 observations and can also explain the observe colour difference between these planets. We also find that a darkening (or possibly opacity change) of the deepest aerosol layer (Aerosol-1) leads to a darkening that is consistent with the observed spectral characteristics of dark spots. Hence, we propose that the dark spots sometimes seen in Neptune’s atmosphere (and occasionally Uranus’s) are caused by a darkening of the deep Aerosol-1 layer. If dark spots in Uranus’s atmosphere really are visible over a wider wavelength range, as reported by Hammel et al. (2009), then this suggests that Uranus’s deep Aerosol-1 layer, presumably containing a significant frac-

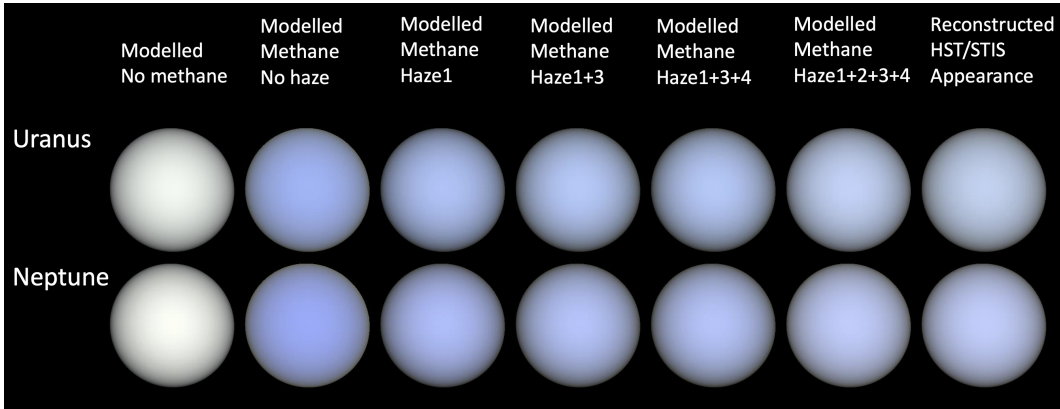


Figure 18. Modelled colours of Uranus and Neptune. The right-hand column shows the simulated ‘observed’ appearance of Uranus and Neptune, reconstructed using the fitted Minnaert limb-darkening coefficients extracted from the HST/STIS data and assuming the observing geometry of the 2014 Uranus HST/WFC3 observations (Fig. 16) for both planets. The spectra across the discs were convolved with the Commission Internationale de l’Éclairage (CIE)-standard red, green, and blue human cone spectral sensitivities (Stockman & Sharpe, 2000; Stockman, 2019) to yield these apparent colours: it can be seen that Uranus is predicted to have a paler, more greenish colour than Neptune. The preceding columns show how our modelled appearance of these planets changes as we add different components to our radiative transfer model. Column 1 shows the modelled appearance of both planets if we remove all the haze and neglect methane absorption: in this case both planets would appear pearly-white since even though Rayleigh-scattering is more effective at blue wavelengths, we will eventually reach depths at even red wavelengths where Rayleigh scattering becomes effective. The effect of adding in absorption from the best-case retrieved methane profile for both planets is shown in Column 2, and underlines the fact that it is the presence of atmospheric methane that leads to the underlying blue colour of these planets. However, the difference in observed colour between Uranus and Neptune cannot be explained by just by the fact that we retrieve more methane in Neptune’s atmosphere than Uranus’s. Column 3 shows the effect of adding in the retrieved profiles for Aerosol-1, while Column 4 shows the effect of further adding Aerosol-3, which can be seen to have little effect. In Column 5 we also add in Aerosol-4. This is set to zero opacity for the Uranus retrievals and so there is no change, while the retrieved opacity for Neptune is very small, which when combined with the forward-scattering nature of the large ($2\text{--}3 \mu\text{m}$ -sized) particles leads to negligible difference for Neptune also. Finally, in Column 6 we add in the opacity of Aerosol-2 to all the other components, which can be seen to lead to the greatest difference between the predicted colours of Uranus and Neptune, and also leads to final colours that are indistinguishable from those reconstructed from the initial HST/STIS limb-darkening coefficients in Column 7 (‘Reconstructed HST/STIS Appearance’). (N.B., the overall brightness in each column as been separately scaled to make each column uniformly bright.)

935 tion of H₂S ice, is brighter over a wider range of wavelengths, since retrieval tests con-
 936 ducted with a conservatively-scattering lower cloud/haze produced a detectable dark spot
 937 signature at all the HST/WFC3 wavelengths when the opacity of this layer was reduced,
 938 except in the strong methane bands at 619 nm and 727 nm.

939 3.11 Voyager-2/ISS observations of dark spots in Neptune's atmosphere.

940 Having found a good correspondence with the spectral properties of dark spots seen
 941 in Neptune's atmosphere with HST/WFC3 by darkening the Aerosol-1 layer, we won-
 942 dered whether we might also be able to find a good correspondence with the original Voy-
 943 ager 2 ISS observations, which first detected such phenomena (Smith et al., 1989). Dur-
 944 ing Voyager-2's approach to the Neptune system in August 1989, the Imaging Science
 945 Subsystem (ISS) took a particular sequence of observations, "Full color set for atmospheric
 946 dynamics", consisting of 319 full-disc observations from 16th to 18th August in each of
 947 the main filters of its Narrow-Angle Camera: UV, Violet, Blue, Green, Orange and also
 948 with no spectral filter (Clear). Observations were also made in three filters of its Wide-
 949 Angle Camera: 'CH4-U' (541 nm), 'CH4-JS' (619 nm) and another Orange filter. The
 950 transmission functions of all these filters are shown in Fig. 15. In these images the Great
 951 Dark Spot (GDS) and also Dark Spot 2 (DS2) were observed at several phase angles.
 952 We examined the limb-darkening properties of the GDS and also the 50°S dark belt in
 953 these observations to see if they supported or contradicted our hypothesis that dark re-
 954 gions are caused by a clearing, or darkening, of the deep H₂S/haze Aerosol-1 layer. Rep-
 955 resentative Voyager-2 observations from this set are shown in Fig. 19. It can be seen that
 956 the GDS is particularly prominent in the Blue filter channel, but becomes less so as we
 957 move to both shorter and longer wavelengths. The bright companion clouds become more
 958 prominent at longer wavelengths, as the Rayleigh scattering becomes less significant, in-
 959 dicating these features to lie at higher altitudes, presumably in the upper troposphere.
 960 The contrast between the dark spots and the surrounding regions looks similar to that
 961 between the darker belt centred at 50°S and surrounding latitudes and we assume, like
 962 Karkoschka (2011), that both are formed a similar way. Looking at the 50°S dark belt
 963 it can be seen that this region is most visible near the central meridian and gets less clear
 964 towards the limbs.

965 To interpret these observations more quantitatively, we performed a limb-darkening
 966 analysis of the Voyager 2 ISS images, which we summarise in Fig. 20. In this figure we
 967 have analysed the observations for each of the six NAC filters studied, first of all concen-
 968 trating on images where the GDS and DS2 were not visible and analysing the limb-darkening
 969 of the background atmosphere in two latitude bands: 15 – 25°S (centred on the GDS)
 970 and 45 – 55°S (centred on the dark belt). Assuming the Minnaert approximation to hold,
 971 Eq. 1 can be re-expressed as

$$972 \log(\mu R) = \log(R_0) + k \log(\mu \mu_0), \quad (3)$$

973 where R is the measured reflectance (i.e., I/F), μ and μ_0 are cosines of the viewing and
 974 solar zenith angles respectively, and R_0 and k are the fitted Minnaert parameters. Hence,
 975 plotting μR against $\mu \mu_0$ on a log-log plot should yield a straight line if the Minnaert ap-
 976 proximation is good and in Fig. 20 we have plotted such curves for the two latitude belts
 977 for all filters. We find that the observed limb darkening is well described by the Minnaert
 978 model and also that the 45 – 55°S belt has a lower $(I/F)_0$ and is noticeably less limb-
 979 darkened than the 15 – 25°S belt, having a significantly shallower slope (i.e., lower k ,
 980 but still greater than 0.5, which is the boundary between limb-darkening and limb-brightening).

981 We then analysed individual observations in the data set containing the GDS at
 982 different zenith angles, selecting pixels within the GDS and over-plotting their reflectance
 983 in the same way in Fig. 20. There was good sampling for the NAC images, but far fewer
 984 WAC images, which were also less spatially resolved making the limb-darkening less clear.
 985 In addition, the CH4-JS channel seems poorly flat-fielded and photometrically corrected.

Accepted Article

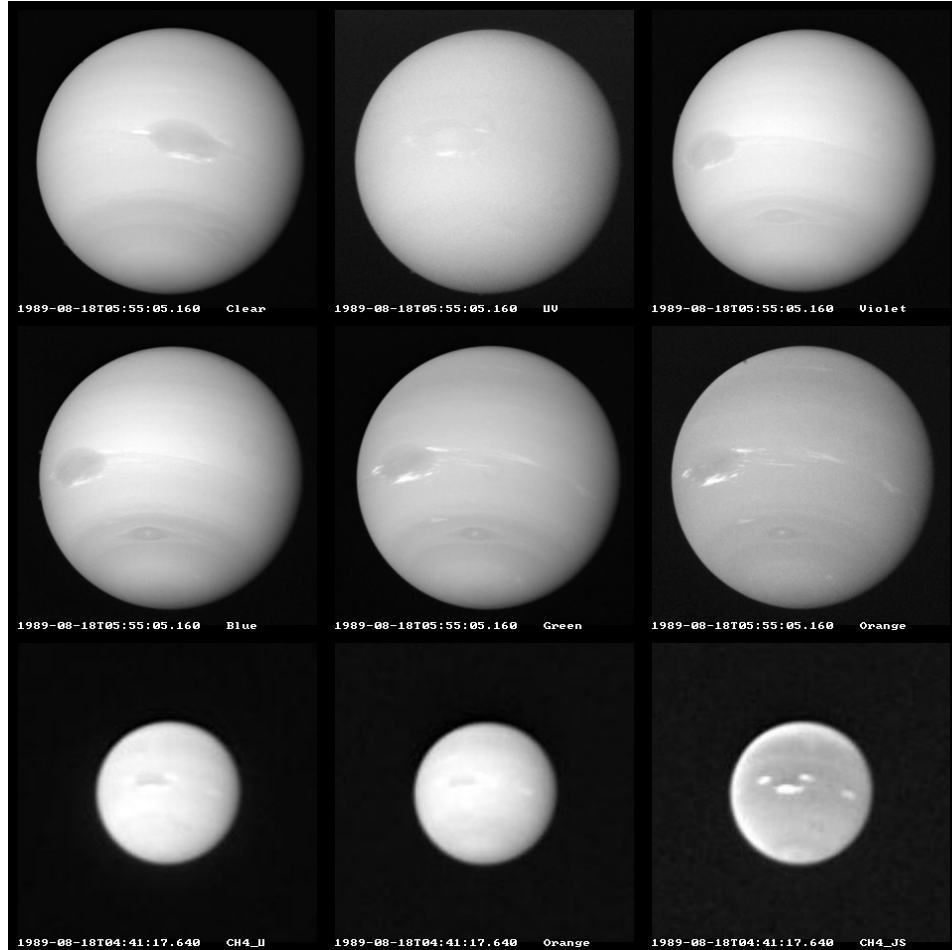


Figure 19. Representative Voyager-2 ISS images of Neptune, observed in August 1989 in the Clear, UV, Violet, Blue, Green and Orange filters, respectively of the Narrow Angle Camera (NAC) and also CH4-U (541 nm), Orange and CH4-JS (619 nm) from the Wide Angle Camera (WAC). For the NAC images, the Great Dark Spot (GDS) and Dark Spot 2 (DS2) are clearly visible, except in the UV channel. Also visible (except again in the UV) is the generally darker belt at 45–55°S. The WAC images are of poorer quality, but cover complementary wavelengths and the GDS and dark belt are still visible in the CH4-U and orange filters. For the CH4-JS filter, centred at 619 nm, the dark belt is less clear, and the white clouds around the GDS are relatively much brighter indicating that these are at a higher altitude than the main 1–2-bar Aerosol-2 layer.

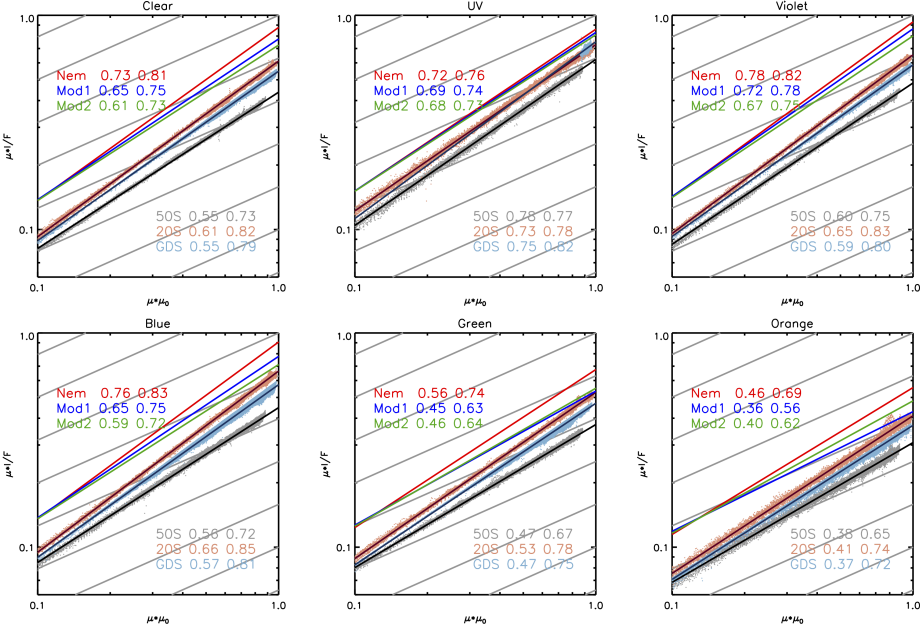


Figure 20. Results of Minnaert analysis of the Voyager-2 ISS NAC observations of Neptune. In each panel (filter), we have first plotted on a log-log plot the observed reflectances multiplied by μ (the cosine of zenith angle) against $\mu\mu_0$ for the 15–25°S and 45–55°S bands, together with the fitted Minnaert lines and derived $(I/F)_0$ and k values, showing the clear linear dependence expected from the Minnaert model, and less pronounced limb-darkening at 45–55°S (smaller values of k) compared with 15–25°S. Note the 45–55°S reflectivities have been scaled by a factor of 0.8 for clarity. Also plotted are the observed limb-darkening dependencies of pixels within the GDS (and associated Minnaert fits), which have a smaller limb-darkening coefficient than the background at 20°S, but less so than at 45–55°S. Finally, on each plot is shown the simulated limb-darkening behaviour of our best-fitting Neptune NEMESIS model (coloured lines, multiplied by 1.2 for clarity) including the deep > 5–7-bar Aerosol-1 layer ('Nem'), removing the Aerosol-1 layer ('Mod1'), or darkening it ('Mod2'), which show similar differences indicating that dark regions are well fitted by our model with lower > 5–7-bar aerosol layer reflectivity. The parallel grey lines on this plot are for reference and mark simulated $k = 0.5$ lines, for which the disc has no limb-darkening or limb-brightening.

Hence, the WAC images were discounted in the limb-darkening analysis. It can be seen in Fig. 20 that pixels within the GDS have a similar $(I/F)_0$ to those in the 50°S belt and the limb-darkening is again less than the background 20°S region, but less so than for 50°S. However, the fact that the GDS and 50°S belt have both lower $(I/F)_0$ and lower k than the background at 20°S suggests these dark features really do have a common origin. To determine if this common origin is due to lower reflectance from the deep Aerosol-1 layer we have also plotted in Fig. 20 the simulated limb-darkening from our best-fitting cloud/haze retrieval to the combined STIS/SpeX/NIFS Neptune data set, including the contribution from this layer, or modifying it by clearing or darkening. It can clearly be seen that reducing the contribution from the Aerosol-1 layer lowers both $(I/F)_0$ and the limb-darkening parameter k , just as is seen for the Voyager-2 dark regions, suggesting that this may indeed be the cause of the darkening. On balance, the difference in limb-darkening is again slightly better simulated by darkening the Aerosol-1 layer, rather than removing it.

In summary, the Voyager-2 ISS observations of Neptune support our suggestion that dark regions are caused by a darkening (or possibly clearing) of the deep Aerosol-1 H₂S/ photochemical haze layer. It has sometimes been suggested that the dark spots might be caused by a darkening of the overlying haze. We looked to see if darkening the 1–2-bar Aerosol-2 layer could explain the observations, but found that this is not supported by the limb-darkening evidence. Such a scenario would lead to stronger limb darkening than observed, since as the spot moved towards the limb we would be looking through more and more of this darker haze. Instead, we believe we are looking at the darker deep Aerosol-1 layer through the fairly uniform 1–2 bar Aerosol-2 layer, which is reasonably scattering at these wavelengths. Hence, as spots move towards the limb we see more reflectance from the Aerosol-2 layer at 1–2 bar and less from the deep Aerosol-1 layer, leading to the reduced limb darkening observed.

4 Discussion

4.1 Vertical Aerosol Structure

Excepting the additional upper tropospheric methane aerosol layer on Neptune, we find very similar vertical aerosol structures for both Uranus and Neptune composed of:

1. Aerosol-1: A deep layer based at $p > 5\text{--}7$ bar of moderately scattering particles (assumed, as previously discussed, to be sub-micron-sized) that we assume to be coincident with the main H₂S cloud/haze condensation layer, perhaps composed of a mixture of photochemically-produced haze particles and H₂S ice;
2. Aerosol-2: A vertically-thin haze near the methane condensation level at 1–2 bar, composed of approximately micron-sized particles that are scattering at visible wavelengths, but more absorbing at UV and longer wavelengths; and
3. Aerosol-3: A vertically-extended haze of sub-micron-sized particles with a fractional scale height of 2 and moderately similar refractive index spectra to the 1–2 bar Aerosol-2 layer.

The similarity of the structure (both vertical and spectral scattering) of the two planets should not be surprising given their similar tropospheric gaseous composition and temperatures, but how can we account for the fact that we apparently have a layer of photochemically-produced haze at the methane condensation level and not methane clouds? We hypothesise that to account for this structure we need to consider the vertical stability of Uranus's and Neptune's atmospheres.

In Appendix A we outline the theory behind buoyancy and static stability in planetary atmospheres. At pressures where the temperature profile falls more slowly with height than the lapse rate, the air is stable to vertical perturbations and will try, if moved vertically, to return to its original level, giving rise to gravity waves with a frequency defined by the Brünt-Väisälä frequency, N . For most atmospheres, this frequency just depends on the vertical gradient of the *potential temperature* $\theta = T(\frac{p_0}{p})^\gamma$, where $\gamma = R/C_p$, T and p are the local temperature and pressure, p_0 is a reference pressure level, R is the gas constant and C_p is the molar heat capacity at constant pressure. The Brünt-Väisälä frequency can be shown in Appendix A to be:

$$N^2(z) = g \frac{d}{dz} \left(\ln \theta_0(z) \right) \quad (4)$$

where $\theta_0(z)$ is the potential temperature of the background air at altitude z .

The latent heat released by the condensation of clouds lowers the rate at which temperature falls with height, making the air more stable for both planets, and this can be

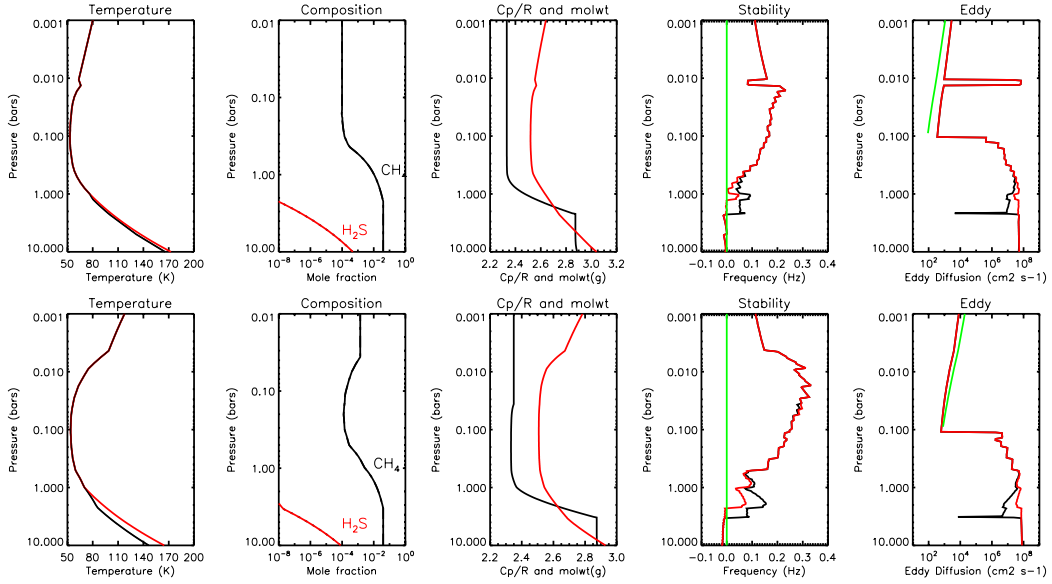


Figure 21. Ice Giant stability plots, with Uranus on top row and Neptune on bottom. We have assumed $\text{He}/\text{H}_2 = 1.06 \times$ solar and $\text{CH}_4/\text{H}_2 = 64 \times$ solar for both planets (assuming protosolar composition of (Asplund et al., 2009)), leading to a ‘deep’ (i.e., at 10 bar) CH_4 mole fraction of 4%. For Uranus we have assumed $\text{H}_2\text{S}/\text{H}_2 = 37 \times$ solar and $\text{NH}_3/\text{H}_2 = 1.4 \times$ solar (Molter et al., 2021), and for Neptune we have assumed $\text{H}_2\text{S}/\text{H}_2 = 54 \times$ solar and $\text{NH}_3/\text{H}_2 = 3.9 \times$ solar (Tollefson et al., 2021), leading to mole fractions for H_2S at 20 – 40 bar of 6.4×10^{-4} and 7.2×10^{-4} , respectively. For each planet/row there are five plots: 1) temperature profiles - red line assumes a dry adiabatic lapse rate (DALR) at depth, while the black line assumes a saturated adiabatic lapse rate (SALR) and so includes latent heat released by condensation; 2) composition profiles showing the assumed methane and H_2S mole fraction profiles; 3) profiles of the mean molecular weight (black) and the molar heat capacity at constant pressure (red), C_p ; 4) stability of atmosphere, represented in terms of the Brünt-Väisälä frequency, calculated from the temperature profile alone (red) and then also including the molecular weight gradient (black); and 5) Eddy-diffusion coefficient estimates calculated, including (black) or excluding (red) molecular weight changes, from the model of Ackerman and Marley (2001), and compared with upper tropospheric determinations of K_{zz} by Fouchet et al. (2003) (green). In the Brünt-Väisälä frequency panels, the green line indicates the neutral static stability line.

seen in our calculations of the Brünt-Väisälä frequency in Fig. 21, with a local region of higher Brünt-Väisälä frequency seen just above the methane condensation level. However, while Eq. 4 is perfectly acceptable for most atmospheres, where the molecular weight does not change greatly with height, this is not the case for Uranus and Neptune near the methane condensation layer. Assuming a deep mole fraction of 4% for methane, the mean molecular weight reduces from ~ 2.9 to ~ 2.3 g/mol for both planets across the methane condensation region, a decrease of $\sim 20\%$. This decrease in molecular weight at the condensation level increases the static stability even further since the lighter air is naturally more buoyant than the heavier air below. We show in Appendix A that a more appropriate equation for the Brünt-Väisälä frequency for atmospheres where the molecular weight also changes significantly with height is:

$$N^2(z) = g \frac{d}{dz} \left(\ln \left(\frac{\theta_0(z)}{M_0(z)} \right) \right) \quad (5)$$

where $M_0(z)$ is the molecular weight of the background air at altitude z . It can be seen in Fig. 21 that including this term greatly increases the static stability of the atmosphere at the methane condensation level.

We hypothesise that this localised vertical region of static stability somehow leads to an enhanced opacity of larger haze particles that, at the lower boundary, act as seed particles for methane condensation. Given the large mole fraction of methane, and ready supply of cloud condensation nuclei (CCN), methane cloud formation will likely be extremely rapid and Carlson et al. (1988) estimate that methane particles at 1–2 bar in Ice Giant atmospheres may grow to a size of ~ 5 mm in as little as ~ 100 s. Hence, these large methane ice particles would almost immediately precipitate, or ‘snow’, out, which would explain why pure methane ice clouds are almost never seen at these levels. The precipitating methane ice particles will drop to deeper levels before sublimating and releasing their payload of photochemical haze particles, which in turn may serve as CCNs for H₂S ice in the 4–10-bar region. The process is analogous to the “smust” concept that Hunten (2008) proposed to explain a vertical gap in the heavy hydrocarbon gas abundances of Jupiter. The difference is that in the case of Uranus and Neptune, methane ice transports haze particulates, while in the case of Jupiter, Hunten (2008) proposed that haze particulates transported volatile hydrocarbon species. Since the mole fraction of H₂S is expected to be very much lower ($\sim 10^{-4}$) than for methane, particle growth at 4–10-bar will not be so rapid (e.g., Carlson et al., 1988) and hence a stable layer of H₂S cloud could form. In addition, there are no vertical stability barriers since the latent heat release and change in mean molecular weight at this pressure level are very small, as can be seen in Fig. 21.

Returning to the Aerosol-2 layer, methane condensation acts to create a clearing beneath it in two ways. Condensation onto haze particles at the base of the layer causes them to snow out directly, and the stable layer produced by latent heating and reduced molecular weight reduces K_{zz} and slows the rate at which haze particles in the Aerosol-2 layer mix into the deeper levels. Within the layer, the mechanism for the local enhancement of haze opacity is currently unknown and understanding of this newly-discovered feature will require a future microphysical modelling study. Toward the top of the compact Aerosol-2 layer, the decrease in haze density with altitude (in the presence of eddy mixing) implies some sort of particle density source at the base of the layer, rather than above it, because eddy mixing alone can only modify the slope of a gradient from the source region to the sink region, not reverse it. The action of methane, near saturation, could be significant. Considering the likely hydrocarbon composition of haze particles, it is possible that methane condensation, even at subsaturated vapour pressures, could influence the surface chemistry of haze particles (in analogy to hydrophilic aerosols significant in terrestrial hazes). It is also possible that while methane condensation at the base is rapid, leading to the formation of large particles, there will be also be some com-

ponent of smaller particles in the size distribution. The fractional abundance of these smaller haze/ice particles is likely to get larger as we move up to lower pressures and lower temperatures in the Aerosol-2 layer, where the saturated vapour pressure of methane will be much lower. Hence, what we may be seeing in the Aerosol-2 layer is a mixture of photochemical haze and methane ice. Microphysics in the unique environment of the Aerosol-2 layer may thus be complex, and it is clear that the haze particles cannot be considered static tracers of mixing.

While this scenario provides an attractive model for the background aerosol structure of both planets, the atmosphere of Neptune is more energetic and contains frequent cloud features that appear to be methane condensation. For the most part these appear to form in the upwelling regions at 20–40°N and 20–40°S and at pressures of 0.6 to 0.1 bar (e.g., Irwin et al., 2016; Molter et al., 2019). However, Irwin et al. (2011a) report the appearance of several clouds at 60–70°S in 2009 that are deep in the atmosphere at 1–2 bar and may be rare examples of methane clouds forming near the methane condensation level itself.

As to the nature of the photochemical haze, there are several candidates. Khare et al. (1993) report the spectra of ‘tholins’ generated by irradiating H₂O/C₂H₆ mixtures, which have minimal absorption at 0.8 μm and increasing absorption as we move to UV, or longer wavelengths. While the spectrum of these ‘tholins’ is not identical to those derived here it is qualitatively similar. Another candidate is acetylene soot (Dalzell & Sarofim, 1969), which also has increasing absorption at long wavelengths. Indeed, such hazes share some characteristics with the phenomenon of ‘blue hazes’ commonly observed in the Smoky Mountains of eastern Tennessee and the Blue Ridge Mountains of Virginia (Ferman et al., 1981). Examining the scattering cross-sections of the retrieved aerosol particles, we find that the small particles assumed to be present in the deep Aerosol-1 component, and found to be necessary in the extended Aerosol-3 component above ∼1.5 bar, would appear to be blue at visible wavelengths. However, the larger particles in the 1–2 bar Aerosol-2 layer would appear white in the visible.

The stability of the 1–2-bar region in the Ice Giant atmospheres has also been concluded by Guillot (1995) and Leconte et al. (2017). Intriguingly, Teanby et al. (2020) noted that a stable layer at this pressure level has important implications for the internal oxygen enrichment of Neptune (Teanby et al., 2020; Cavalié et al., 2017). Limited mixing at 1–2 bar could permit externally-sourced CO entering Neptune’s atmosphere from comets to be trapped in the upper troposphere, which removes the need to have extreme internal oxygen enrichment in order to explain the wide wings in Neptune’s sub-mm CO lines. Previous work had suggested CO to be present throughout the troposphere, which requires an extremely high internal oxygen enrichment compared with the solar composition by a factor of at least a few hundred (Lellouch et al., 2005; Luszcz-Cook & de Pater, 2013; Cavalié et al., 2017; Moses et al., 2020) in order to act as a deep source for tropospheric CO. If externally sourced CO can be kept in the upper troposphere by limited mixing this opens up the possibility of a more rock-rich Uranus and Neptune (Teanby et al., 2020), in keeping with more modest oxygen enrichments of ∼50 inferred from the observed D/H ratio (Feuchtgruber et al., 1997).

Finally, in Appendix D we outline a review of methods for calculating the eddy diffusion coefficient, K_{zz} , in planetary atmospheres. With some modification of model parameters suggested by Ackerman and Marley (2001) we found we could derive a K_{zz} profile that was consistent with upper stratospheric determinations of K_{zz} by Fouchet et al. (2003), as can be seen in Fig. 21. With these parameters we find a local minimum of K_{zz} at the methane condensation level, but also a smaller minimum near the tropopause; this second K_{zz} minimum may help to explain the detached methane ice layer (Aerosol-4) seen near the tropopause of Neptune, where the atmosphere may be dynamically vigorous enough to mix methane up to such levels.

1147 4.2 Nature of dark regions in the atmospheres of the Ice Giants

1148 In this paper we have shown that dark regions seen occasionally in Neptune's at-
 1149 mosphere, and rarely in Uranus's atmosphere, can be explained by a darkening, or opac-
 1150 ity change of the deep Aerosol-1 layer, which we have suggested may be composed of a
 1151 mixture of H₂S ice and photochemically-produced haze. Such a condensation level is con-
 1152 sistent with the estimate from ground-based microwave studies that the deep abundance
 1153 of H₂S in Uranus's and Neptune's atmospheres are $53.8^{+18.9}_{-13.4} \times$ solar (Tollefson et al.,
 1154 2021) and $37^{+13}_{-6} \times$ solar (Molter et al., 2021), respectively. We believe the reason that
 1155 such regions are more commonly reported on Neptune than Uranus is that the overlying
 1156 1–2-bar Aerosol-2 layer on Neptune has lower opacity, making the deep Aerosol-1
 1157 layer more visible.

1158 Interpreting the results of our radiative transfer analysis with respect to the struc-
 1159 ture of dark vortices is complicated, especially if the dark spots are to be explained by
 1160 a darkening of particles in the deep haze layer. Particle colour (resulting from changes
 1161 to n_{imag}) cannot be unambiguously attributed to composition and/or heterogeneous mi-
 1162 crophysical structure, and thus linking these quantities to vortex dynamics and struc-
 1163 ture would be speculative given the limited information currently available. Even for Jupiter,
 1164 where more detailed information is available, links between vortex structure and aerosol
 1165 properties remain tentative (e.g., Wong et al., 2011). It is possible that dark spots are
 1166 generated by secondary-circulation uplift within vortices dredging up and concentrat-
 1167 ing a ‘chromophore’ material from warmer depths below, which is dark at visible wave-
 1168 lengths. However, it is not clear what this material might be, and photolysis, which might
 1169 be thought necessary to generate dark particles, is unlikely to be significant at pressures
 1170 of $\sim 5\text{--}7$ bar since the UV flux will be very low. Rather than interpreting such features
 1171 as being caused by the addition of a new ‘chromophore’, an alternative explanation might
 1172 be that such regions are anomalously warm at the H₂S condensation level and so H₂S
 1173 ice sublimates into the vapour state, revealing the darker CCN photochemical haze core,
 1174 similar to the mantling process proposed in (West et al., 1986) to explain belt-zone color
 1175 differences in Jupiter’s atmosphere. Such a scenario may be consistent with cooling above
 1176 the anticyclone mid-plane and warming below, as seen in numerical simulations (Stratman
 1177 et al., 2001; Hadland et al., 2020; Lemasquerier et al., 2020) and theoretical models (Marcus
 1178 et al., 2013). However, more observations are needed to fully constrain why the parti-
 1179 cles in the Aerosol-1 layer appear to be darker in the centre of dark spots and at dark
 1180 latitudes.

1181 Our results place interesting constraints on the vertical structure of dark spots. Geostrophic
 1182 anticyclones in stratified fluids—whether salt lenses in the Earth’s oceans or the Great
 1183 Red Spot in Jupiter’s atmosphere—are characterized by high density anomalies in their
 1184 upper regions, and low density anomalies in their lower regions (for example, dark con-
 1185 tours in Fig. 2 of Barceló-Llull et al. (2017), Fig. 3 of Marcus et al. (2013), Fig. S8 of
 1186 Lemasquerier et al. (2020)). Thus, how giant planet atmospheric vortices affect the ob-
 1187 servable aerosol structure depends on the location of aerosol layers with respect to the
 1188 vortex mid-plane. Anticyclones are also more efficiently mixed, compared to the strat-
 1189 ified background atmosphere (e.g., Hassanzadeh et al., 2012).

1190 Figure 22 compares differences in model Jupiter and Neptune vortex structures that
 1191 might be consistent with our deep aerosol results. In Jupiter’s case, observable aerosol
 1192 layers (the NH₃ ice cloud layer plus the tropospheric haze above it) intersect the upper
 1193 part of the vortex, where the high density anomaly is associated with cooler tempera-
 1194 tures (e.g., Cheng et al., 2008). The cooler temperatures enhance haze (e.g., N₂H₄) con-
 1195 densation (West et al., 1986), and efficient mixing delivers cloud and haze precursors to
 1196 high altitudes, producing the increased aerosols that are seen within the upper portion
 1197 of Jovian anticyclones (Banfield et al., 1998).

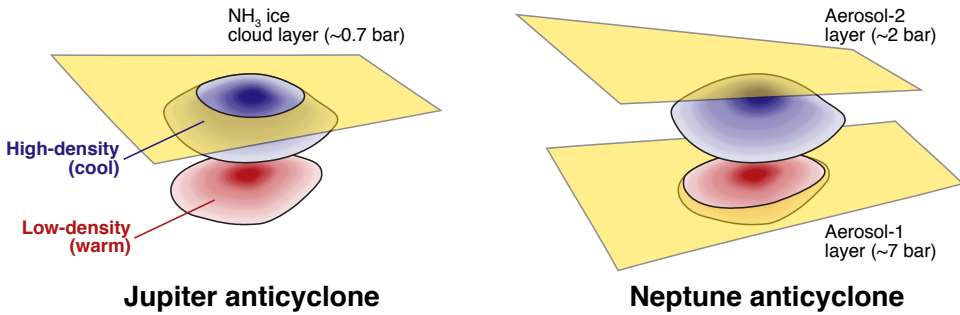


Figure 22. Possible explanations for vertical structure of dark spots in Uranus and Neptune's atmospheres, compared with vortex model for Jupiter's atmosphere. Cloud structure may be affected differently, depending on whether cloud layers intersect with the high-density (cool) or low-density (warm) anomalies associated with anticyclonic vortices. Left hand panel shows a model of vortices in Jupiter's atmosphere, where the upper cooler part of the vortex intersects with the NH₃ condensation layer, leading to enhanced ice formation there, and enhanced haze formation above it (extending close to the tropopause). In contrast, the right hand panel shows a similar model for Neptune's atmosphere, where the lower warm region overlaps with the H₂S condensation level, causing a darkening, or clearing, of the Aerosol-1 layer. To explain the lack of any changes in the Aerosol-2 layer at the location of dark spots, the high-density (cool) anomaly may need to reside deeper than the Aerosol-2 layer. However, a deep vortex top is challenging to reconcile with observations of orographic companion clouds near dark spots. Alternatively, the mid-plane may need to coincide with the Aerosol-2 layer.

Depleted, or darkened, aerosols in Neptune's dark spots, as possibly suggested by our analysis, may indicate that the vortex midplane is located at higher altitudes than the deep Aerosol-1 layer. Higher temperatures in the low-density anomaly would inhibit H₂S condensation. Depending on the vertical distribution of the dark haze CCNs populating the deep layer, mixing within the anticyclone may also play a role by altering the concentration of CCNs at the H₂S condensation layer. This scenario may also constrain the top of the vortex in this model. Efficient mixing within the anticyclone would disrupt the middle Aerosol-2 layer near 1–2 bar, which is not observed. We have demonstrated that we can model the dark spot appearance at all HST/WFC3 wavelengths (Fig. 10) without any changes to the middle Aerosol-2 layer, which would mean that the high-density anomaly of the dark vortex may reside entirely below this level. Models where both the Aerosol-1 and Aerosol-2 layers were depleted rendered vortices visible at longer HST/WFC3 wavelengths, in contradiction with the observations. If vortices are indeed bounded by approximately the 2-bar and 10-bar surfaces, their thickness is less than two atmospheric pressure scale heights. This thickness is much smaller than that for Jupiter, where remote sensing of the visible clouds constrains vortex tops to about the 0.5-bar level (e.g., Banfield et al., 1998; West et al., 2004; Cheng et al., 2008) and vortex bases to levels near the 10-bar level, or perhaps as deep as 800 bar in the special case of the Great Red Spot (Parisi et al., 2021; Bolton et al., 2021). Thermal infrared observations, however, (e.g., Fletcher et al., 2010) find that the thermal effects of vortices reach even higher to the tropopause. Jovian vortices thus span ranges of 3–7 scale heights. The potential difference in vortex thicknesses between Jupiter and Neptune may perhaps be related to the deep stratification of these outer planet atmospheres, which is still not known to high precision. Direct measurements at relevant pressure levels are only available for a single time and place: the Galileo Probe entry site at Jupiter (Seiff et al., 1998; Magalhães et al., 2002). Given the dependence of vortex vertical/horizontal aspect ratio on

the difference between internal and environmental stratification (Hassanzadeh et al., 2012), and the roughly comparable horizontal dimensions of vortices on Jupiter and Neptune (Li et al., 2004; Wong et al., 2018), the thicker vertical dimensions of Jupiter's vortices may indicate that the environmental stratification is weaker on Jupiter compared to Neptune. However, this tightly constrained thickness scenario runs counter to the observation that such dark spot disturbances are often accompanied by what appear to be orographic clouds near the tropopause, e.g., the 'scooter' cloud that accompanied Voyager-2's GDS. Hence, it would seem that the effect of the vortices must actually extend much higher. A possible scenario that might be consistent with all the evidence may be that the mid-plane of the vortex coincides with the statically stable 1–2-bar Aerosol-2 layer, i.e., the methane condensation level, which could leave this layer unaffected, but would affect both upper and lower clouds.

4.3 Dependence of solutions on methane absorption spectra

The main retrievals presented here have been conducted using k-tables generated from the methane band model coefficients of Karkoschka and Tomasko (2010). We used these coefficients as they cover the entire spectral range of our observations leading, we hope, to self-consistent results. The line data sets that are available, e.g., WKLMC@80K (Campargue et al., 2013) have been shown to provide better fits to the H-band observations (e.g., Irwin, de Bergh, et al., 2012), but are limited in their wavelength coverage and so cannot cover the entire 0.3 – 2.5 μm region. Later databases, such as HITRAN16 (Gordon et al., 2017), and TheoRETS (Rey et al., 2018) extend the lower wavelength limit to 1.0 and 0.75 μm , respectively, but these still fail to cover the spectral region where dark spots are most visible. We repeated some of our retrievals for 0.76 – 2.5 μm region alone, using k-tables generated from the methane band parameters (Karkoschka & Tomasko, 2010) and also from the TheoRETS database and found better fits to the observations with TheoRETS, and broadly similar retrieved aerosol structures and scattering parameters for the two different sources of methane absorption data. However, significant differences were found between the aerosol structures retrieved from the 0.76 – 2.5 μm using using the methane band/k-data and those retrieved from the full 0.3 – 2.5 μm range, with significantly more opacity of the deep Aerosol-1 layer estimated when using the restricted wavelength range. This may go some way to explaining the difference between the vertical profiles of aerosol retrieved here and those from previous studies, concentrating on the 820 nm or H-band regions alone, that did not include a separate deep Aerosol-1 layer and generally put the main Aerosol-2 layer deeper at 2–3 bar, and for the 820 nm retrievals deduced a lower methane abundance for Neptune (Irwin et al., 2021). It is only the methane band data of Karkoschka and Tomasko (2010) that allows us to analyse the whole range simultaneously and deduce the presence of the deeper layer Aerosol-1 layer, whose spatial variations are, we suggest, responsible for dark spot features.

We did attempt trying to combine the band and line data together, but there are significant differences in the wavelength regions of overlap and we found, generally, that the fits were worse when using a combination of methane data from different sources. In order to extend this analysis we really need for the line data sources to extend to 0.3 μm so that we are able to analyse the whole spectral range with a self-consistent set of absorption data. We look forward to the time when this might be possible.

4.4 Spatial Deconvolution

While the HST/STIS observations presented here have been spatially deconvolved with a Lucy-Richardson deconvolution scheme, this has not yet been possible with the Gemini/NIFS data we have analysed. For Uranus we do not consider this to be too significant a problem since the disc of Uranus seen in 2009 was moderately featureless. However, for the Neptune observations, there were significant levels of high methane ice clouds. Although we masked these regions when extracting the Minnaert coefficients of the back-

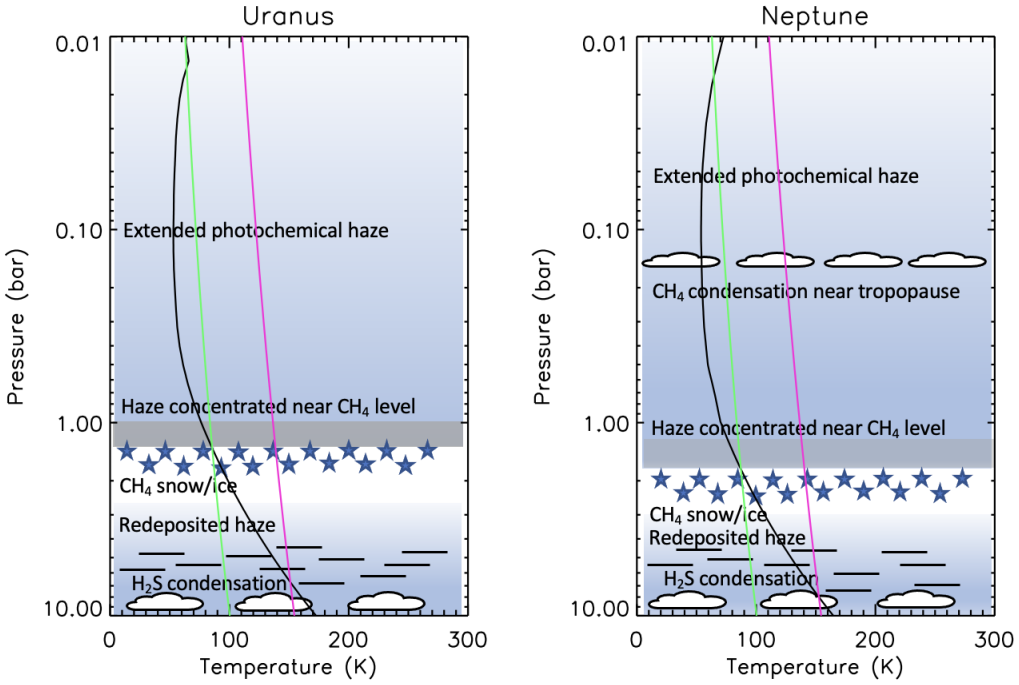


Figure 23. Summary of retrieved aerosol distributions for Uranus (left) and Neptune (right), compared with the assumed temperature/pressure profiles. On each plot is also shown the condensation lines for CH₄ (green) and H₂S (pink), assuming mole fractions at 10 bar of 4% for CH₄ and 1×10^{-3} for H₂S, to move the condensation levels to the approximate levels of the Aerosol-1 and Aerosol-2 layers. The default solution is composed of: A) an extended layer of haze, photochemically-produced in the stratosphere and mixed by eddy diffusion to lower levels (Aerosol-3); B) a thicker haze layer of larger particles ($r \sim 1 \mu\text{m}$) near the CH₄ condensation level (Aerosol-2); C) rapid formation of large methane ice/snow particles at the base of this layer, which rapidly fall and redeposit the haze cores at lower altitudes; and D) an H₂S cloud based at $p > 5 - 7$ bar, which forms on the haze particles (Aerosol-1). For Neptune, we find we also need a component of moderate-sized ($\sim 2 \mu\text{m}$) methane ice particles near the tropopause. Note that the Aerosol-2 layer on Neptune has noticeably less opacity than that on Uranus, by a factor of ~ 2 .

1275
1276
1277
1278
1279
1280
1281

ground regions, given the likely shape of the Point-Spread-Function (PSF) it is possible that the unmasked regions were still contaminated by light from the bright, cloudy regions, which may help to explain why the NIFS Neptune data show very little limb-brightening at methane-absorbing wavelengths, in contrast to the expectations from the fits to the combined data and also to the behaviour seen in the Uranus NIFS observations. We hope, when possible, in future work to attempt to spatially deconvolve these Gemini/NIFS observations to explore this.

1282
1283
1284
1285
1286
1287

5 Conclusions

Modelling the visible/near-infrared reflectivity spectra of Uranus and Neptune over a wide wavelength range of 0.3–2.5 μm represents a considerable challenge. In effect we are trying to find a cloud/haze structure of unknown constituents, of unknown size and unknown complex refractive index spectra, using as our main probe of vertical level the absorption spectrum of gaseous methane, which also has unknown systematic errors. Add

to that the uncertain measurement error of the observed data themselves and it can be seen that this is a considerably degenerate problem! Hence, there are multiple solutions that fit equally well and all may need to be revised once the available line data of methane have been extended to the visible. However, by performing our ‘snippet analyses’, we have shown how we can differentiate between spectral and vertical variations of the Ice Giant aerosols. Using the snippet analyses to constrain our traditional retrieval approach (modified to use multiple starting points to avoid the solutions becoming trapped in local χ^2/n minima) we have determined an aerosol model for Uranus and Neptune that matches the observations well and is simple, elegant, has some basis in terms of haze production and likely pressure levels of static stability, and serendipitously can also explain the observed characteristics of Neptune’s (and Uranus’s) dark spots.

In summary, in this work we have found that we can model the observed reflectivity spectra of both Uranus and Neptune from 0.3 to 2.5 μm with a single, simple aerosol model, summarised in Fig. 23, comprised of:

1. A deep layer based at $p > 5\text{--}7$ bar (Aerosol-1) of what we assume to be sub-micron-sized particles, which we suggest to be coincident with the main H₂S cloud/haze condensation layer and composed of a mixture of photochemically-produced haze particles and H₂S ice. These particles are highly scattering at 500 nm, but become more absorbing at both shorter and longer wavelengths;
2. A vertically thin aerosol layer of micron-sized particles just above the methane condensation level at 1–2 bar (Aerosol-2), possibly composed of a mixture of photochemically-produced haze and methane ice, that are less reflective than the deeper Aerosol-1 haze particles at visible wavelengths and are also more absorbing at both shorter and longer wavelengths;
3. A vertically extended haze of small particles based at 1–2 bar (Aerosol-3) with a fractional scale height of ~ 2 and similar refractive index spectrum to the main 1–2-bar Aerosol-2 layer;
4. For Neptune, an additional vertically thin component of moderate-sized methane ice particles ($\sim 2 \mu\text{m}$), located at ~ 0.2 bar just below the tropopause .

We find this model to be consistent with HST/STIS, HST/WFC3, IRTF/SpeX, Gemini/NIFS and Voyager-2/ISS observations. Our main conclusions are:

1. The UV- and long-wavelength-absorbing nature of the retrieved imaginary refractive index spectrum of the 1–2-bar Aerosol-2 layer is not consistent with our expectation for CH₄ or H₂S ice. The spectral dependence is more consistent with the imaginary refractive index spectrum derived for the tropospheric/stratospheric haze. Hence, we suggest that the 1–2-bar Aerosol-2 layer contains a considerable fraction of photochemical haze, produced at higher altitudes, which has somehow become concentrated and modified at this level in a region of static stability created by vertical gradient in molecular weight and also latent heat release from methane condensation.
2. The haze particles in the 1–2-bar Aerosol-2 layer act as cloud-condensation nuclei (CCN) for methane condensation at the lower boundary, which condenses so quickly that methane ice immediately ‘snows out’ to re-evaporate at deeper levels, redepositing the haze particles there. The larger retrieved size of the particles in the Aerosol-2 layer compared with the higher, vertically extended Aerosol-3 layer may in part reflect this cloud-seeding process and may also just arise due to coagulation and coalescence in this vertically stable layer.
3. The haze particles at deeper levels act as CCNs for H₂S condensation at $\sim 4\text{--}10$ bar (Aerosol-1). At the low partial pressures of H₂S seen at these levels and the higher pressure, this condensation is slower, forming a cloud of what we have as-

- 1338 sumed to be sub-micron-sized particles, which have spectral properties consistent
 1339 with a mix of dark haze and ice.
- 1340 4. In Neptune's atmosphere, increased reflectance in methane absorption bands at
 1341 wavelengths longer than $\sim 1 \mu\text{m}$ can be accounted for by the addition of an opti-
 1342 cally and vertically thin component of micron-sized methane ice particles, based
 1343 near 0.2 bar, just below the tropopause.
- 1344 5. Darkening of the particles in the deep haze/ H_2S -ice Aerosol-1 layer (or to a lesser
 1345 extent a clearing of this layer) leads to spectral perturbations that match well the
 1346 observed characteristics of dark spots and the dark latitude bands seen in Voyager-
 1347 2/ISS and HST/WFC3 observations of Neptune (i.e., visibility only at $\lambda < \sim 700$
 1348 nm). Such perturbations also provide a good fit to observed limb-darkening prop-
 1349 erties of these features. At the same time, the Aerosol-2 layer (1–2 bar) appears
 1350 to be unperturbed by dark regions. This potentially limits the vertical thickness
 1351 of dark spots (and dark latitudes) to disturbances at pressures greater than ~ 3 -
 1352 bar, and perhaps spanning less than 2 scale heights, a significant difference from
 1353 thicker anticyclones seen in Jupiter's atmosphere. However, such an interpreta-
 1354 tion does not rest easily with the observation that such features are frequently ac-
 1355 companied by orographic clouds, based near the tropopause. Hence, it may be that
 1356 the vortex mid-plane coincides with the 1–2-bar Aerosol-2 layer.
- 1357 6. The opacity of the 1–2-bar Aerosol-2 layer in Uranus's atmosphere is found to be
 1358 significantly thicker than that of Neptune by a factor of ~ 2 ; since these parti-
 1359 cles are found to be UV-absorbing, this explains Uranus's lower observed UV re-
 1360 flectivity and also explains why Uranus appears to have a paler blue colour to the
 1361 human eye than Neptune since these particles are found to have a roughly white
 1362 visible reflectivity spectrum. The lower opacity of Neptune's Aerosol-2 layer also
 1363 explains why dark spots, caused, we suggest, by perturbations of the deep Aerosol-
 1364 1 H_2S /haze layer are easier to observe in Neptune's atmosphere than in Uranus's.
 1365 We suggest that the Aerosol-2 layer on Neptune may be thinner than that of Uranus
 1366 due to Neptune's dynamically overturning atmosphere being more efficient at clear-
 1367 ing this haze layer through methane condensation.
- 1368 7. Future observations of Uranus and Neptune with instruments such as HST/STIS
 1369 or VLT/MUSE, able to return high spectral resolution hyperspectral cubes at vis-
 1370 ible wavelengths, may help to resolve the question of whether dark spots and dark
 1371 regions are caused by a darkening or a clearing of the Aerosol-1 layer. This will,
 1372 we hope, be the focus of future work.

Acknowledgments

We are grateful to the United Kingdom Science and Technology Facilities Council for funding this research (Irwin: ST/S000461/1, Teanby: ST/R000980/1). Glenn Orton was supported by funding to the Jet Propulsion Laboratory, California Institute of Technology, under a contract with the National Aeronautics and Space Administration (80NM0018D0004). Leigh Fletcher and Mike Roman were supported by a European Research Council Consolidator Grant (under the European Union's Horizon 2020 research and innovation programme, grant agreement No 723890) at the University of Leicester. Santiago Pérez-Hoyos is supported by grant PID2019-109467GB-I00Z, funded by MCIN/AEI/10.13039/501100011033. We are also grateful for the assistance of Larry Sromovsky and Pat Fry in locating and reading the HST/STIS data. We are also grateful to the PDS Ring-Moon Systems Node's OPUS search service for providing access to the Voyager-2 ISS images. Finally, the Gemini/NIFS observations used were obtained at the international Gemini Observatory, a program of NSF's NOIRLab, which is managed by the Association of Universities for Research in Astronomy (AURA) under a cooperative agreement with the National Science Foundation, on behalf of the Gemini Observatory partnership: the National Science Foundation (United States), National Research Council

(Canada), Agencia Nacional de Investigación y Desarrollo (Chile), Ministerio de Ciencia, Tecnología e Innovación (Argentina), Ministério da Ciência, Tecnologia, Inovações e Comunicações (Brazil), and Korea Astronomy and Space Science Institute (Republic of Korea).

6 Data Availability

The Uranus HST/STIS datasets used in this study are available from Fry and Karkoschka (2018), while the Neptune/STIS dataset is available from Irwin (2022). The IRTF/SpeX observations are available from http://irtfweb.ifa.hawaii.edu/~spex/IRTF_Spectral_Library/References_files/Planets.html. The Uranus Gemini/NIFS data are available at <https://archive.gemini.edu/searchform/GN-2009B-Q-52/>, while the Neptune Gemini/NIFS data are available at <https://archive.gemini.edu/searchform/GN-2009B-Q-85/>. The Voyager ISS images were downloaded from <https://bit.ly/3qjuqk6>. The spectral fitting and retrievals were performed using the NEMESIS radiative transfer and retrieval algorithm Irwin et al. (2008) and can be downloaded from Irwin, Teanby, de Kok, et al. (2022a), with supporting website information at Irwin, Teanby, de Kok, et al. (2022b). The data products generated in this study (processed spectra and retrieved atmospheric parameters) are available from Irwin, Teanby, Fletcher, et al. (2022).

Appendix A Bouyancy Forces

Consider the force acting in the vertical direction z on a parcel of air at altitude z_0 of cross-sectional area A , height dz , and density ρ :

$$\rho Adz \frac{d^2z}{dt^2} = -\rho g Adz + \rho_0 g Adz \quad (\text{A1})$$

where ρ_0 is the density of the surrounding air and g is the gravitational acceleration. Dividing by $A\rho dz$ we have:

$$\frac{d^2z}{dt^2} = -g \frac{(\rho - \rho_0)}{\rho}. \quad (\text{A2})$$

The density can be written as $\rho = \frac{Mp}{RT}$, where M is the molecular weight of the air, p is the pressure, T is the temperature and R is the gas constant. Hence, we can rewrite this equation as:

$$\frac{d^2z}{dt^2} = -g \frac{\left(\frac{Mp}{RT} - \frac{M_0 p}{R T_0}\right)}{\frac{Mp}{RT}} \quad (\text{A3})$$

where we have assumed the parcel and the surroundings have the same pressure. Rearranging this equation we find:

$$\frac{d^2z}{dt^2} = -g \left(1 - \frac{M_0}{M} \frac{T}{T_0}\right) = -g \left(1 - \frac{M_0}{M} \frac{\theta}{\theta_0}\right) \quad (\text{A4})$$

where θ is the potential temperature of the parcel (i.e., the temperature it would have if compressed or expanded adiabatically to a reference pressure p_0), defined for the parcel to be $\theta = T\left(\frac{p_0}{p}\right)^\gamma$, where $\gamma = R/C_p$ and C_p is the molar heat capacity at constant pressure. The potential temperature of the surrounding air is similarly $\theta_0 = T_0\left(\frac{p_0}{p}\right)^\gamma$ and hence $\frac{T}{T_0} = \frac{\theta}{\theta_0}$.

If the parcel moves adiabatically then its potential temperature and molecular weight remain constant (if no condensation) so any buoyancy must be due to changes in M_0 and T_0 . We know that the acceleration $a = \frac{d^2z}{dt^2} = 0$ at $z = z_0$ by definition and so

$$\frac{d^2z}{dt^2} \sim \left(\frac{da}{dz}\right)_{z_0} (z - z_0) \quad (\text{A5})$$

Accepted Article

where

$$\left(\frac{da}{dz}\right)_{z_0} = g \frac{\theta}{M} \frac{d}{dz} \left(\frac{M_0}{\theta_0} \right) = g \frac{\theta}{M} \frac{\theta_0 \frac{dM_0}{dz} - M_0 \frac{d\theta_0}{dz}}{\theta_0^2}. \quad (\text{A6})$$

At $z = z_0$, $\theta = \theta_0$ and $M = M_0$, and hence:

$$\left(\frac{da}{dz}\right)_{z_0} = g \left(-\frac{1}{\theta_0} \frac{d\theta_0}{dz} + \frac{1}{M_0} \frac{dM_0}{dz} \right) \quad (\text{A7})$$

or

$$\left(\frac{da}{dz}\right)_{z_0} = g \frac{d}{dz} \left(\ln \left(\frac{M_0}{\theta_0} \right) \right). \quad (\text{A8})$$

Hence

$$\frac{d^2z}{dt^2} = -g \frac{d}{dz} \left(\ln \left(\frac{\theta_0}{M_0} \right) \right) (z - z_0). \quad (\text{A9})$$

This is simple harmonic motion, with an angular frequency, N , known as the Brünt-Väisälä frequency, given by

$$N^2 = g \frac{d}{dz} \left(\ln \left(\frac{\theta_0}{M_0} \right) \right). \quad (\text{A10})$$

This is different from the more familiar definition of the Brünt-Väisälä frequency that ignores molecular weight changes:

$$N^2 = g \frac{d}{dz} \left(\ln \theta_0 \right). \quad (\text{A11})$$

Accepted Article

Appendix B Disc-averaging

The disc-averaged radiance \bar{I} of a planet of apparent radius R is defined as:

$$\bar{I} = \frac{1}{\pi R^2} \int_{r=0}^{r=R} \int_{\phi=0}^{\phi=2\pi} I r dr d\phi \quad (\text{B1})$$

where r is the radial position on the disc and ϕ is the azimuth angle. Substituting $r = R \sin \theta$, where θ is the local zenith angle, this becomes

$$\bar{I} = \frac{1}{\pi} \int_{\theta=0}^{\theta=\pi/2} \int_{\phi=0}^{\phi=2\pi} I \sin \theta \cos \theta d\theta d\phi. \quad (\text{B2})$$

Assuming the radiance I is azimuthally symmetric, i.e., does not depend on ϕ , this simplifies to

$$\bar{I} = 2 \int_0^{\pi/2} I(\theta) \sin \theta \cos \theta d\theta = \int_0^{\pi/2} I(\theta) \sin 2\theta d\theta \quad (\text{B3})$$

or

$$\bar{I} = 2 \int_0^1 I(\mu) \mu d\mu \quad (\text{B4})$$

where $\mu = \cos \theta$. If we assume that $I(\mu)$ is well approximated by Minnaert limb darkening and that $\mu = \mu_0$, then $I(\mu) = I_0 \mu^{2k-1}$. Hence, the disc-averaged radiance \bar{I} will be

$$\bar{I} = 2I_0 \int_0^1 \mu^{2k} d\mu = \frac{2I_0}{2k+1}. \quad (\text{B5})$$

The ‘disc-averaged’ IRTF/SpeX spectra are actually line-integrals along the central meridian, for which:

$$\bar{I} = \frac{\int I dy dx}{\int dy dx} \sim \frac{\Delta x \int I dy}{2R \Delta x} = \frac{\int I dy}{2R} \quad (\text{B6})$$

where y is the distance along the slit, x is the position across it, and Δx is the slit width (assumed to be small). Substituting $y = R \sin \theta$ this becomes

$$\bar{I} = \frac{1}{2} \int_{-\pi/2}^{\pi/2} I(\theta) \cos \theta d\theta = \int_0^{\pi/2} I(\theta) \cos \theta d\theta. \quad (\text{B7})$$

Assuming $I(\theta)$ is Minnaert-dependent (i.e., $I(\theta) = I_0(\cos \theta)^{2k-1}$) this becomes

$$\bar{I} = I_0 \int_0^{\pi/2} (\cos \theta)^{2k} d\theta. \quad (\text{B8})$$

Sadly, this is not simply integrable for a general, non-integer k , but it may be evaluated numerically. This can be done either by pre-tabulating \bar{I}/I_0 as a function of k , or alternatively calculating $I(\theta)$ at all the quadrature zenith angles of the radiative transfer model and integrating $I(\theta) \cos(\theta)$ using the quadrature scheme weights. Both approaches were tested and found to give similar results. However, with the 5-point Gaussian-Lobatto scheme we generally use, the latter approach was found to be much slower since calculations at the higher zenith angles need many more Fourier components to fully resolve the azimuthal part of the radiance calculation. Instead, calculating at just two zenith angles ($0, 42.47^\circ$), extracting the minnaert- k coefficients I_0 and k , and using the pre-tabulated dependence of \bar{I}/I_0 on k to calculate \bar{I} was found to be more than twice as fast and of equivalent accuracy.

Appendix C Cloud Opacity Units

The default units for particle cross-sections, $\chi(\lambda)$, in NEMESIS are $\text{cm}^2/\text{particle}$, while the default units of aerosol density, $D(p)$, are particles/gram. Hence, $\chi(\lambda)D(p)$ gives aerosol cross-section in units of cm^2/gram (i.e., cm^2 per gram of atmosphere).

To get opacity we need to multiply this cross-section by the path amount, u , which has units of gram/cm^2 , and can be calculated as $u = \rho z$, where z is the path length in cm and ρ is the atmospheric density in units of gram/cm^3 . Hence, the opacity of a path at wavelength, λ , is $\tau(\lambda) = \chi(\lambda)D(p)u = \chi(\lambda)D(p)\rho z$, which is unit-less. The opacity per km in a vertical path of atmosphere is then simply $\frac{d\tau}{dz} = 10^5 \chi(\lambda)D(p)\rho$.

Other authors commonly express cloud profiles in units of opacity/bar, $\frac{d\tau(\lambda)}{dp}$, which by the chain rule can be calculated as $\frac{d\tau(\lambda)}{dz} \cdot \frac{dz}{dp}$. Assuming hydrostatic equilibrium, $p = p_0 e^{z/H}$, where H is the Scale Height and z is measured downwards, and thus $\frac{dp}{dz} = \frac{p}{H}$ and $\frac{d\tau(\lambda)}{dp} = 10^5 \chi(\lambda)D(p)\rho \frac{H}{p}$. Substituting for the Scale Height, $H = RT/Mg$ and for atmospheric density, $\rho = pM/RT$, we conclude that the cloud opacity per bar is

$$\frac{d\tau(\lambda)}{dp} = 10^5 \frac{\chi(\lambda)D(p)}{g(p)} \quad (\text{C1})$$

where $g(p)$ is the gravitational acceleration at pressure level, p .

In NEMESIS we usually normalise the aerosol density profile, $D(p)$ and cross-section spectra, $\chi(\lambda)$, such that the cross section is 1.0 at a reference wavelength, λ_0 , and the

1444 normalised dust opacity profile $D'(p) = D(p)\chi(\lambda_0)$. In this case, the opacity/bar at λ_0
 1445 is related to the scaled aerosol density, $D'(p)$, as

$$\frac{d\tau(\lambda_0)}{dp} = 10^5 \frac{D'(p)}{g(p)}. \quad (\text{C2})$$

1446 Appendix D Eddy diffusion coefficients

1447 Following the method of Ackerman and Marley (2001) we assume the eddy diffu-
 1448 sion coefficient K_{zz} is the same as that for free convection, which Gierasch and Conrath
 1449 (1985) derive to be:

$$K_{zz} = \frac{H}{3} \left(\frac{L}{H} \right)^{4/3} \left(\frac{RF}{\mu \rho_a c_p} \right)^{1/3} \quad (\text{D1})$$

1450 where H is the atmospheric scale height, μ is the atmospheric molecular weight,
 1451 c_p is the specific heat capacity at constant pressure (i.e., $\text{J K}^{-1} \text{kg}^{-1}$), R is the gas con-
 1452 stant ($8.31 \text{ J K}^{-1} \text{ mol}^{-1}$), ρ_a is the atmospheric density (kg m^{-3}), and F is the convec-
 1453 tive heat flux (W m^{-2}). This equation can also be slightly more simply re-expressed as:

$$K_{zz} = \frac{H}{3} \left(\frac{L}{H} \right)^{4/3} \left(\frac{RF}{\rho_a C_p} \right)^{1/3} \quad (\text{D2})$$

1454 where C_p is the molar heat capacity at constant pressure (i.e., $\text{J K}^{-1} \text{ mol}^{-1}$).

1455 In this equation, L is the *turbulent mixing length*. For a freely convecting atmo-
 1456 sphere, this is typically assumed to be the atmospheric scale height, but in regions of at-
 1457 mospheric stability, Ackerman and Marley (2001) apply a scaling factor:

$$L = H \max(\Lambda, \Gamma/\Gamma_d) \quad (\text{D3})$$

1458 where Γ is the local lapse rate (i.e., $-\frac{dT}{dz}$) and Γ_d is the dry adiabatic lapse rate.
 1459 The parameter Λ is present to prevent L becoming negative and was assumed by Ackerman
 1460 and Marley (2001) to have a value of 0.1. In this study, where a large part of the atmo-
 1461 spheric stability is assumed to come from the vertical variation of molecular weight, we
 1462 modified this scaling to:

$$L = H \max \left(\Lambda, \frac{\Gamma}{\Gamma_d} \left(1 - \alpha \frac{d\mu}{dz} \right) \right) \quad (\text{D4})$$

1463 where the factor α was set to be:

$$\alpha = \frac{1 - 0.0001}{\max \left(\left| \frac{d\mu}{dz} \right| \right)}. \quad (\text{D5})$$

1464 Also, to force the profile of K_{zz} to be consistent with stratospheric determinations
 1465 for Fouchet et al. (2003), we reduced the factor Λ from 0.1 to 0.0001.

1466 **References**

- 1467 Ackerman, A. S., & Marley, M. S. (2001, August). Precipitating Condens-
 1468 ation Clouds in Substellar Atmospheres. *ApJ*, *556*(2), 872-884. doi:
 1469 10.1086/321540
- 1470 Asplund, M., Grevesse, N., Sauval, A. J., & Scott, P. (2009, September). The Chemical
 1471 Composition of the Sun. *ARA&A*, *47*(1), 481-522. doi: 10.1146/annurev.
 1472 .astro.46.060407.145222
- 1473 Banfield, D., Gierasch, P. J., Bell, M., Ustinov, E., Ingersoll, A. P., Vasavada, A. R.,
 1474 ... Belton, M. J. S. (1998, September). Jupiter's Cloud Structure from Galileo
 1475 Imaging Data. *Icarus*, *135*(1), 230-250. doi: 10.1006/icar.1998.5985
- 1476 Barceló-Llull, B., Sangrà, P., Pallàs-Sanz, E., Barton, E. D., Estrada-Allis, S. N.,
 1477 Martínez-Marrero, A., ... Arístegui, J. (2017, June). Anatomy of a subtropical
 1478 intrathermocline eddy. *Deep Sea Research Part I: Oceanographic Research*,
 1479 *124*, 126-139. doi: 10.1016/j.dsr.2017.03.012
- 1480 Bolton, S., Levin, S., Guillot, T., & et al. (2021, October). Microwave observations
 1481 reveal the deep extent and structure of Jupiters atmospheric vortices. *Science*,
 1482 *374*, 968. doi: 10.1126/science.abf1015
- 1483 Borysow, A., Borysow, J., & Fu, Y. (2000, June). Semi-empirical Model of Collision-
 1484 Induced Absorption Spectra of H₂-H₂ Complexes in the Second Overtone
 1485 Band of Hydrogen at Temperatures from 50 to 500 K. *Icarus*, *145*(2), 601-608.
 1486 doi: 10.1006/icar.2000.6384
- 1487 Borysow, A., & Frommhold, L. (1989, June). Collision-induced Infrared Spectra of
 1488 H₂-He Pairs at Temperatures from 18 to 7000 K. II. Overtone and Hot Bands.
 1489 *ApJ*, *341*, 549. doi: 10.1086/167515
- 1490 Borysow, A., Frommhold, L., & Moraldi, M. (1989, January). Collision-induced
 1491 Infrared Spectra of H₂-He Pairs Involving 0 1 Vibrational Transitions and
 1492 Temperatures from 18 to 7000 K. *ApJ*, *336*, 495. doi: 10.1086/167027
- 1493 Campargue, A., Leshchishina, O., Wang, L., Mondelain, D., & Kassi, S. (2013,
 1494 September). The WKLMC empirical line lists (5852-7919 cm⁻¹) for
 1495 methane between 80 K and 296 K: "Final" lists for atmospheric and plan-
 1496 etary applications. *Journal of Molecular Spectroscopy*, *291*, 16-22. doi:
 1497 10.1016/j.jms.2013.03.001
- 1498 Carlson, B. E., Rossow, W. B., & Orton, G. S. (1988, July). Cloud microphysics of
 1499 the giant planets. *Journal of Atmospheric Sciences*, *45*, 2066-2081. doi: 10
 1500 .1175/1520-0469(1988)045<2066:CMOTGP>2.0.CO;2
- 1501 Cavalie, T., Venot, O., Selsis, F., Hersant, F., Hartogh, P., & Leconte, J. (2017).
 1502 Thermochemistry and vertical mixing in the tropospheres of Uranus and Nep-
 1503 tune: how convection inhibition can affect the derivation of deep oxygen abun-
 1504 dances. *Icarus*, *291*, 1-16. doi: 10.1016/j.icarus.2017.03.015
- 1505 Chance, K., & Kurucz, R. L. (2010, June). An improved high-resolution so-
 1506 lar reference spectrum for earth's atmosphere measurements in the ul-
 1507 traviolet, visible, and near infrared. *JQSRT*, *111*(9), 1289-1295. doi:
 1508 10.1016/j.jqsrt.2010.01.036
- 1509 Cheng, A. F., Simon-Miller, A. A., Weaver, H. A., Baines, K. H., Orton, G. S.,
 1510 Yanamandra-Fisher, P. A., ... Noll, K. S. (2008, June). Changing Char-
 1511 acteristics of Jupiter's Little Red SPOT. *AJ*, *135*(6), 2446-2452. doi:
 1512 10.1088/0004-6256/135/6/2446
- 1513 Dalzell, W. H., & Sarofim, A. S. (1969, February). Optical Constants of Soot and
 1514 Their Application to Heat-Flux Calculations. *Journal of Heat Transfer*, *91*(1),
 1515 100-104. doi: 10.1115/1.3580063
- 1516 de Kleer, K., Luszcz-Cook, S., de Pater, I., Ádámkovics, M., & Hammel, H. B.
 1517 (2015, August). Clouds and aerosols on Uranus: Radiative transfer modeling
 1518 of spatially-resolved near-infrared Keck spectra. *Icarus*, *256*, 120-137. doi:
 1519 10.1016/j.icarus.2015.04.021

- 1520 Dressel, L. (2021). WFC3 Instrument Handbook for Cycle 29 v. 13. In *Wfc3 instrument handbook for cycle 29 v. 13* (Vol. 13, p. 13).
- 1521 Encrenaz, T., Feuchtgruber, H., Atreya, S. K., Bezard, B., Lellouch, E., Bishop, J.,
1522 ... Kessler, M. F. (1998, May). ISO observations of Uranus: The stratospheric
1523 distribution of C_2H_2 and the eddy diffusion coefficient. *A&A*, 333, L43-L46.
- 1524 Ferman, M. A., Wolff, G. T., & Kelly, N. A. (1981). The Nature and Sources
1525 of Haze in the Shenandoah Valley/Blue Ridge Mountains Area. *Journal of the Air Pollution Control Association*, 31(10), 1074-1082.
1526 Retrieved from <https://doi.org/10.1080/00022470.1981.10465329> doi:
1527 10.1080/00022470.1981.10465329
- 1528 Feuchtgruber, H., Lellouch, E., de Graauw, T., Bézard, B., Encrenaz, T., & Griffin,
1529 M. (1997). External supply of oxygen to the atmospheres of the giant planets.
1530 *Nature*, 389, 159–162.
- 1531 Fletcher, L. N., Orton, G. S., Mousis, O., Yanamandra-Fisher, P., Parrish, P. D.,
1532 Irwin, P. G. J., ... De Buizer, J. (2010, July). Thermal structure and com-
1533 position of Jupiter's Great Red Spot from high-resolution thermal imaging.
1534 *Icarus*, 208(1), 306-328. doi: 10.1016/j.icarus.2010.01.005
- 1535 Ford, A. L., & Browne, J. C. (1973, January). Rayleigh and Raman Cross Sections
1536 for the Hydrogen Molecule. *Atomic Data*, 5, 305. doi: 10.1016/S0092-640X(73)
1537 80011-7
- 1538 Fouchet, T., Lellouch, E., & Feuchtgruber, H. (2003, January). The hydrogen ortho-
1539 to-para ratio in the stratospheres of the giant planets. *Icarus*, 161(1), 127-143.
1540 doi: 10.1016/S0019-1035(02)00014-3
- 1541 Fry, P., & Karkoschka, E. (2018). *Hyperspectral cubes from mosaicked STIS ob-*
1542 *1543 servations of Uranus ("URANUS-STIS")* [dataset]. Mikulski Archive for
1544 Space Telescopes. Retrieved from <https://archive.stsci.edu/prepds/uranus-stis/> doi: 10.17909/t9kq4n
- 1545 Gierasch, P. J., & Conrath, B. J. (1985). Energy conversion processes in the
1546 outer planets. In G. E. Hunt (Ed.), *Recent advances in planetary meteorol-*
1547 *ogy* (p. 121-146).
- 1548 Gordon, I. E., Rothman, L. S., Hill, C., Kochanov, R. V., Tan, Y., Bernath, P. F.,
1549 ... Zak, E. J. (2017, December). The HITRAN2016 molecular spectroscopic
1550 database. *JQSRT*, 203, 3-69. doi: 10.1016/j.jqsrt.2017.06.038
- 1551 Guillot, T. (1995, September). Condensation of Methane, Ammonia, and Water and
1552 the Inhibition of Convection in Giant Planets. *Science*, 269(5231), 1697-1699.
1553 doi: 10.1126/science.7569896
- 1554 Hadland, N., Sankar, R., LeBeau, J., Raymond Paul, & Palotai, C. (2020, August).
1555 EPIC simulations of Neptune's dark spots using an active cloud microphysical
1556 model. *MNRAS*, 496(4), 4760-4768. doi: 10.1093/mnras/staa1799
- 1557 Hammel, H. B., Lockwood, G. W., Mills, J. R., & Barnet, C. D. (1995, June). Hubble
1558 Space Telescope Imaging of Neptune's Cloud Structure in 1994. *Science*,
1559 268(5218), 1740-1742. doi: 10.1126/science.268.5218.1740
- 1560 Hammel, H. B., Sromovsky, L. A., Fry, P. M., Rages, K., Showalter, M., de Pater,
1561 I., ... Deng, X. (2009, May). The Dark Spot in the atmosphere of Uranus
1562 in 2006: Discovery, description, and dynamical simulations. *Icarus*, 201(1),
1563 257-271. doi: 10.1016/j.icarus.2008.08.019
- 1564 Hassanzadeh, P., Marcus, P. S., & Le Gal, P. (2012, September). The universal as-
1565 pect ratio of vortices in rotating stratified flows: theory and simulation. *Jour-*
1566 *1567 nal of Fluid Mechanics*, 706, 46-57. doi: 10.1017/jfm.2012.180
- 1568 Hsu, A. I., Wong, M. H., & Simon, A. A. (2019, April). Lifetimes and Occurrence
1569 Rates of Dark Vortices on Neptune from 25 Years of Hubble Space Telescope
1570 Images. *AJ*, 157(4), 152. doi: 10.3847/1538-3881/ab0747
- 1571 Hunten, D. M. (2008, April). Transport of nonmethane hydrocarbons to Jupiter's
1572 troposphere by descent of smog particles. *Icarus*, 194(2), 616-622. doi: 10
1573 .1016/j.icarus.2007.11.012

- 1575 Irwin, P. G. J. (2022). *HST/STIS observations of Neptune from 2003. (v1.0.1)*
 1576 [dataset]. Zenodo. Retrieved from [https://doi.org/10.5281/zenodo](https://doi.org/10.5281/zenodo.5837531)
 1577 .5837531 doi: 10.5281/zenodo.5837531
- 1578 Irwin, P. G. J., de Bergh, C., Courtin, R., Bézard, B., Teanby, N. A., Davis, G. R.,
 1579 ... Hurley, J. (2012, August). The application of new methane line absorption
 1580 data to Gemini-N/NIFS and KPNO/FTS observations of Uranus' near-infrared
 1581 spectrum. *Icarus*, 220(2), 369-382. doi: 10.1016/j.icarus.2012.05.017
- 1582 Irwin, P. G. J., Dobinson, J., James, A., Toledo, D., Teanby, N. A., Fletcher, L. N.,
 1583 ... Pérez-Hoyos, S. (2021, March). Latitudinal variation of methane mole
 1584 fraction above clouds in Neptune's atmosphere from VLT/MUSE-NFM: Limb-
 1585 darkening reanalysis. *Icarus*, 357, 114277. doi: 10.1016/j.icarus.2020.114277
- 1586 Irwin, P. G. J., Fletcher, L. N., Tice, D., Owen, S. J., Orton, G. S., Teanby, N. A.,
 1587 & Davis, G. R. (2016, June). Time variability of Neptune's horizontal and
 1588 vertical cloud structure revealed by VLT/SINFONI and Gemini/NIFS from
 1589 2009 to 2013. *Icarus*, 271, 418-437. doi: 10.1016/j.icarus.2016.01.015
- 1590 Irwin, P. G. J., Teanby, N. A., Davis, G. R., Fletcher, L. N., Orton, G. S., Calcutt,
 1591 S. B., ... Hurley, J. (2012, March). Further seasonal changes in Uranus' cloud
 1592 structure observed by Gemini-North and UKIRT. *Icarus*, 218(1), 47-55. doi:
 1593 10.1016/j.icarus.2011.12.001
- 1594 Irwin, P. G. J., Teanby, N. A., Davis, G. R., Fletcher, L. N., Orton, G. S., Tice, D.,
 1595 ... Calcutt, S. B. (2011a, November). Multispectral imaging observations of
 1596 Neptune's cloud structure with Gemini-North. *Icarus*, 216(1), 141-158. doi:
 1597 10.1016/j.icarus.2011.08.005
- 1598 Irwin, P. G. J., Teanby, N. A., Davis, G. R., Fletcher, L. N., Orton, G. S., Tice, D.,
 1599 & Kyffin, A. (2011b, March). Uranus' cloud structure and seasonal variability
 1600 from Gemini-North and UKIRT observations. *Icarus*, 212(1), 339-350. doi:
 1601 10.1016/j.icarus.2010.12.018
- 1602 Irwin, P. G. J., Teanby, N. A., de Kok, R., Fletcher, L. N., Howett, C. J. A., Tsang,
 1603 C. C. C., ... Parrish, P. D. (2008, April). The NEMESIS planetary atmo-
 1604 sphere radiative transfer and retrieval tool. *JQSRT*, 109, 1136-1150. doi:
 1605 10.1016/j.jqsrt.2007.11.006
- 1606 Irwin, P. G. J., Teanby, N. A., de Kok, R., Fletcher, L. N., Howett, C. J. A.,
 1607 Tsang, C. C. C., ... Parrish, P. D. (2022a). *Nemesis* [Software]. Zen-
 1608 odo. Retrieved from <https://github.com/nemesiscode/radtrancode> doi:
 1609 10.5281/zenodo.5816714
- 1610 Irwin, P. G. J., Teanby, N. A., de Kok, R., Fletcher, L. N., Howett, C. J. A., Tsang,
 1611 C. C. C., ... Parrish, P. D. (2022b). *Nemesis documentation* [Software doc-
 1612 umentation]. Zenodo. Retrieved from <https://github.com/nemesiscode/nemesiscode.github.io> doi: 10.5281/zenodo.5816724
- 1613 Irwin, P. G. J., Teanby, N. A., Fletcher, L. N., Toledo, D., Orton, G. S.,
 1614 Wong, M. H., ... Dobinson, J. (2022). *Associated data files for paper*
 1615 [dataset]. Zenodo. Retrieved from <https://github.com/patrickkirwin/UranusNeptuneAerosol> doi: 10.5281/zenodo.5840961
- 1616 Irwin, P. G. J., Tice, D. S., Fletcher, L. N., Barstow, J. K., Teanby, N. A., Or-
 1617 ton, G. S., & Davis, G. R. (2015, April). Reanalysis of Uranus' cloud
 1618 scattering properties from IRTF/SpeX observations using a self-consistent
 1619 scattering cloud retrieval scheme. *Icarus*, 250, 462-476. doi: 10.1016/
 1620 j.icarus.2014.12.020
- 1621 Irwin, P. G. J., Toledo, D., Braude, A. S., Bacon, R., Weilbacher, P. M., Teanby,
 1622 N. A., ... Orton, G. S. (2019, October). Latitudinal variation in the abun-
 1623 dance of methane (CH_4) above the clouds in Neptune's atmosphere from
 1624 VLT/MUSE Narrow Field Mode Observations. *Icarus*, 331, 69-82. doi:
 1625 10.1016/j.icarus.2019.05.011
- 1626 Irwin, P. G. J., Toledo, D., Garland, R., Teanby, N. A., Fletcher, L. N., Orton,
 1627 G. S., & Bézard, B. (2018, April). Detection of hydrogen sulfide above

- the clouds in Uranus's atmosphere. *Nature Astronomy*, *2*, 420-427. doi: 10.1038/s41550-018-0432-1
- Irwin, P. G. J., Toledo, D., Garland, R., Teanby, N. A., Fletcher, L. N., Orton, G. S., & Bézard, B. (2019, March). Probable detection of hydrogen sulphide (H_2S) in Neptune's atmosphere. *Icarus*, *321*, 550-563. doi: 10.1016/j.icarus.2018.12.014
- Karkoschka, E. (2011, October). Neptune's cloud and haze variations 1994-2008 from 500 HST-WFPC2 images. *Icarus*, *215*(2), 759-773. doi: 10.1016/j.icarus.2011.06.010
- Karkoschka, E., & Tomasko, M. (2009, July). The haze and methane distributions on Uranus from HST-STIS spectroscopy. *Icarus*, *202*(1), 287-309. doi: 10.1016/j.icarus.2009.02.010
- Karkoschka, E., & Tomasko, M. G. (2010, February). Methane absorption coefficients for the jovian planets from laboratory, Huygens, and HST data. *Icarus*, *205*(2), 674-694. doi: 10.1016/j.icarus.2009.07.044
- Karkoschka, E., & Tomasko, M. G. (2011, January). The haze and methane distributions on Neptune from HST-STIS spectroscopy. *Icarus*, *211*(1), 780-797. doi: 10.1016/j.icarus.2010.08.013
- Khare, B. N., Thompson, W. R., Cheng, L., Chyba, C., Sagan, C., Arakawa, E. T., ... Tuminello, P. S. (1993, June). Production and Optical Constants of Ice Tholin from Charged Particle Irradiation of (1:6) C_2H_6/H_2O at 77 K. *Icarus*, *103*(2), 290-300. doi: 10.1006/icar.1993.1071
- Kurucz, R. (1993, January). ATLAS9 Stellar Atmosphere Programs and 2 km/s grid. *ATLAS9 Stellar Atmosphere Programs and 2 km/s grid. Kurucz CD-ROM No. 13. Cambridge*, *13*.
- Leconte, J., Selsis, F., Hersant, F., & Guillot, T. (2017, February). Condensation-inhibited convection in hydrogen-rich atmospheres . Stability against double-diffusive processes and thermal profiles for Jupiter, Saturn, Uranus, and Neptune. *A&A*, *598*, A98. doi: 10.1051/0004-6361/201629140
- Lellouch, E., Hartogh, P., Feuchtgruber, H., Vand enbussche, B., de Graauw, T., Moreno, R., ... Wildeman, K. (2010, July). First results of Herschel-PACS observations of Neptune. *A&A*, *518*, L152. doi: 10.1051/0004-6361/201014600
- Lellouch, E., Moreno, R., & Paubert, G. (2005). A dual origin for Neptune's carbon monoxide? *A&A*, *430*, L37-L40.
- Lemasquier, D., Facchini, G., Favier, B., & Le Bars, M. (2020, March). Remote determination of the shape of Jupiter's vortices from laboratory experiments. *Nature Physics*, *16*(6), 695-700. doi: 10.1038/s41567-020-0833-9
- Li, L., Ingersoll, A. P., Vasavada, A. R., Porco, C. C., Del Genio, A. D., & Ewald, S. P. (2004, November). Life cycles of spots on Jupiter from Cassini images. *Icarus*, *172*(1), 9-23. doi: 10.1016/j.icarus.2003.10.015
- Lindal, G. F. (1992, March). The Atmosphere of Neptune: an Analysis of Radio Occultation Data Acquired with Voyager 2. *AJ*, *103*, 967. doi: 10.1086/116119
- Lindal, G. F., Lyons, J. R., Sweetnam, D. N., Eshleman, V. R., Hinson, D. P., & Tyler, G. L. (1987, December). The atmosphere of Uranus: Results of radio occultation measurements with Voyager 2. *J. Geophys. Res.*, *92*(A13), 14987-15001. doi: 10.1029/JA092iA13p14987
- Lockwood, G. W. (2019, May). Final compilation of photometry of Uranus and Neptune, 1972-2016. *Icarus*, *324*, 77-85. doi: 10.1016/j.icarus.2019.01.024
- Luszcz-Cook, S. H., de Kleer, K., de Pater, I., Adamkovics, M., & Hammel, H. B. (2016, September). Retrieving Neptune's aerosol properties from Keck OSIRIS observations. I. Dark regions. *Icarus*, *276*, 52-87. doi: 10.1016/j.icarus.2016.04.032
- Luszcz-Cook, S. H., & de Pater, I. (2013). Constraining the origins of Neptune's carbon monoxide abundance with CARMA millimeter-wave observations. *Icarus*, *222*, 379–400.

- 1685 Magalhães, J. A., Seiff, A., & Young, R. E. (2002, August). The Stratification of
 1686 Jupiter's Troposphere at the Galileo Probe Entry Site. *Icarus*, *158*(2), 410-433.
 1687 doi: 10.1006/icar.2002.6891
- 1688 Marcus, P. S., Asay-Davis, X., Wong, M. H., & de Pater, I. (2013, 12). Jupiters
 1689 Red Oval BA: Dynamics, Color, and Relationship to Jovian Climate Change.
 1690 *Journal of Heat Transfer*, *135*, 011007. Retrieved from <https://doi.org/10.1115/1.4007666> (011007) doi: 10.1115/1.4007666
- 1691 Minnaert, M. (1941). The reciprocity principle in lunar photometry. *ApJ*, *93*, 403-
 1692 410. doi: 10.1086/144279
- 1693 Molter, E. M., de Pater, I., Luszcz-Cook, S., Hueso, R., Tollefson, J., Alvarez, C., ...
 1694 Wang, F. (2019, March). Analysis of Neptune's 2017 bright equatorial storm.
 1695 *Icarus*, *321*, 324-345. doi: 10.1016/j.icarus.2018.11.018
- 1696 Molter, E. M., de Pater, I., Luszcz-Cook, S., Tollefson, J., Sault, R. J., Butler, B., &
 1697 de Boer, D. (2021, February). Tropospheric Composition and Circulation of
 1698 Uranus with ALMA and the VLA. *PSJ*, *2*(1), 3. doi: 10.3847/PSJ/abc48a
- 1699 Moses, J. I., Cavalie, T., Fletcher, L. N., & Roman, M. T. (2020, December). Atmo-
 1700 spheric chemistry on Uranus and Neptune. *Philosophical Transactions of the*
 1701 *Royal Society of London Series A*, *378*(2187), 20190477. doi: 10.1098/rsta.2019
 1702 .0477
- 1703 Orton, G. S., Moses, J. I., Fletcher, L. N., Mainzer, A. K., Hines, D., Hammel,
 1704 H. B., ... Line, M. R. (2014, November). Mid-infrared spectroscopy of Uranus
 1705 from the Spitzer infrared spectrometer: 2. Determination of the mean compo-
 1706 sition of the upper troposphere and stratosphere. *Icarus*, *243*, 471-493. doi:
 1707 10.1016/j.icarus.2014.07.012
- 1708 Parisi, M., Kaspi, Y., Galanti, E., & et al. (2021, October). The depth of Jupiters
 1709 Great Red Spot constrained by Juno gravity overflights. *Science*, *374*, 964.
 1710 doi: 10.1126/science.abf1396
- 1711 Plass, G. N., Kattawar, G. W., & Catchings, F. E. (1973, January). Matrix operator
 1712 theory of radiative transfer. 1: Rayleigh scattering. *ApOpt*, *12*, 314-329. doi:
 1713 10.1364/AO.12.000314
- 1714 Rayner, J. T., Cushing, M. C., & Vacca, W. D. (2009, December). The Infrared
 1715 Telescope Facility (IRTF) Spectral Library: Cool Stars. *ApJS*, *185*(2), 289-
 1716 432. doi: 10.1088/0067-0049/185/2/289
- 1717 Rey, M., Nikitin, A. V., Bézard, B., Rannou, P., Coustenis, A., & Tyuterev, V. G.
 1718 (2018, March). New accurate theoretical line lists of $^{12}\text{CH}_4$ and $^{13}\text{CH}_4$ in the
 1719 0-13400 cm $^{-1}$ range: Application to the modeling of methane absorption in
 1720 Titan's atmosphere. *Icarus*, *303*, 114-130. doi: 10.1016/j.icarus.2017.12.045
- 1721 Roman, M. T., Banfield, D., & Gierasch, P. J. (2018, August). Aerosols and
 1722 methane in the ice giant atmospheres inferred from spatially resolved,
 1723 near-infrared spectra: I. Uranus, 2001-2007. *Icarus*, *310*, 54-76. doi:
 1724 10.1016/j.icarus.2017.10.036
- 1725 Seiff, A., Kirk, D. B., Knight, T. C. D., Young, R. E., Mihalov, J. D., Young, L. A.,
 1726 ... Atkinson, D. (1998, September). Thermal structure of Jupiter's atmo-
 1727 sphere near the edge of a 5- μm hot spot in the north equatorial belt. *J. Geo-*
 1728 *phys. Res.*, *103*(E10), 22857-22890. doi: 10.1029/98JE01766
- 1729 Simon, A. A., Wong, M. H., & Hsu, A. I. (2019, March). Formation of a New Great
 1730 Dark Spot on Neptune in 2018. *Geophys. Res. Lett.*, *46*(6), 3108-3113. doi: 10
 1731 .1029/2019GL081961
- 1732 Simon, A. A., Wong, M. H., & Orton, G. S. (2015, October). First Results from the
 1733 Hubble OPAL Program: Jupiter in 2015. *ApJ*, *812*(1), 55. doi: 10.1088/0004
 1734 -637X/812/1/55
- 1735 Smith, B. A., Briggs, G. A., Danielson, G. E., Cook, A. F., Davies, M. E., Hunt,
 1736 G. E., ... Suomi, V. E. (1977, November). Voyager Imaging Experiment.
 1737 *SSRv*, *21*(2), 103-127. doi: 10.1007/BF00200847
- 1738 Smith, B. A., Soderblom, L. A., Banfield, D., Barnet, C., Basilevksy, A. T.,

- 1740 Beebe, R. F., ... Veverka, J. (1989, December). Voyager 2 at Neptune: Imaging Science Results. *Science*, *246*(4936), 1422-1449. doi: 10.1126/science.246.4936.1422
- 1741 Sromovsky, L. A. (2005a, January). Accurate and approximate calculations of Raman scattering in the atmosphere of Neptune. *Icarus*, *173*(1), 254-283. doi: 10.1016/j.icarus.2004.08.008
- 1742 Sromovsky, L. A. (2005b, January). Effects of Rayleigh-scattering polarization on reflected intensity: a fast and accurate approximation method for atmospheres with aerosols. *Icarus*, *173*(1), 284-294. doi: 10.1016/j.icarus.2004.07.016
- 1743 Sromovsky, L. A., & Fry, P. M. (2008, January). The methane abundance and structure of Uranus' cloud bands inferred from spatially resolved 2006 Keck grism spectra. *Icarus*, *193*(1), 252-266. doi: 10.1016/j.icarus.2007.08.037
- 1744 Sromovsky, L. A., Fry, P. M., Dowling, T. E., Baines, K. H., & Limaye, S. S. (2001, February). Coordinated 1996 HST and IRTF Imaging of Neptune and Triton. III. Neptune's Atmospheric Circulation and Cloud Structure. *Icarus*, *149*(2), 459-488. doi: 10.1006/icar.2000.6564
- 1745 Sromovsky, L. A., Fry, P. M., & Kim, J. H. (2011, September). Methane on Uranus: The case for a compact CH₄ cloud layer at low latitudes and a severe CH₄ depletion at high-latitudes based on re-analysis of Voyager occultation measurements and STIS spectroscopy. *Icarus*, *215*(1), 292-312. doi: 10.1016/j.icarus.2011.06.024
- 1746 Sromovsky, L. A., Karkoschka, E., Fry, P. M., de Pater, I., & Hammel, H. B. (2019, January). The methane distribution and polar brightening on Uranus based on HST/STIS, Keck/NIRC2, and IRTF/SpeX observations through 2015. *Icarus*, *317*, 266-306. doi: 10.1016/j.icarus.2018.06.026
- 1747 Sromovsky, L. A., Karkoschka, E., Fry, P. M., Hammel, H. B., de Pater, I., & Rages, K. (2014, August). Methane depletion in both polar regions of Uranus inferred from HST/STIS and Keck/NIRC2 observations. *Icarus*, *238*, 137-155. doi: 10.1016/j.icarus.2014.05.016
- 1748 Sromovsky, L. A., Limaye, S. S., & Fry, P. M. (1993, September). Dynamics of Neptune's Major Cloud Features. *Icarus*, *105*(1), 110-141. doi: 10.1006/icar.1993.1114
- 1749 Stockman, A. (2019, December). Cone fundamentals and CIE standards. *Current Opinion in Behavioral Sciences*, *30*, 87-93. doi: 10.1016/j.cobeha.2019.06.005
- 1750 Stockman, A., & Sharpe, L. T. (2000, June). The spectral sensitivities of the middle- and long-wavelength-sensitive cones derived from measurements in observers of known genotype. *Vision Research*, *40*, 1711-1737. doi: 10.1016/S0042-6989(00)00021-3
- 1751 Stratman, P. W., Showman, A. P., Dowling, T. E., & Sromovsky, L. A. (2001, June). EPIC Simulations of Bright Companions to Neptune's Great Dark Spots. *Icarus*, *151*(2), 275-285. doi: 10.1006/icar.2001.6603
- 1752 Teanby, N. A., Irwin, P. G. J., Moses, J. I., & Helled, R. (2020, December). Neptune and Uranus: ice or rock giants? *Philosophical Transactions of the Royal Society of London Series A*, *378*(2187), 20190489. doi: 10.1098/rsta.2019.0489
- 1753 Tice, D. S., Irwin, P. G. J., Fletcher, L. N., Teanby, N. A., Hurley, J., Orton, G. S., & Davis, G. R. (2013, April). Uranus' cloud particle properties and latitudinal methane variation from IRTF SpeX observations. *Icarus*, *223*(2), 684-698. doi: 10.1016/j.icarus.2013.01.006
- 1754 Toledo, D., Irwin, P. G. J., Rannou, P., Fletcher, L. N., Teanby, N. A., Wong, M. H., & Orton, G. S. (2020, November). Constraints on Neptune's haze structure and formation from VLT observations in the H-band. *Icarus*, *350*, 113808. doi: 10.1016/j.icarus.2020.113808
- 1755 Toledo, D., Irwin, P. G. J., Rannou, P., Teanby, N. A., Simon, A. A., Wong, M. H., & Orton, G. S. (2019, November). Constraints on Uranus's haze structure, formation and transport. *Icarus*, *333*, 1-11. doi: 10.1016/j.icarus.2019.05.018

- 1795 Tollefson, J., de Pater, I., Molter, E. M., Sault, R. J., Butler, B. J., Luszcz-Cook, S.,
1796 & DeBoer, D. (2021, June). Neptune's Spatial Brightness Temperature Variations from the VLA and ALMA. *PSJ*, 2(3), 105. doi: 10.3847/PSJ/abf837
1797
1798 West, R. A., Baines, K. H., Friedson, A. J., Banfield, D., Ragent, B., & Taylor,
1799 F. W. (2004). Jovian clouds and haze. In F. Bagenal, T. E. Dowling, &
1800 W. B. McKinnon (Eds.), *Jupiter. the planet, satellites and magnetosphere*
1801 (Vol. 1, p. 79-104).
1802 West, R. A., Strobel, D. F., & Tomasko, M. G. (1986, March). Clouds, aerosols, and
1803 photochemistry in the Jovian atmosphere. *Icarus*, 65(2-3), 161-217. doi: 10
1804 .1016/0019-1035(86)90135-1
1805 Wong, M. H., de Pater, I., Asay-Davis, X., Marcus, P. S., & Go, C. Y. (2011,
1806 September). Vertical structure of Jupiter's Oval BA before and after
1807 it reddened: What changed? *Icarus*, 215(1), 211-225. doi: 10.1016/
1808 j.icarus.2011.06.032
1809 Wong, M. H., Tollefson, J., Hsu, A. I., de Pater, I., Simon, A. A., Hueso, R., ...
1810 Baranec, C. (2018, March). A New Dark Vortex on Neptune. *AJ*, 155(3), 117.
1811 doi: 10.3847/1538-3881/aaa6d6